THE ROLE OF PRECIOUS METAL NANOPARTICLES ON THE OXYGEN EXCHANGE KINETICS FROM CERIA

A THESIS SUBMITTED TO
THE GRADUATE SCHOOL OF NATURAL AND APPLIED SCIENCES
OF
MIDDLE EAST TECHNICAL UNIVERSITY

BY

DENİZ KAYA

IN PARTIAL FULFILLMENT OF THE REQUIREMENTS
FOR
THE DEGREE OF MASTER OF SCIENCE
IN
CHEMICAL ENGINEERING

SEPTEMBER 2016

Approval of thesis:

THE ROLE OF PRECIOUS METAL NANOPARTICLES ON THE OXYGEN EXCHANGE KINETICS FROM CERIA

submitted by **DENİZ KAYA** in partial fulfillment of the requirements for the degree of **Master of Science in Chemical Engineering Department, Middle East Technical University** by,

Prof. Dr. Gülbin Dural Ünver
Dean, Graduate School of **Natural and Applied Sciences** _______________

Prof. Dr. Halil Kalıpçılar
Head of Department, **Chemical Engineering** _______________

Prof. Dr. Deniz Üner
Supervisor, **Chemical Engineering Dept., METU** _______________

Assoc. Dr. Serkan Kıncal
Co-Supervisor, **Chemical Engineering Dept., METU** _______________

Examining Committee Members:

Prof. Dr. Derek K. Baker
Mechanical Engineering Dept., METU _______________

Prof. Dr. Deniz Üner
Chemical Engineering Dept., METU _______________

Assoc. Prof. Dr. Serkan Kıncal
Chemical Engineering Dept., METU _______________

Assoc. Prof. Dr. Niyazi Alper Tapan
Chemical Engineering Dept., Gazi University _______________

Asst. Prof. Dr. Harun Koku
Chemical Engineering Dept., METU _______________

Date: 07.09.2016

I hereby declare that all information in this document has been obtained and presented in accordance with academic rules and ethical conduct. I also declare that, as required by these rules and conduct, I have fully cited and referenced all material and results that are not original to this work.

Name, Last Name: Deniz Kaya

Signature:

ABSTRACT

THE ROLE OF PRECIOUS METAL NANOPARTICLES ON THE OXYGEN EXCHANGE KINETICS FROM CERIA

Kaya, Deniz
M.Sc., Department of Chemical Engineering
Supervisor: Prof. Dr. Deniz Üner
Co-Supervisor: Assoc. Prof. Serkan Kıncal

September 2016, 102 pages

The oxygen exchange kinetics of precious metal added ceria and ceria-alumina oxides were investigated by temperature programmed analyses and microcalorimetric measurements. 1 wt. % Pd/CeO_2 and 1 wt. % Pd/Al_2O_3 oxides were synthesized by the incipient wetness method. 1 wt. % Pd/CeO_2-Al_2O_3 oxides with 20 wt. %, 15 wt. % and 10 wt. % loadings of ceria were synthesized by the sequential impregnation method. Temperature programmed reduction (TPR) analysis was performed to analyze the reducibility of prepared oxides. At temperatures below 200 °C, surface ceria atoms were totally reduced for all prepared oxides and the total reduction of CeO_2 to Ce_2O_3 was observed for alumina-added oxides. Hence, there are Pd-CeO_2 interactions in all prepared oxides and Pd increases the reducibility of ceria at lower temperatures via the spillover of hydrogen in the presence of Pd atoms. Temperature programmed thermal decomposition (TPtD) and temperature programmed oxidation (TPO) cycles were performed to understand the oxygen release/uptake temperature, capacity and kinetics of prepared oxides. It is clearly seen that addition of Pd to CeO_2 decreases the decomposition temperature of ceria by nearly 940 °C via the reverse spillover of oxygen atoms in ceria in the presence of Pd. Additionally, increase in alumina amount for prepared oxides results in an increase in oxygen release amount per ceria basis. Activation energies were calculated for TPR by the

Kissinger method. It can be concluded that reduction process is in the pore diffusion regime and mass transfer limited for while the reduction process is in the kinetic regime for 1 % Pd/CeO_2. Activation energies were calculated for TPtD by Redhead and differential methods. Volumetric chemisorption measurement was performed for 1 wt. % Pd/CeO_2 to analyze the hydrogen adsorption amount and to calculate the dispersion. Microcalorimetric measurements were performed for prepared oxides using H_2, O_2 and H_2O vapor in order to investigate the adsorption amounts of gases and heat of adsorption data. It is seen that H_2, O_2 and H_2O adsorption capacity increases with the addition of alumina and heat of O_2 adsorption is almost two times higher than heat of H_2O adsorption for all prepared oxides which proves that prepared oxides can be oxidized with water in addition of oxygen.

Keywords: Pd/CeO_2, Pd/CeO_2-Al_2O_3, temperature programmed analysis, oxygen exchange kinetics, metal support interactions, microcalorimetry.

ÖZ

DEĞERLİ METAL NANOPARÇACIKLARININ SERYUM DİOKSİT OKSİJEN DEĞİŞİM KİNETİĞİ ÜZERİNE ETKİSİ

Kaya, Deniz
Yüksek Lisans, Kimya Mühendisliği Bölümü
Tez Yöneticisi: Prof. Dr. Deniz Üner
Ortak Tez Yöneticisi: Assoc. Prof. Serkan Kıncal

Eylül 2016, 102 sayfa

Değerli metal eklenmiş seryum dioksit ve seryum dioksit-aluminyum oksit oksitlerinin oksijen alışveriş kinetiği, sıcaklık programlı analizler ve mikrokalorimetrik ölçümlerle incelendi. Kütlece % 1 Pd/CeO_2 ve kütlece % 1 Pd/Al_2O_3 oksitleri ıslaklık başlangıcı emdirme metodu ile sentezlendi. Kütlece % 20, % 15 ve % 10 seryum dioksit yüklenmiş kütlece % 1 Pd/CeO_2-Al_2O_3 oksitleri sıralı emdirme metodu ile sentezlendi. Hazırlanan oksitlerin indirgenebilirliğini ölçmek amacıyla sıcaklık programlı indirgenme (TPR) analizi yapıldı. 200 °C sıcaklığın altında, hazırlanan bütün oksitler için yüzey seryum dioksit atomlarının tamamının ve aluminyum oksit içeren oksitler için seryum (II) oksitin tamamen seryum (III) oksite indirgendiği gözlemlendi. Bunun sonucu olarak, hazırlanan oksitlerin tamamında Pd-CeO_2 etkileşimi görüldü ve Pd atomlarının varlığında hidrojen taşması mekanizması ile seryum dioksitin düşük sıcaklıklarda indirgenebilirliği Pd sayesinde artış gösterdi. Hazırlanan oksitlerin oksijen alma/salma sıcaklığı, kapasitesi ve kinetiğini ölçmek amacıyla sıcaklık programlı ısıl dekompozisyon (TPtD) ve sıcaklık programlı oksidasyon (TPO) döngüleri yapıldı. Bu döngüler sonucunda CeO_2 dekompozisyon sıcaklığının Pd eklenmesi sonucunda seryum dioksitte bulunan oksijen atomlarının Pd varlığında ters taşma mekanizması ile yaklaşık 940 °C düşürüldüğü açıkça gözlendi. Buna ek olarak, aluminyum dioksit miktarı arttıkça seryum dioksit bazında oksijen salma miktarının arttığı görüldü. TPR için Kissinger metod kullanılarak aktivasyon enerjileri hesaplandı. Bunun sonucunda seryum dioksit için indirgenme prosesinin kütle aktarımınca sınırlandırılmış ve gözenek dağıtımı bölgesinde olduğu fakat % 1 Pd/CeO_2 için indirgenme prosesinin kinetik bölgede olduğu sonuçlandırıldı. TPtD için Redhead ve diferansiyel metodlar kullanılarak aktivasyon enerjileri hesaplandı. Kütlece % 1 Pd/CeO_2 oksiti için, hidrojen adsorplanma miktarı ve metal dağılım oranını hesaplamak amacıyla sabit hacimli kimyasal adsorpsiyon ölçümleri yapıldı. Hazırlanan oksitler için H_2, O_2 ve H_2O buharı adsorplanma miktarı ve adsorplanma ısını ölçmek amacıyla mikrokalorimetrik ölçümler yapıldı. Bu ölçümler neticesinde, H_2, O_2 ve H_2O adsorplanma kapasitesinin aluminyum oksit ilavesi ile arttığı ve hazırlanan bütün oksitler için, O_2 adsorplanma ısısının H_2O adsorplanma ısısından yaklaşık iki kat yüksek olduğu görüldü ve bunun sonucunda hazırlanan bütün oksitlerin, oksijenin yanında su ile de oksitlenebildiği sonucuna varıldı.

Anahtar Kelimeler: Pd/CeO_2, Pd/CeO_2-Al_2O_3, sıcaklık programlı analiz, oksijen alışveriş kinetiği, metal destek etkileşimleri, mikrokalorimetre.

To my mother and the memory of my father

ACKNOWLEDGEMENTS

Throughout my studies, many people provided inspiration, encouragement and support to me. First of all, I would like to express my utmost gratitude to my supervisor Prof. Dr. Deniz Üner for her endless motivation, guidance and patience. I am grateful to her for letting me to be a part of her research group. Without her sanguine approach, I would never had gained all precious knowledge and experiences, not only in academic world but also in every aspects of life.

I also would like to present my gratitude to my co-supervisor Assoc. Prof. Dr. Serkan Kıncal for his supports and guidance.

I would like to present my sincere thanks to all members of UNER Research Group; Atalay Çalışan, Veysi Halvacı, Mustafa Yasin Aslan, Dr. Başar Çağlar, Ezgi Yavuzyılmaz, Dr. Mehmet Mert Oymak, Selda Odabaşı and former members; Dr. Taymaz Tabari, Dr. Dheerendra Singh and Cihan Ateş. I would like to express my special thanks to Atalay Çalışan for his endless motivation, guidance and support. His contributions played a big role on this research during all phases. I also would like to thank my lab buddy Veysi Halvacı for his kind friendship and supports both morally and technically. I also would like to present my thanks to former postdoctoral members of research group; Dr. Taymaz Tabari for all the knowledge he shared with me and Dr. Dheerendra Singh for his guidance in microcalorimetry and chemisorption experiments.

I would like share my thanks to the technical staff of Chemical Engineering Department; Gülten Orakçı, Mihrican Açıkgöz, İsa Çağlar, Süleyman Nazif Kuşhan and Ertuğrul Özdemir for their support and assistance.

The Scientific and Research Council of Turkey (TÜBİTAK, Research Grant No: 213M006) is kindly acknowledged for the financial support during the study.

Turkish Petroleum Refineries Corporation (TÜPRAŞ) is also acknowledged for the financial support in the scope of RAYEP project.

I would like to present my lovely thanks to the people who are beyond being my friends and collegues; Berna Sezgin and Dilara Gülçin Çağlayan for their intimate friendship and all the precious times we spent together and Merve Tufan, Elif Kocaman, Zeynep Sümer, Ebru Okur, Onur Yüksel and Ahmet Gökhan Karabıyık for their priceless friendship and moral supports that they provide me throughout my whole university life.

I would like to present my sincerest thanks to my family; my mom, dad, sisters, brother, nephews and my little niece for their unconditional love and support under any circumstances. Throughout my whole life, they showed unlimited patience and had always faith in me.

Last but not the least, I would like to express my deepest thanks to Kerem Eyice for his great support and unconditional love. Without his existence, many of beautiful things in my life would not have happened.

TABLE OF CONTENTS

ABSTRACT v

ÖZ vii

ACKNOWLEDGEMENTS x

TABLE OF CONTENTS xii

LIST OF TABLES xvi

LIST OF FIGURES xviii

LIST OF SYMBOLS xxi

CHAPTERS

- 1. INTRODUCTION 1
  - 1.1. Hydrogen Production 1
  - 1.2. Solar Thermochemical Water Splitting 4
  - 1.3. Temperature Programmed Reduction (TPR) 6
  - 1.4. Temperature Programmed Oxidation (TPO) 6
  - 1.5. Temperature Programmed Thermal Decomposition (TPtD) 7
  - 1.6. Objectives 7
- 2. LITERATURE SURVEY 9
  - 2.1. Ceria (CeO_2) 9
    - 2.1.1. Ceria Applications 10
    - 2.1.2. Ceria Oxygen Storage Capacity and Oxygen Exchange Kinetics 12
      - 2.1.2.1. The Effects of Precious Metals on Ceria Oxygen Exchange Kinetics 16
      - 2.1.2.2. Metal Support Interactions 18

2.1.2.3. Activation Energies of Different Reactions: Pd/CeO_2 Used as Catalyst 19

2.2. Two Step Solar Thermochemical Hydrogen Production on Reducible Metal Oxides 21

2.2.1. Volatile Cycles 24

2.2.2. Nonvolatile Cycles 25

2.2.3. Ceria for Use in Solar Thermochemical Cycles 27

3. MATERIALS AND METHODS 29

3.1. Materials 29

3.1.1. Synthesis of 1 % Pd/CeO_2 with Incipient Wetness Method 29

3.1.2. Synthesis of 1 % Pd/Al_2O_3 with Incipient Wetness Method 29

3.1.3. Synthesis of 1 % Pd/CeO_2-Al_2O_3 with Sequential Impregnation Method 30

3.2. Characterization 30

3.2.1. BET Analysis 30

3.2.2. XRD Analysis 30

3.2.3. TPx Analyses 31

3.2.4. Chemisorption 32

3.2.5. Microcalorimetry 33

3.3. Kinetic Analysis 35

3.3.1. Redhead Method 35

3.3.2. Differential Method 35

3.3.3. Kissinger Method 36

4. RESULTS AND DISCUSSIONS 39

4.1. BET Results 39

4.2. XRD Results 40

4.3. TPx Results 42
    4.3.1. TPR Results 42
        4.3.1.1. Hydrogen Uptake Amounts 47
    4.3.2. TPO Results 51
    4.3.3. TPtD Results 53
        4.3.3.1. Oxygen Uptake and Release Amounts 57
    4.3.4. Activation Energy Calculations for TPx Experiments 58
        4.3.4.1. Redhead Method 58
        4.3.4.2. Differential Method 59
        4.3.4.3. Kissinger Method 61
4.4. Chemisorption Results 62
4.5. Microcalorimetry Results 62
    4.5.1. H_2 Adsorption 63
    4.5.2. O_2 Adsorption 65
    4.5.3. H_2O Adsorption 66
    4.5.4. Heat of Adsorption and Adsorption Amount Comparison 68
5. CONCLUSIONS 71
REFERENCES 73

APPENDICES

A. MICROMERITICS CHEMISORB 2720 83
B. EXPERIMENTAL PROCEDURES 85
    B.1. TPx Experimental Procedures 85
        B.1.1. TPR Experiments 86
        B.1.2. TPO Experiments 87
        B.1.3. TPtD Experiments 88
    B.2. Chemisorption Experimental Procedures 89

B.3. Microcalorimetry Experimental Procedures 90

C. CALCULATIONS 91

C.1. Hydrogen Consumption Calculations 91

C.1.1. Calibration with Reference Material: Ag_2O 91

C.1.2. CeO_2 93

C.1.3. 1 % Pd/CeO_2 94

C.1.4. 1 % Pd/CeO_2-Al_2O_3 96

C.2. Oxygen Calibration with Air Injection 98

C.3. Surface Atom Percentage Calculation 100

C.4. Activation Energy Calculations 101

C.4.1. Redhead Method 101

C.5. Dispersion Calculations 102

LIST OF TABLES

TABLES

Table 1.1 Hydrogen production methods [2] 2
Table 2.1 Activation energies of CeO_2 and Pd/CeO_2 for different reactions reported in the literature 20
Table 2.2 Solar thermochemical hydrogen production cycles 22
Table 4.1 BET surface areas for used and synthesized materials 39
Table 4.2 Hydrogen consumption for CeO_2 during TPR 48
Table 4.3 Hydrogen consumption for 1 % Pd/CeO_2 during TPR 48
Table 4.4 Hydrogen consumption for 1 % Pd/CeO_2-Al_2O_3 oxides during TPR in the temperature range of 25-200 °C 50
Table 4.5 Oxygen uptake and release amounts for 1 % Pd/CeO_2 during two-step thermochemical cycles at 10 °C/min heating rate 57
Table 4.6 Oxygen uptake and release amounts for 1 % Pd/CeO_2-Al_2O_3 oxides during two-step thermochemical cycles at 20 °C/min heating rate 58
Table 4.7 Calculated activation energies for TPtD experiments by Redhead method 59
Table 4.8 Calculated activation energies and pre-exponential factors for prepared oxides during TPtD experiments by using differential method 60
Table 4.9 Calculated activation energies and pre-exponential factors for CeO_2 and 1 % Pd/CeO_2 during TPR experiments by using Kissinger method 61
Table 4.10 Percentage Pd dispersions for synthesized oxides 65
Table 4.11 Heat of adsorption data at initial coverage for 1 % Pd/CeO_2 and 1 % Pd/CeO_2-Al_2O_3 oxides 68
Table C.1 Ag_2O amounts in TPR analysis 92
Table C.2 Calculated hydrogen consumption for CeO_2 using stoichiometry 93
Table C.3 Calculated hydrogen consumption for 1 % Pd/CeO_2 using stoichiometry 94

Table C.4 Calculated hydrogen consumption for 1 % Pd/CeO_2-Al_2O oxides using stoichiometry 96

Table C.5 Air injection and corresponding oxygen amounts 98

Table C.6 Percentage CeO_2 surface atoms for synthesized oxides 100

LIST OF FIGURES

FIGURES

Figure 1.1 World energy consumption by source between 1990-2040 (adapted from [1]) 1

Figure 1.2 A thermochemical cycle that converts H_2O to H_2 and O_2 by decomposition and oxidation of a metal oxide using solar energy [8] 4

Figure 2.1 FCC cell of fluorite structure of CeO_2 (adapted from [14] with permission) 9

Figure 2.2 TPR pattern of CeO_2 samples with surface area (a) 1.5 m^2/g, (b) 30 m^2/g (c) 130 m^2/g (adapted from [26] with permission) 13

Figure 2.3 TPR pattern of (a) CeO_2, (b) $Ce_{0.2}Zr_{0.8}O_2$ (c) $Ce_{0.5}Zr_{0.5}O_2$, (d) $Ce_{0.8}Zr_{0.2}O_2$ (adapted from [28] with permission) 15

Figure 2.4 TPR pattern of $Pt/BaO/Ce_{0.25}Zr_{0.75}O_2$ (adapted from [31] with permission) 16

Figure 2.5 TPR pattern of (A) Ir/CeO_2 (B) Pd/CeO_2 (C) Pt/CeO_2 (D) Ru/CeO_2 (E) Rh/CeO_2 (F) CeO_2 (adapted from [14] with permission) 17

Figure 2.6 Schematic of solar two-step hydrogen production cycle based on CeO_2/Ce_2O_3 system (adapted from [9] with permission) 27

Figure 3.1 Micromeritics ChemiSorb 2720 TPx equipment 31

Figure 3.2 Drawing of chemisorption manifold 32

Figure 3.3 Drawing of microcalorimetry manifold 34

Figure 4.1 XRD spectra for (a) fresh (b) oxidized (c) reduced catalyst (adapted from [32]) 40

Figure 4.2 XRD spectra for 1 % Pd/20 % CeO_2-Al_2O_3 (oxidized), 1 % Pd/15 % CeO_2-Al_2O_3 (reduced), 1 % Pd/10 % CeO_2-Al_2O_3 (oxidized) 41

Figure 4.3 TPR pattern of CeO_2 and 1 % Pd/CeO_2 at (a) 5 °C/min (b) 10 °C/min and (c) 20 °C/min heating rates under 25 sccm 10 % H_2-Ar flow 43

Figure 4.4 TPR pattern of 1 % Pd/CeO_2 at 5, 10 and 20 °C/min heating rates under 25 sccm 10 % H_2-Ar flow 44

Figure 4.5 TPR pattern of 1 % Pd/CeO_2 with CeO_2 surface areas 2.9 m^2/g and 48.1 m^2/g at 20 °C/min heating rate under 25 sccm 10 % H_2-Ar flow 45

Figure 4.6 TPR pattern of CeO_2, 1 % Pd/CeO_2, 1 % Pd/CeO_2-Al_2O_3 oxides, CeO_2-Al_2O_3, 1 % Pd/Al_2O_3 and γ-Al_2O_3 at 20 °C/min heating rate under 25 sccm 10 % H_2-Ar flow 46

Figure 4.7 TPO pattern after TPtD of 1 % Pd/CeO_2 at (a) 10 °C/min and (b) 20 °C/min heating rates under 25 sccm 2 % O_2-He flow 52

Figure 4.8 TPO pattern after TPtD of 1 % Pd/CeO_2 and 1 % Pd/CeO_2-Al_2O_3 oxides at 20 °C/min heating rate under 25 sccm 2 % O_2-He flow 53

Figure 4.9 TPtD pattern after TPO of 1 % Pd/CeO_2 at (a) 10 °C/min and (b) 20 °C/min heating rates under 25 sccm He flow 55

Figure 4.10 TPtD pattern after TPO of 1 % Pd/CeO_2 and 1 % Pd/CeO_2-Al_2O_3 oxides at 20 °C/min heating rate under 25 sccm He flow 56

Figure 4.11 TPtD 1 pattern after TPO 1 of 1 % Pd/CeO_2 and 1 % Pd/CeO_2-Al_2O_3 oxides at 20 °C/min heating rate under 25 sccm He flow 56

Figure 4.12 Percentage dispersion measurements for 1 % Pd/CeO_2 at 30 °C 62

Figure 4.13 Differential heats of H_2 adsorption on 1 % Pd/CeO_2 (at 100 °C) and 1 % Pd/CeO_2-Al_2O_3 oxides (at 50 °C) (a) μmol H_2/g oxide vs differential heat of adsorption (b) H atom/Pd atom vs differential heat of adsorption 63

Figure 4.14 H_2 adsorption isotherms for 1 % Pd/CeO_2 (at 100 °C) and 1 % Pd/CeO_2-Al_2O_3 oxides (at 50 °C) 64

Figure 4.15 Differential heats of O_2 adsorption on 1 % Pd/CeO_2 (at 100 °C) and 1 % Pd/CeO_2-Al_2O_3 oxides (at 50 °C) 65

Figure 4.16 O_2 adsorption isotherms for 1 % Pd/CeO_2 (at 100 °C) and 1 % Pd/CeO_2-Al_2O_3 oxides (at 50 °C) 66

Figure 4.17 Differential heats of H_2O adsorption on 1 % Pd/CeO_2 (at 100 °C) and 1 % Pd/CeO_2-Al_2O_3 oxides (at 50 °C) 67

Figure 4.18 H_2O adsorption isotherms for 1 % Pd/CeO_2 (at 100 °C) and 1 % Pd/CeO_2-Al_2O_3 oxides (at 50 °C) 67

Figure C.1 TPR pattern of Ag_2O at 10 °C/min heating rate under 25 sccm 10 % H_2-Ar flow 91

Figure C.2 Hydrogen consumption area calculations for CeO_2 during TPR using Matlab Interactive Peak Fitter tool 93

Figure C.3 Hydrogen consumption area calculations for 1 % Pd/CeO_2 during TPR using Matlab Interactive Peak Fitter tool 95

Figure C.4 Hydrogen consumption area calculations for 1 % Pd/CeO_2-Al_2O_3 oxides during TPR using Matlab Interactive Peak Fitter tool 97

Figure C.5 Air injection experiments for oxygen calibration 98

Figure C.6 Oxygen calibration plot for Micromeritics Chemisorb 2720 99

Figure C.7 Activation energy calculation by Redhead Method using MathCad.. 101

LIST OF SYMBOLS

BET	Brunauer-Emmett-Teller
C	Concentration of reactive species, mol/L
E_a	Activation energy, kJ/mol
H_{ads}	Heat of adsorption, kJ/mol
k_0	Pre-exponential factor, 1/min
k(T)	Rate constant, min^{-1}
OSC	Oxygen storage capacity
R	Gas constant, $8.314*10^{-3}$ kJ/mol.K
x	Fraction of remaining reactant
t	Time, min
T	Temperature, K
T_0	Initial temperature, K
TCD	Thermal conductivity detector
TPO	Temperature programmed oxidation
TPR	Temperature programmed reduction
TPtD	Temperature programmed thermal decomposition
α	Heating rate, K/min

CHAPTER 1

INTRODUCTION

1.1. Hydrogen Production

World's energy need and consumption has drastically increased especially after the 20th century and it is expected to continue in future due to global increase in population and technology. U.S. Energy Information and Administration reported that world energy consumption will grow by 56 % between 2010 and 2040, from 524 quadrillion Btu to 820 quadrillion Btu [1].

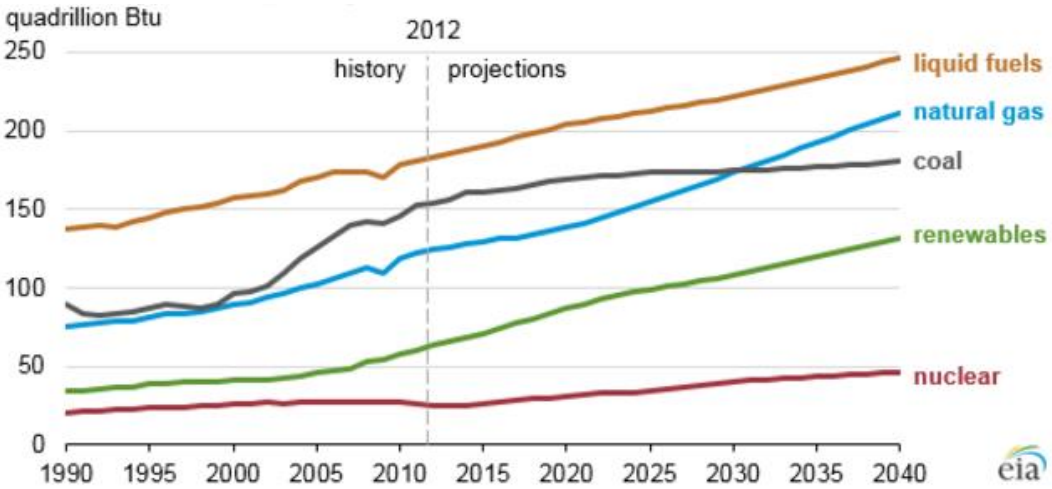

Figure 1.1 World energy consumption by source between 1990-2040 (adapted from [1])

Since energy need is increasing day by day, energy generation capacity should be developed. It is proved that reserves of fossil fuels are not discovered as fast as world's energy need and fossil fuels can only supply nearly 80 % of world energy use through 2040 [1]. Therefore, more secure, clean and varied energy sources should be used to meet the world energy needs, and also to reduce the greenhouse gas emissions.

Among the other alternatives, hydrogen has various advantages as a future fuel and energy carrier. Hydrogen (H_2) is the lightest and simplest chemical element which is naturally present on Earth in combination with other elements such as with oxygen in water and with carbon and nitrogen in hydrocarbons and fossil fuels.

Hydrogen can be produced by different industrial methods which are summarized in Table 1.1.

Table 1.1 Hydrogen production methods [2]

System	**Type**	**Raw materials**	**Efficiency (%)**
Steam Reforming	High temperature	Fossil fuels	70-85
Gasification	High temperature	Fossil fuels	60-75
Thermal Decomposition	High temperature	Fossil fuels	60-75
Electrolysis	High temperature	H_2O	20
Photovoltaic	Low temperature	H_2O	19.8
Solar Thermochemical	High temperature	H_2O, metal oxides	15
Photoelectrochemical	Low temperature	H_2O	12.4
Photosynthesis	Low temperature	H_2O, biomass	<10

It is clearly seen that fossil fuel based hydrogen production techniques, such as steam reforming, steam gasification and thermal decomposition, have the highest efficiencies.

Steam reforming is the cheapest and most common hydrogen production method. In this method, natural gas or other hydrocarbons are mixed with steam after purification, and carbon monoxide (CO) and hydrogen (H_2) are produced. After that, with water gas shift reaction, CO is converted to carbon dioxide (CO_2) and hydrogen is purified from the product stream [3].

In gasification, coal is converted to hydrogen in partial oxidation of coal with steam and oxygen in high temperature and high pressure reaction conditions. Main products are CO, CO_2, H_2 and sulfur containing compounds. The product gas should be cleaned in conventional ways to recover sulphur and carbon capture and storage (CCS) unit should be built up because of high CO_2 emissions.

The major concern about steam reforming and coal gasification is the high CO_2 emission due to the high carbon content of raw materials, i.e. fossil fuels. Based on the fuel used, a plant might need to deal with dust, organic sulfur and sulfides. Moreover, produced gas always needs to be purified in complex systems. Therefore, fossil fuel based hydrogen production should be replaced with renewable energy based methods.

Eco-friendly production of hydrogen is very important for clean environment and sustainable energy development. Although, the efficiencies are not high in renewable energy based hydrogen production methods, sustainability and the aspect of environmentally friendly production is much more important. Therefore, new technologies, such as solar or wind based electrolysis, biomass gasification, solar thermochemical water splitting etc., have gained an attention.

Biomass gasification is one of the promising clean hydrogen production methods in which agricultural residues, municipal and animal wastes, crops are used. Although carbon dioxide is released when biomass is oxidized, it is absorbed from the atmosphere and used in photosynthesis in biomass growing process. This carbon dioxide cycle makes the biomass gasification better then fossil fuel based hydrogen production methods by reducing the net carbon dioxide emissions. However, limited natural source and land problems are major concerns for this method [4].

It is estimated that the energy contained in one hour of sunlight is equal to the all energy consumption in the planet for one year, therefore the methods containing the use of sun’s energy to produce hydrogen are very good alternative methods [5]. Solar hydrogen production system can be classified into four categories; photovoltaic, photoelectrochemical, photobiological and solar thermochemical.

In photovoltaic hydrogen production, water is split into hydrogen and oxygen by using the electricity produced by photovoltaic panels. This electrolysis method is the most effective method due to the direct transformation of radiant solar energy to electrical energy [6]. However, it is one of the most costly hydrogen production methods.

Photoelectrochemical light collecting systems are also used to produce hydrogen by electrolysis of water. In this method, semiconductor materials are used and they are immersed in a water-based electrolyte in which water is split by using sunlight. Major disadvantages about this method are high land space and semiconductor requirements, low lifetimes and unknown operational details [7].

Hydrogen can also be produced by photobiological systems such as light dependent biophotolysis, biofermentation and light independent dark fermentation. Microalgae are generally used in this process due to their high hydrogen evolutions in bioreactors. This technology is still developing because it involves low efficiencies and only laboratory scale production is available.

1.2. Solar Thermochemical Water Splitting

Recently, two step solar thermochemical water splitting cycles have gained an attention due to the direct production of clean hydrogen. In Figure 1.2, solar thermochemical cycle for hydrogen production via water splitting is given.

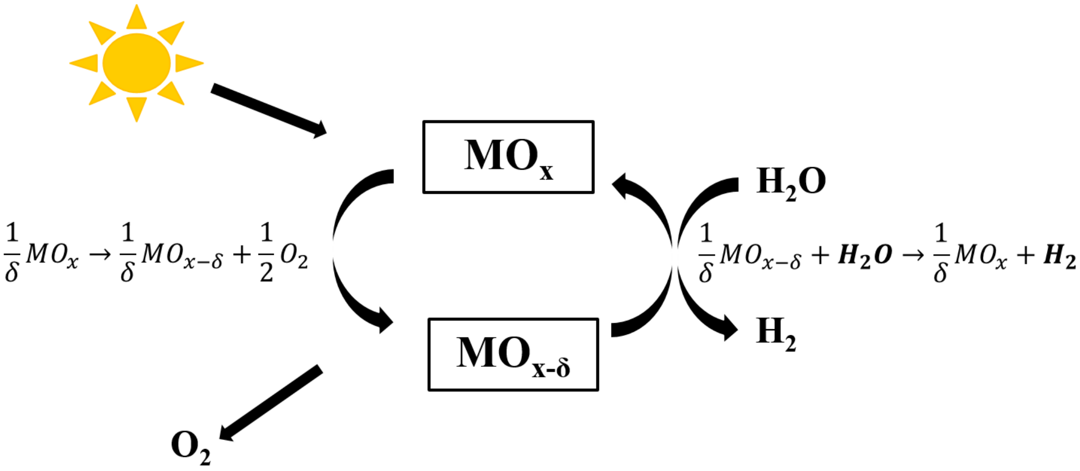
MO_x
$MO_{x-\delta}$
$\frac{1}{\delta}MO_x \rightarrow \frac{1}{\delta}MO_{x-\delta} + \frac{1}{2}O_2$
O_2
H_2O
$\frac{1}{\delta}MO_{x-\delta} + \boldsymbol{H_2O} \rightarrow \frac{1}{\delta}MO_x + \boldsymbol{H_2}$
H_2

Figure 1.2 A thermochemical cycle that converts H_2O to H_2 and O_2 by decomposition and oxidation of a metal oxide using solar energy [8]

In solar thermochemical cycles, water is used as a raw material and heat is used to decompose the metal oxide. Outputs are pure hydrogen and oxygen and there is no need for separation of products in this methods due to the fact that these gases are produced in different steps. Since pure hydrogen is generated, it can be directly used in fuel cells [9].

Solar thermochemical hydrogen production system consists of two main steps. Firstly, the metal oxide is decomposed by using sun's entire spectrum with a concentrator and releases oxygen under an inert atmosphere. The solar, highly endothermic and high temperature reaction for first step is given in Equation 1.1 below.

Decomposition of metal oxide (solar, endothermic, high temperature)

$$M_xO_y \rightarrow xM + \frac{y}{2}O_2 \qquad \text{Equation 1.1}$$

Secondly, by passing water through the decomposed formed of metal oxide, oxygen vacancies, formed in first step, are filled with the oxygen in water. Therefore, metal oxide is oxidized to its initial form and hydrogen is produced. The nonsolar, exothermic and low temperature reaction for second step is given in Equation 1.2 below.

Oxidation of metal oxide (nonsolar, exothermic, low temperature)

$$xM + yH_2O \rightarrow M_xO_y + yH_2 \qquad \text{Equation 1.2}$$

By performing decomposition and oxidation cycles again, hydrogen can be produced using solar energy, releasing only oxygen as a waste product.

Even though this hydrogen production method has relatively low efficiency, it has some major advantages;

1. CO_2, NO_x and sulphur containing waste products are not produced.
2. The energy of sun can be used infinitely.
3. There is no need for H_2/O_2 separation.
4. Clean H_2 is produced and it can be directly used in fuel cells.

Different metal oxide redox pairs are used in solar thermochemical hydrogen production cycles such as ZnO/Zn, CdO/Cd, Fe_3O_4/FeO, CeO_2/Ce_2O_3, perovskites etc.

1.3. Temperature Programmed Reduction (TPR)

Temperature programmed reduction (TPR) is a commonly used characterization technique for reducible solids, catalysts and metal oxides. With the help of TPR analysis, the number of reducible species present in the material and oxygen storage capacity (OSC) can be determined.

The reaction between the metal oxide, MO and hydrogen results in the formation of water and metal, M as can be represented by the equation given below [10].

$$MO_{(s)} + H_{2_{(g)}} \rightarrow M_{(s)} + H_2O_{(g)} \qquad \text{Equation 1.3}$$

In TPR analysis, a reducing gas (typically hydrogen in an inert gas such as nitrogen or argon) flows through a reducible material, usually at ambient pressure while the temperature is linearly increased with time. Changes in the concentration or mass of the gas mixture at the outlet of the reactor are monitored by usually using thermal conductivity detector (TCD) or mass spectrometer so that the reduction rate is continuously followed. The total amount of hydrogen uptake can be calculated. Therefore, the average oxidation state of the material after reduction can be determined [11].

1.4. Temperature Programmed Oxidation (TPO)

Temperature programmed oxidation (TPO) is used in OSC measurements to determine the oxygen uptake capacity of reduced or decomposed metal oxides.

The reaction between reduced metal, M and oxygen results in the formation of metal oxide, MO can be represented by the equation given below.

$$M_{(s)} + \frac{1}{2}O_{2_{(g)}} \rightarrow MO_{(s)} \qquad \text{Equation 1.4}$$

In TPO analysis, an oxidizing gas (typically oxygen mixtures with helium, water, carbon dioxide) flows through reduced material, usually at ambient pressure while the temperature is linearly increased with time. Similar with TPR analysis, oxidation rate is continuously recorded using thermal conductivity detector or mass spectrometer.

1.5. Temperature Programmed Thermal Decomposition (TPtD)

Temperature programmed thermal decomposition (TPtD) analysis is used to investigate the oxygen release capacity of metal oxides under an inert atmosphere, without using any reducing gas. Gorte reported that temperature programmed desorption is a powerful technique to understand the side densities and reaction pathways on metal oxides [12].

TPtD reaction occurs at relatively high temperatures compared to TPR and TPO reactions. Thermal oxygen release reaction of metal oxide, MO can be represented by the equation given below.

$$MO_{(s)} \rightarrow M_{(s)} + \frac{1}{2} O_{2(g)} \qquad \text{Equation 1.5}$$

In TPtD analysis, material is heated in a furnace under an inert gas flow (typically helium). Oxygen release temperature and capacity are measured using thermocouple, thermal conductivity detector or mass spectrometer.

1.6. Objectives

In this study, oxygen desorption and adsorption kinetics of precious metal (PM) added ceria and ceria-alumina oxides were investigated in details. The main objective of this study was to decrease the decomposition temperature of ceria and to investigate strong metal support interactions (SMSI) on PM-ceria interphase.

In the scope of these purposes, Pd/CeO_2, Pd/Al_2O_3 and Pd/CeO_2-Al_2O_3 oxides were synthesized by incipient wetness method and oxygen exchange kinetics were investigated using temperature programmed analyses. Moreover, microcalorimetric measurements were performed to analyze adsorption characteristics.

CHAPTER 2

LITERATURE SURVEY

2.1. Ceria (CeO_2)

Cerium (IV) oxide, also known as ceria, cerium dioxide and ceric oxide, is an oxide form of the most abundant rare earth element, cerium. Ceria is a pale yellow powder having a chemical formula of CeO_2 and molar mass of 172.115 g/mol. It is formed by the calcination of cerium oxalate or cerium hydroxide.

Ceria has the fluorite crystal structure shown in Figure 2.1 below. Fluorite structure, with anions (coordination number of 4) at every corner and a cation (coordination number of 8) in the middle, offers easily formed oxygen vacancies (high oxygen mobility) to ceria. Because the oxygen atoms in ceria are all in a plane with another, these atoms diffuse rapidly as a function of the number of oxygen vacancies and to vary the oxidation state from Ce^{+3} to Ce^{+4}. Therefore, with the increasing number of vacancies, oxygen can move more easily in the crystal. Eventually, the catalytic activity of ceria increases [13].

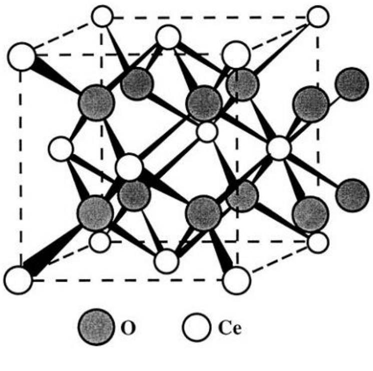

Figure 2.1 FCC cell of fluorite structure of CeO_2 (adapted from [14] with permission)

2.1.1. Ceria Applications

Ceria and ceria-containing materials have been studied in plenty of research for both academic and industrial purposes. Early publications related to ceria started in 1950s and ceria-related topics have gained a constant interest over the following years. It is seen that up to 2015, there are more than 26000 publications available in the literature and this number increased especially between 2014 and 2015 with the contribution of 2300 publications. A book named 'Catalysis by Ceria and Related Materials' was published in 2002 by Trovarelli for assembling different aspects of ceria and ceria-related materials [15]. There are review articles related to the structural properties and applications of ceria and ceria-containing materials [14][16]. Moreover, Applied Catalysis B: Environmental has more recently published a special issue for ceria including 33 papers related to the fundamental applications and theoretical studies [17].

Ceria and ceria-containing materials are commonly used as a catalyst or as a non-inert support for catalysts in various applications such as a promoter in three way catalytic converters for exhaust emission control systems, for soot combustion in diesel engines, as an electrolyte, as a barrier layer for cathodes or as a catalyst in cathode and anode in solid oxide fuel cells, as a catalyst for steam/dry reforming of hydrocarbons, water gas shift reaction, preferential oxidation of CO, oxidation of volatile organic compounds, thermochemical water splitting etc. In these applications, it is known that ceria plays different roles such as affecting the dispersion of supported metals, increasing the thermal stability of support, promoting precious metal reduction/oxidation, forming surface and bulk vacancies and releasing/uptaking oxygen.

The most common use of ceria is in three way catalytic converters (TWCs) as a promoter. In TWCs, the oxidation of CO and unburnt hydrocarbons should be performed as well as the reduction of NO_x compounds. They consist of monolithic ceramic substrate (usually cordierite), thermally stable support (usually doped alumina, Al_2O_3), precious metals serving as active phase (usually Pt, Pd or Rh) and CeO_2-based promoter (usually $Ce_xZr_{1-x}O_2$). The ability of creating oxygen vacancies of ceria plays a key role in TWCs. Ceria enhances the performance of

TWCs by interacting with precious metals and creating catalytically active sites at M-CeO (M: metal) interface for CO and unburnt hydrocarbon oxidation and NO_x reduction. In O_2-lean exhaust environment, ceria releases its oxygen by reducing itself with CO and unburnt hydrocarbons. In O_2-rich exhaust environment, oxygen is adsorbed by reduced ceria and oxidation of CO and unburnt hydrocarbons is completed by reducing NO_x. Therefore, ceria plays a direct role in TWCs in both O_2-lean and O_2-rich conditions by cycling its oxidation state between Ce^{+3} and Ce^{+4} through its oxygen storage capacity [18].

In diesel engines, soot particles consisting of carbon, adsorbed hydrocarbons, SO_x and water, are also emitted as well as CO, unburnt hydrocarbon and NO_x. Ceria based catalysts are the most effective catalysts for soot oxidation in diesel engines due to the high redox properties and oxygen exchange capacity of ceria. Ceria doped with Zr, Fe, Pr, Sm, Tb, Cu, Mn, Mo and ceria supported K, Co, Ag catalysts are reported in the literature for soot combustion [19].

Steam methane reforming (SMR), given in Equation 2.1 below, is the most commonly used industrial hydrogen production method. It is an endothermic process which should be conducted at high temperatures.

$$CH_4 + H_2O \leftrightarrow CO + 3H_2 \qquad \text{Equation 2.1}$$

In steam methane reforming, CeO_2-ZrO_2 oxides are used and it is reported that the catalysts are active up to 773 K. Gorte et al. reported that ceria-supported Pd and Ni catalysts are more active for steam methane reforming because of dual function mechanism in which while oxygen of ceria is transferred to supported metal via spillover, reduced ceria is oxidized by water [20].

Water gas shift reaction (WGSR), given in Equation 2.2, is a well-established industrial method to purify H_2 from CO. It is an exothermic process in which temperature should be kept as low as possible in order to obtain high CO removal.

$$CO + H_2O \leftrightarrow CO_2 + H_2 \qquad \text{Equation 2.2}$$

Wieder et al. reported that ceria-supported Pd catalysts show higher reaction rates than ceria and Pd/Al_2O_3 catalysts because cerium is able to change its oxidation state from Ce^{+3} to Ce^{+4} [21]. Shido et al. reported that in the presence of Rh, the local electronic structure and morphology of surface around the reaction site change. Also, oxygen can be transferred from ceria to Rh particles at low temperatures and then, it can be used to oxidize CO to CO_2 [22][23].

Volatile organic compounds (VOCs), mainly 2-propanol, toluene and methanol, are air pollutants emitted from many different industrial processes. Therefore, the combustion of VOCs is very important for human life. Scire et al. reported that Au/CeO_2 catalysts have high activity for VOCs combustion by weakening Ce-O bond and enhancing oxygen mobility in order to oxidize VOCs through Mars-van Krevelen mechanism [24].

2.1.2. Ceria Oxygen Storage Capacity and Oxygen Exchange Kinetics

It is known that due to its fluorite structure, ceria has high oxygen mobility and fast oxygen exchange kinetics by changing its oxidation states between $Ce^{+3}$and Ce^{+4} rapidly under O_2-lean and O_2-rich conditions. In TWCs, the high ability of creating oxygen vacancies in a redox cycle of ceria is well proved [18].

Oxygen storage capacity (OSC) can be correlated with the most reactive oxygen species and the most readily available oxygen atoms. OSC measurements are performed to evaluate the redox properties. Martin et al. suggested OSC mechanism in three steps for ceria [25];

1. Dissociative adsorption and desorption of oxygen on metals
2. Transfer of active oxygen from metal to support and surface migration of these species on support
3. Oxygen storage by ceria

OSC can be measured by temperature programmed reduction (TPR) experiments in which a reducing gas (H_2 or CO) passes through the oxide while increasing the temperature to determine the oxygen release capacity and temperature programmed oxidation (TPO) experiments in which oxygen uptake capacity can be measured by oxidizing the reduced oxide under oxygen rich environment (O_2, O_2 mixtures, NO, H_2O) [14][15]. Reactions for reducing and oxidizing conditions are given.

Reducing conditions;

$2CeO_2 + H_2 \rightarrow Ce_2O_3 + H_2O$ Equation 2.3

$2CeO_2 + CO \rightarrow Ce_2O_3 + CO_2$ Equation 2.4

Oxidizing conditions;

$Ce_2O_3 + \frac{1}{2}O_2 \rightarrow 2CeO_2$ Equation 2.5

$Ce_2O_3 + NO \rightarrow 2CeO_2 + \frac{1}{2}N_2$ Equation 2.6

$Ce_2O_3 + H_2O \rightarrow 2CeO_2 + H_2$ Equation 2.7

OSC is also important in measuring the change of oxygen content of an oxide. In other words, the rate of oxygen release and uptake processes can be determined by OSC analysis.

Rao reported temperature programmed reduction (TPR) results on pure ceria samples with different surface areas. TPR was conducted under 5 % H_2-Ar at 20 ml/min flow rate while heating the sample in U-shaped reactor at a rate of 10 K/min. TCD detector was used to measure the oxygen release [26].

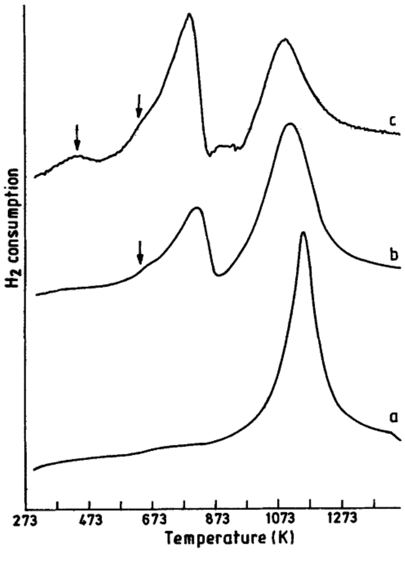

Figure 2.2 TPR pattern of CeO_2 samples with surface area (a) 1.5 m^2/g, (b) 30 m^2/g (c) 130 m^2/g (adapted from [26] with permission)

In Figure 2.2, TPR profiles of CeO_2 samples are given. It is reported that the first peak, around 578-873 K attributes to the surface reduction of ceria and the second peak, around 973-1273 K attributes to the bulk reduction of ceria. For low temperature region, it is seen that the unsaturated surface oxygen ions can easily capture hydrogen and produce water by creating anion vacancies. However, bulk oxygen should be transported to the surface before reduction by diffusion of surface anion vacancies into the bulk. Therefore, bulk reduction is observed in high temperature region. Additionally, increase in surface area of ceria samples results in an increase in hydrogen consumption from surface oxygen. Moreover, Johnson et al. reported that hydrogen consumption increases with the increase in surface area of oxide due to the fact that the reduction of cerium (III) ions corresponds to the transportation of one fourth of the surface oxygen ions. Therefore, OSC is strongly dependent on the surface area of ceria [27].

There are several studies available in the literature about the measurements of additive effect (Zr, Gd, Pr, Tb, Pb) on OSC of ceria [26][28][29].

Especially, OSC studies on CeO_2-ZrO_2 solid solutions have gained an attention because of its wide use in TWCs and steam methane reforming. Trovarelli et al. reported that the addition of ZrO_2 to CeO_2 lattice strongly affects the reduction kinetics of ceria by modifying the fluorite lattice. Introducing Zr^{+4} ions to the lattice and substituting Ce^{+4} ions, ionic radius decreases. Therefore, reduction of solid solution can occur more easily than ceria [28].

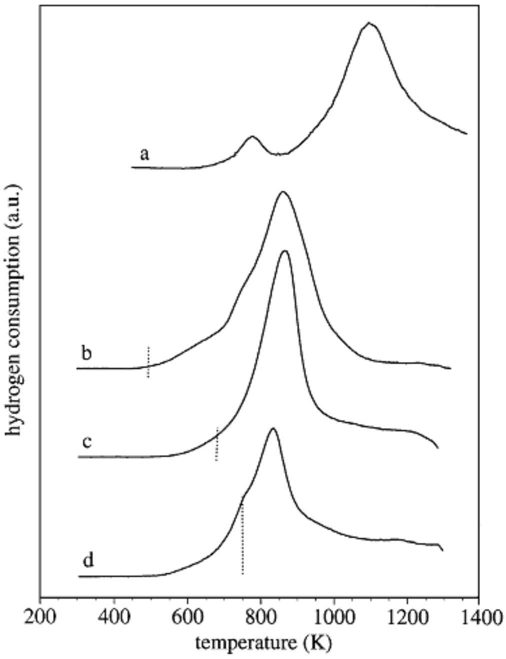

Figure 2.3 TPR pattern of (a) CeO_2, (b) $Ce_{0.2}Zr_{0.8}O_2$ (c) $Ce_{0.5}Zr_{0.5}O_2$, (d) $Ce_{0.8}Zr_{0.2}O_2$ (adapted from [28] with permission)

In Figure 2.3, it is seen that TPR profiles of CeO_2-ZrO_2 solutions are completely different from ceria. Both surface and bulk reduction peaks are merged in solid solutions which can be explained by the facile migration of oxygen ions in the CeO_2-ZrO_2 lattice. Complete reduction for ZrO_2-added ceria samples is observed in the range of 600-1100 K which is much less than pure ceria indicating the OSC dependence on structural properties [26].

Pt-BaO containing CeO_2-ZrO_2 mixed oxides are also studied by Uner et al. for NO_x reduction [30][31]. It is reported that alumina-zirconia containing catalyst shows no significant amount of hydrogen consumption whereas ceria containing catalyst consumes remarkable amount hydrogen at nearly 573 K. Moreover, it is reported that addition of zirconia to ceria results in the shift in reduction peaks of ceria to lower temperatures mainly due to the incorporation of zirconium in ceria lattices. TPR profile of Pt/BaO/$Ce_{0.25}Zr_{0.75}O_2$ mixed oxide is given in Figure 2.4.

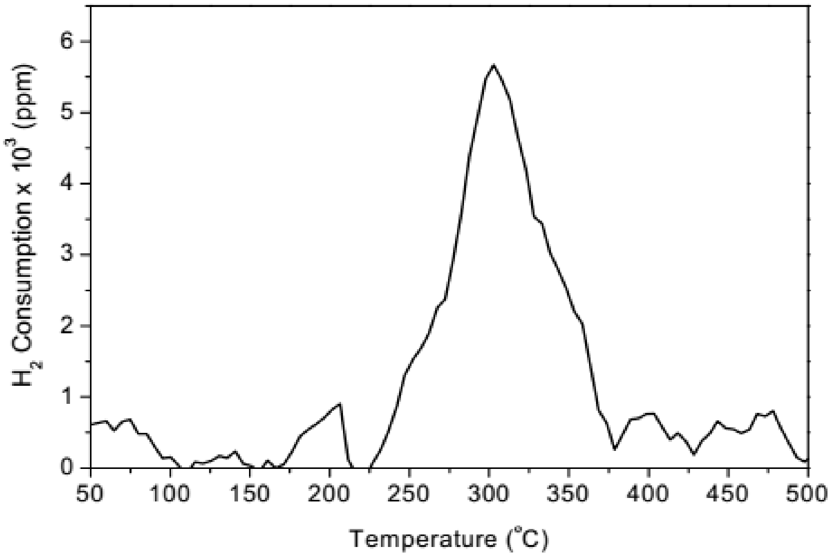

Figure 2.4 TPR pattern of Pt/BaO/$Ce_{0.25}Zr_{0.75}O_2$ (adapted from [31] with permission)

CeO_2 supported Al_2O_3 oxides are commonly studied in the literature in terms of OSC. Haneda et al reported that the hydrogen uptake is strongly dependent on the interaction between two oxides [32]. Shyu et al. also performed TPR experiments on CeO_2/Al_2O_3 samples with different ceria loadings. It is reported that in addition to the surface reduction peak of ceria (nearly at 723 K) and bulk reduction peak of ceria (nearly at 1073 K), peaks at nearly 573 K, 683 K and 993 K attribute to the adsorbed oxygen on alumina, reduction of surface oxygen of $CeAlO_3$ and partially reduced $CeAlO_3$, respectively. Additionally, increase in ceria loading results in two additional peaks at nearly 873 K and 1073 K which correspond to bulk reduction of ceria [33].

2.1.2.1. The Effects of Precious Metals on Ceria Oxygen Exchange Kinetics

Addition of low percentages of precious metals (Pt, Pd, Rh) on ceria or ceria-containing oxides greatly changes the redox properties by promoting the reduction of surface oxygen as determined by a shift in surface reduction TPR peak to lower temperatures [34][35].

Trovarelli et al. studied different precious metals doped on ceria. In Figure 2.5, TPR profiles of different M/CeO_2 oxides are given. It is seen that a new peak in the range of 300-450 K is due to the reduction of precious metals. The intensity of this low temperature peak is high because hydrogen consumption is higher than the reduction of metal precursor so that the surface Ce^{+4} reduction occurs simultaneously at this temperature range [14].

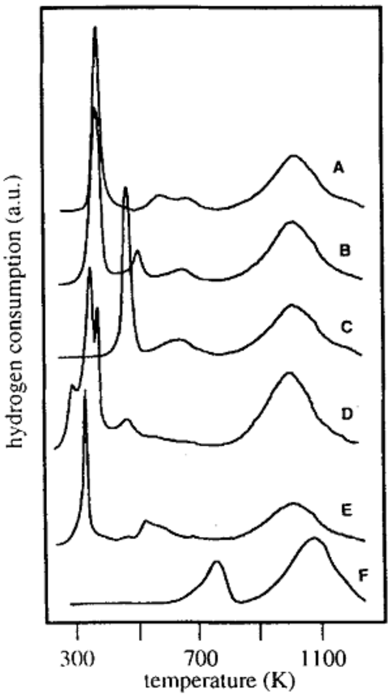

Figure 2.5 TPR pattern of (A) Ir/CeO_2 (B) Pd/CeO_2 (C) Pt/CeO_2 (D) Ru/CeO_2 (E) Rh/CeO_2 (F) CeO_2 (adapted from [14] with permission)

Uner et al. studied Pt/Al_2O_3, Pt/CeO_2 and Pt/CeO_2-Al_2O_3 catalysts for CO oxidation [36]. They reported that activation energy is lowered by nearly 50 kJ/mol when Pt/CeO_2 is used as a catalyst instead of Pt/Al_2O_3 mainly due to the difference in heat of CO adsorption. Moreover, reaction mechanism changes for these two catalysts. For Pt/Al_2O_3, oxygen dissociation or dissociative adsorption of oxygen happens over the catalyst while for Pt/CeO_2, CO is adsorbed onto surface and first, it uses the surface oxygen atoms of ceria and then, it uses the bulk oxygen atoms of ceria by reverse spillover with the help of platinum surface.

Therefore, it can be concluded that the presence of Pt enhances the oxygen mobility of CeO_2.

2.1.2.2. Metal Support Interactions

In catalysis, the aim of support usage is generally to disperse and to stabilize small metal particles. Besides these effects, other interactions at metal-support interface can be observed. Metal support interactions directly affect the chemisorption and catalytic properties of metal and support oxide by changing the chemical bond structure between metal and support in addition to the electronic properties. In general, metal support interactions in M-CeO systems are studied under H_2 and O_2 at high temperature applications.

Brogan et al. studied Pt/CeO_2 oxide in Raman spectroscopy under oxidizing conditions and they reported that on the ceria surface, Pt-O species form in high temperature calcination in addition to the stabilization of Pt toward dispersion [37]. The effect of Al_2O_3 addition on Pt/CeO_2 oxide reported in the literature that Pt strongly interacts with ceria and Pt^{+2} forms on Pt/CeO_2/Al_2O_3 surface. Moreover, at high temperatures, Pt migrates from Pt/Al_2O_3 to CeO_2/Al_2O_3 under oxidizing conditions and this migration increases the activity in CO oxidation with the help of dispersed Pt on CeO formation. It is also reported that Pt enhances the bulk oxidation of $CeAlO_3$/Al_2O_3 to CeO_2/Al_2O_3 and the reduction of CeO_2/Al_2O_3 to $CeAlO_3$/Al_2O_3 [38].

Shyu et al. reported that Pd has the similar effects with Pt in CeO_2/Al_2O_3 systems. Similarly, Pd facilitates the formation of $CeAlO_3$ to CeO_2/Al_2O_3 and under oxidizing atmosphere, ceria aids the formation of Pd-O which improves the metal dispersion. However, in cycle applications, Pd-O surfaces cause sintering and agglomeration [39].

Under reducing conditions, generally H_2 or CO atmosphere, metal support interactions are defined as strong metal support interactions (SMSI). Kepinski et al. reported that reduced ceria encapsulates the Pd and Pd-Ce forms at the temperatures higher than 873 K [40]. Monterio et al. reported that in Pd/CeO_2-Al_2O_3 oxide, Pd-Ce interaction is enhanced by the higher degree of contact area between Pd and Ce so that the redox activity increases and redox temperature decreases by facilitating oxygen vacancy formation and ceria stabilizes the Pd particles [41].

Farmer et al. also studied Ag-CeO_2 and Ag-MgO interactions by performing calorimetric measurements [42][43]. In this study, they measured adsorption energies of Ag gas atoms onto clean CeO_2 and MgO surfaces. They reported that Ag nanoparticles are more stable (30-70 kJ/mole of Ag) on CeO_2 (111) than on MgO (100) due to the fact that Ag atoms strongly bind to the vacant sites of ceria. They reported that adsorption of Ag starts at 250 kJ/mol to surface defects (steps, kinks and oxygen vacancies), quickly increases at 275 kJ/mol and slowly increases to 285 kJ/mol. Therefore, it can be concluded that surface defects and vacancies increase the adsorption energy of Ag to ceria. They confirmed that low adsorption energies can be attributed to the more stable particles and therefore, slow sintering occurs mainly because of the thermodynamic driving forces for sintering.

2.1.2.3. Activation Energies of Different Reactions: Pd/CeO_2 Used as Catalyst

There are several studies conducted on the calculation of kinetic parameters; such as activation energy, pre-exponential factor, reaction order etc. for different reactions in which Pd/CeO_2 used as catalyst.

In Table 2.1, a literature review of different studies over CeO_2 and Pd/CeO_2 is given. It is seen that in general, addition of Pd decreases the activation energy. However, parameters such as synthesis conditions and operation temperature also significantly affect the activation energy.

Table 2.1 Activation energies of CeO_2 and Pd/CeO_2 for different reactions reported in the literature

Reference	**Reaction**	**Catalyst**	**Activation Energy (kJ/mol)**
Bunluesin et al. [44]	Water gas shift	CeO_2	62.8
		Pd/CeO_2 (low T)	46.1
		Pd/CeO_2 (high T)	87.9
Wen et al. [45]	Water gas shift	Pd/CeO_2 (nanoclusters)	34.0
		Pd/CeO_2 (nanorod)	76.0
Stavroula et al. [46]	CO oxidation	1.3 nm Pd/CeO_2	8.0
		1.8 nm Pd/CeO_2	9.5
		16.4 nm Pd/CeO_2	21.1
Craciun et al. [47]	Methane steam reforming	CeO_2	57.3
		Pd/CeO_2	54.8
		Pd/CeO_2 (reduced)	146.0
Yee et al. [48]	Ethanol reforming	CeO_2	75.0
		Pd/CeO_2	40.0

Wang et al. reported that precious metal doped ceria catalysts show higher activities for CO, NO_x and hydrocarbon conversions due to the fact that with the help of precious metals, oxygen storage capacity increases and lattice oxygen activation improves [49]. They performed reduction analyses on Pd/CeO_2 catalysts synthesized by sol-gel method and they concluded that increasing reduction ratio increases the activation energy. If Pd is doped to the CeO_2 lattice, only lattice oxygen activation will be observed and therefore, activation energy will be lower. However, it there is oxygen diffusion into the CeO_2 bulk, activation energy will be comparably higher.

2.2. Two Step Solar Thermochemical Hydrogen Production on Reducible Metal Oxides

Two step solar hydrogen production cycles have the following steps;

1. Solar decomposition of redox material at high temperatures by releasing the oxygen under inert atmosphere (endothermic)
2. Water splitting reaction at moderate temperatures on decomposed redox material to produce hydrogen (exothermic)

The process strongly depends on the material properties. Candidate materials for solar hydrogen production should have good redox properties. Thermodynamic analysis can be performed to select the appropriate materials and it indicates that high entropy gain by transformation into the low oxidation state is favorable. There are lots of redox pairs indicating negative entropy change making inappropriate to use in two-step water splitting cycles. Moreover, the temperature difference between decomposition and water splitting is important because of material sintering at decomposition and slow kinetics at water splitting.

In the literature, the solar thermochemical two step hydrogen production cycles have been studied extensively. Several metal/metal oxide combinations reported in different studies. In Table 2.2, most commonly used redox cycles are listed.

Table 2.2 Solar thermochemical hydrogen production cycles

Reference	**Redox pairs**	**Cycle type**	**Reactions**	**Thermal decomposition temperature (K)**	**Water splitting temperature (K)**
Steinfeld [50]	ZnO Zn	Volatile Stoichiometric	$ZnO \rightarrow Zn + \frac{1}{2}O_2$ $Zn + H_2O \rightarrow ZnO + H_2$	2300	700
Kromer et al. [51]	CdO Cd	Volatile Stoichiometric	$CdO \rightarrow Cd + \frac{1}{2}O_2$ $Cd + H_2O \rightarrow CdO + H_2$	1723	773
Charvin et al. [52]	SnO_2 SnO	Volatile Stoichiometric	$SnO_2 \rightarrow SnO + \frac{1}{2}O_2$ $SnO + H_2O \rightarrow SnO_2 + H_2$	1873	873
Nakamura [53]	Fe_3O_4 FeO	Nonvolatile Stoichiometric	$Fe_3O_4 \rightarrow 3FeO + \frac{1}{2}O_2$ $3FeO + H_2O \rightarrow Fe_3O_4 + H_2$	2500	1000
Agrafiotis et al. [54]	$NiFe_2O_4$ $Ni_yFe_{1-y}O$	Nonvolatile Stoichiometric	$NiFe_2O_4 \rightarrow 3Ni_yFe_{1-y}O + \frac{1}{2}O_2$ $3Ni_yFe_{1-y}O + H_2O \rightarrow NiFe_2O_4 + H_2$	1673	1373
Scheffe et al. [55]	$La_{1-x}Sr_xMnO_3$ $La_{1-x}Sr_xMnO_{3-\delta}$	Nonvolatile Nonstoichiometric	$La_{1-x}Sr_xMnO_3 \rightarrow La_{1-x}Sr_xMnO_{3-\delta} + \frac{\delta}{2}O_2$ $La_{1-x}Sr_xMnO_{3-\delta} + \delta H_2O \rightarrow La_{1-x}Sr_xMnO_3 + \delta H_2$	1723	1623

McDaniel et al. [56]	$La_{1-x}Sr_xMn_yAl_{1-y}O_3$ $La_{1-x}Sr_xMn_yAl_{1-y}O_{3-\delta}$	Nonvolatile Nonstoichiometric	$La_{1-x}Sr_xMn_yAl_{1-y}O_3 \rightarrow La_{1-x}Sr_xMn_yAl_{1-y}O_{3-\delta} + \frac{\delta}{2}O_2$ $La_{1-x}Sr_xMn_yAl_{1-y}O_{3-\delta} + \delta H_2O \rightarrow La_{1-x}Sr_xMn_yAl_{1-y}O_3 + \delta H_2$	1623	1273
Abanades et al. [9]	CeO_2 Ce_2O_3	Nonvolatile Stoichiometric	$2CeO_2 \rightarrow Ce_2O_3 + \frac{1}{2}O_2$ $Ce_2O_3 + H_2O \rightarrow 2CeO_2 + H_2$	2273	773
Chueh et al. [57]	CeO_2 $CeO_{2-\delta}$	Nonvolatile Nonstoichiometric	$CeO_2 \rightarrow CeO_{2-\delta} + \frac{\delta}{2}O_2$ $CeO_{2-\delta} + \delta H_2O \rightarrow CeO_2 + \delta H_2$	1873	1073
Le Gal et al. [58]	$Ce_{0.25}Zr_{0.75}O_2$ $Ce_{0.25}Zr_{0.75}O_{2-\delta}$	Nonvolatile Nonstoichiometric	$Ce_{0.25}Zr_{0.75}O_2 \rightarrow Ce_{0.25}Zr_{0.75}O_{2-\delta} + \frac{\delta}{2}O_2$ $Ce_{0.25}Zr_{0.75}O_{2-\delta} + \delta H_2O \rightarrow Ce_{0.25}Zr_{0.75}O_2 + \delta H_2$	1673	1323
Kaneko et al. [11]	$Ce_{8.9}Fe_{1.1}O_2$ $Ce_{8.9}Fe_{1.1}O_{2-\delta}$	Nonvolatile Nonstoichiometric	$Ce_{8.9}Fe_{1.1}O_2 \rightarrow Ce_{8.9}Fe_{1.1}O_{2-\delta} + \frac{\delta}{2}O_2$ $Ce_{8.9}Fe_{1.1}O_{2-\delta} + \delta H_2O \rightarrow Ce_{8.9}Fe_{1.1}O_2 + \delta H_2$	1673	1273
Kaneko et al. [60]	$Ce_{0.9}Mn/Ni_{0.1}O_2$ $Ce_{0.9}Mn/Ni_{0.1}O_{2-\delta}$	Nonvolatile Nonstoichiometric	$Ce_{0.9}Mn/Ni_{0.1}O_2 \rightarrow Ce_{0.9}Mn/Ni_{0.1}O_{2-\delta} + \frac{\delta}{2}O_2$ $Ce_{0.9}Mn/Ni_{0.1}O_{2-\delta} + \delta H_2O \rightarrow Ce_{0.9}Mn/Ni_{0.1}O_2 + \delta H_2$	1773	1273

2.2.1. Volatile Cycles

Volatile redox pairs, showing phase transition in decomposition step due to their low melting and boiling temperatures, are employed in two step solar thermochemical hydrogen production cycles. The phase transition is thermodynamically advantageous because it creates an increase in entropy. However, the possibility of recombination of product gases are high for these volatile redox pairs so that quenching or gas phase separation at high temperatures are required.

There are three main volatile redox pairs discussed in the literature: ZnO/Zn, CdO/Cd and SnO_2/SnO.

ZnO/Zn volatile cycle is one of the most promising candidates for solar thermochemical hydrogen production cycles due to its favorable material and thermodynamic properties. Molar mass of Zn is 65.38 g/mol which results in high energy content per mass. This makes Zn attractive for transportable energy. In terms of thermodynamics, the volatility of ZnO oxide results in more favorable decomposition due to the steeper change of Gibbs free energy with temperature. Accordingly, because of large change in Gibbs free energy, ZnO is attractive for thermochemical cycles. First step for this process is the solar decomposition of $ZnO_{(s)}$ to $Zn_{(g)}$ that occurs at approximately at 2300 K. Second step is the hydrogen production on $Zn_{(g)}$ via water splitting at nearly 700 K [61]. Although ZnO/Zn cycle is very suitable for solar thermochemical hydrogen production, the process has separation problems. After decomposition, the product gases (Zn and O_2) should be separated or quenched at high temperatures to prevent reoxidation because melting and boiling temperatures of Zn are 693 K and 1180 K, respectively [50][62].

CdO/Cd is a volatile cycle for which decomposition and water splitting temperatures are reported as 1723 K and 773 K, respectively. CdO/Cd cycle should also have Cd vapor quenching step after decomposition. Major disadvantage for this cycle is that cadmium has operation challenges due to its toxicity [51]. Additionally, because Cd melting and boiling temperatures are low (594 K and 1040 K), separation of product gases is essential for this system [63].

A two-step thermochemical volatile cycle based on SnO_2/SnO proposed for solar hydrogen production. First step is the solar decomposition of SnO_2 to SnO at high temperatures, about 1873 K [52]. Decomposition of SnO to metallic Sn is also proposed in the literature however it is hard to separate metallic Sn from SnO_2 and water splitting reaction with metallic Sn is considerably slow [64]. Therefore, second step is the direct reaction of SnO with water to produce hydrogen which operates at 873 K [52]. Because SnO boiling temperature is 1800 K, the products are gaseous [62]. Hence, quench is necessary to prevent recombination reactions. This volatile cycle consists of solid-gas reactions only which makes the operation easier and simplifies the separation of products.

2.2.2. Nonvolatile Cycles

Nonvolatile redox pairs, including a wide variety of single-metal, multi-metal and multivalent metal oxides, are commonly used in solar thermochemical hydrogen production. These nonvolatile redox materials remain in solid state during both decomposition and water splitting processes which make them more viable. The physicochemical properties of nonvolatile redox materials such as surface area, particle size, porosity etc. are very important for decomposition and water splitting reactions. Therefore, there are many studies reported in the literature to enhance these properties not only in synthesis phase but also during repeated thermochemical cycles. Additionally, material screening and evaluation in terms of the capability of releasing oxygen and adsorbing water are very important for solar thermochemical hydrogen production based on nonvolatile redox pairs.

There are many studies reported in the literature about nonvolatile redox pairs for solar thermochemical hydrogen production. Ferrites (Fe_3O_4, $NiFe_2O_4$ $ZnFe_2O_4$, $CoFe_2O_4$, $Ni_{0.5}Mn_{0.5}Fe_2O_4$, $Mn_{0.5}Zn_{0.5}Fe_2O_4$ etc.), perovskites ($La_{1-x}Sr_xMnO_3$, $La_{1-x}Sr_xFeO_3$, $La_{1-x}Sr_xCo_yFe_{1-y}O_3$, $La_{1-x}Sr_xMn_yFe_{1-y}O_3$ etc.) and stoichiometric-nonstoichiometric ceria have been demonstrated recently.

The Fe_3O_4/FeO redox cycle is the first cycle proposed for solar thermochemical hydrogen production by Nakamura [53]. In this cycle, the first reaction is the decomposition of magnetite to wustite (Fe_3O_4 to FeO) proceeding at 2500 K, highly endothermic and the second reaction is water splitting on FeO, slightly exothermic proceeding at 1000 K. In theory, this redox pair has excellent properties for solar thermochemical hydrogen production. However, extremely high temperatures are required for decomposition step exceeding the melting temperatures of Fe_3O_4 and FeO and causing a rapid deactivation of iron oxide particles. Hence, magnetite/wustite cycle is not a good candidate in practice [65].

In order to decrease the decomposition temperature of iron oxide by lowering the activation energy, spinel ferrites having a formula of MFe_2O_4 (M: Zn, Ni, Co, Cu etc.) have been reported in the literature [5][67]. Since high temperatures are required for decomposition step, Zn containing ferrite materials have volatilization problems. Mn containing ferrites materials exhibit stability problems during thermochemical cycles due to the fact Mn is not a stable element at high temperatures [5]. Fresno et al. reported that after first decomposition-oxidation cycle, the hydrogen production amount decreases in the order of $NiFe_2O_4$, $ZnFe_2O_4$ and $CuFe_2O_4$ [66]. Although, Ni-ferrites indicate good performances on solar decomposition and water splitting after first cycle, Kodama et al. reported that sintering occurs at high temperature and that makes Ni-ferrite materials not suitable for cycling [68].

Perovskite materials, having a formula of ABO_3, are nonstoichiometric compounds that have high oxygen release and uptake capacities at high temperatures. These materials are commonly used in solid oxide fuel cells [69]. In the recent years, several studies indicate that perovskite materials have an ability to split water. Especially, La-containing perovskites ($La_{1-x}Sr_xMnO_3$, $La_{1-x}Sr_xMn_yAl_{1-y}O_3$ etc.) indicate good performances on solar hydrogen production cycles. It is reported in the literature that for La-Sr-Mn perovskites, thermogravimetric decomposition and oxidation experiments observed in the range of 1723-1623 K and 1623-1273 K, respectively [55][56].

2.2.3. Ceria for Use in Solar Thermochemical Cycles

Ceria has been commonly used in many applications such as automotive emission catalyst, oxidation catalyst, reforming catalyst and anode for solid oxide fuel cells due to the fact that it has a high capability of oxygen release and uptake [34][69][70]. In addition to the common use of ceria in automotive catalysts, Otsuka et al. proposed hydrogen production mechanism over hydrogen-reduced ceria via water splitting [71]. Recently, ceria has gained an attention as one of the most promising materials for solar driven two step hydrogen production because of its attractive redox properties.

Solar thermochemical hydrogen production via water splitting by using ceria was firstly suggested by Abanades et al. [9]. They reported a thermochemical stoichiometric CeO_2/Ce_2O_3 redox cycle system for solar hydrogen production consisting of two steps; stoichiometric decomposition of CeO_2 to Ce_2O_3 at 2273 K, 100-200 mbar in solar reactor under an inert atmosphere and complete conversion of Ce_2O_3 to CeO_2 with water at 673-873 K for production of hydrogen because of high reactivity of Ce_2O_3. They successfully proved that ceria is stable at ambient temperatures and it can be used as a hydrogen tank since heating ceria in the presence of water can generate hydrogen rapidly. This allows to produce on-board hydrogen safely. However, in order to decompose ceria, high temperatures are required. Although it is possible to reach these temperatures with solar flux, in practice, there are some problems concerning the evaporation of ceria and high energy losses due to irradiation.

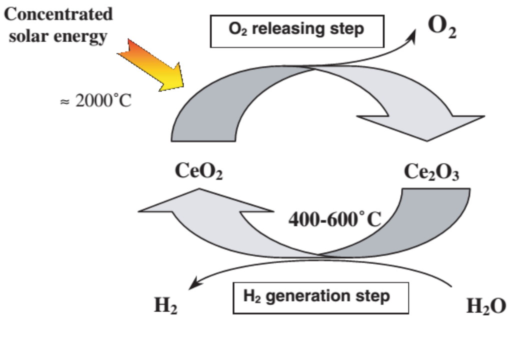

Figure 2.6 Schematic of solar two-step hydrogen production cycle based on CeO_2/Ce_2O_3 system (adapted from [9] with permission)

Therefore, scientists became interested in partially-decomposed ceria system without any melting problems because decomposition of ceria starts at nearly 1673 K under an inert atmosphere. Chueh et al. reported solar driven hydrogen production via water splitting on nonstoichiometric ceria consisting of two steps; oxygen release from CeO_2 to $CeO_{2-\delta}$ at 1873 K by using solar heat input and hydrogen release via water splitting at 1073 K [8][57]. They reported that hydrogen is generated rapidly over 500 cycles with high hydrogen yields [72].

Although ceria has high oxygen release capacity, it sinters at high temperatures and this situation results in the limitation of oxygen storage and release capacity [67]. By modifying ceria with other oxides while having the same crystal structure, it is possible to reduce the grain growth of ceria and to make the decomposition of ceria easier. The materials such as Mn, Fe, Co, Cu, Zn, Ni, Zr and yttria stabilized zirconia (YSZ) are reported in the literature as additives.

Petkovich et al. studied $Ce_{1-x}Zr_xO_2$ materials for solar water splitting systems. They reported that Zr can limit the crystalline growth and sintering successfully while improving the thermal stability [73]. Moreover, Le Gal et al. reported that Zr addition can decrease the decomposition temperature of ceria due to lattice deformation [58]. Kaneko et al. reported $Ce_{1-x}Fe_xO_2$ nonstoichiometric 12 cycles for solar hydrogen production by lowering the ceria decomposition temperature nearly 600 K [11]. Additionally, they proved that the amount of hydrogen evolved during water splitting reaction can be elevated by adding Mn and Ni to ceria as well as decreasing the decomposition temperature [60].

CHAPTER 3

MATERIALS AND METHODS

3.1. Materials

In order to synthesize supported oxides, four different chemicals are used; CeO_2 (cerium (IV) oxide, 99.9 %, Alfa Aesar), $Ce(NO_3)_3.6H_2O$ (cerium (III) nitrate hexahydrate, Merck), γ-Al_2O_3 (gamma-aluminum oxide, 99.97 %, Alfa Aesar) and $Pd(NO_3)_2$ (palladium (II) nitrate, 99.95 %, Alfa Aesar). Gases used in TPx experiments are 10 % H_2-Ar, 2 % O_2-He and He. Gases used in microcalorimetry experiments are H_2, O_2 and H_2O vapor.

3.1.1. Synthesis of 1 % Pd/CeO_2 with Incipient Wetness Method

1 wt. % Pd/CeO_2 oxide was prepared by incipient wetness method by using palladium (II) nitrate solution ($Pd(NO_3)_2$, 99.95 %, Alfa Aesar) and cerium (IV) oxide powder (CeO_2, 99.9 %, Alfa Aesar). Appropriate amount of $Pd(NO_3)_2$ solution was added to CeO_2 powder and this solution was impregnated over the support. The oxide dried at 120 °C overnight. Then, the oxide was calcined at 450 °C for 5 h at a rate of 5 °C/min.

3.1.2. Synthesis of 1 % Pd/Al_2O_3 with Incipient Wetness Method

1 wt. % Pd/Al_2O_3 oxide was prepared by incipient wetness method by using palladium (II) nitrate solution ($Pd(NO_3)_2$, 99.95 %, Alfa Aesar) and gamma-aluminum oxide (γ-Al_2O_3, 99.97 %, Alfa Aesar). Appropriate amount of $Pd(NO_3)_2$ solution was added to γ-Al_2O_3 powder and this solution was impregnated over the support. The oxide dried at 120 °C overnight. Then, the oxide was calcined at 450 °C for 5 h at a rate of 5 °C/min.

3.1.3. Synthesis of 1 % Pd/CeO_2-Al_2O_3 with Sequential Impregnation Method

1 wt. % Pd/CeO_2-Al_2O_3 oxides were prepared by sequential impregnation method using palladium (II) nitrate solution ($Pd(NO_3)_2$, 99.95 %, Alfa Aesar), cerium (III) nitrate hexahydrate ($Ce(NO_3)_3.6H_2O$, Merck) and gamma-aluminum oxide (γ-Al_2O_3, Alfa Aesar). Appropriate amount of cerium (III) nitrate hexahydrate ($Ce(NO_3)_3.6H_2O$, Merck) was dissolved in a sufficient amount of deionized water and appropriate amount of gamma-aluminum oxide (γ-Al_2O_3, Alfa Aesar) was added to the solution. The solution was stirred for 24 h and dried at 110 °C for 2 h. After that, prepared oxide was calcined at 400 °C for 6 h at a rate of 2 °C/min. After preparing CeO_2-Al_2O_3 (20:80, 15:85, 10:90 wt:wt) oxides, 1 wt. % Pd/CeO_2-Al_2O_3 was prepared by incipient wetness method by using palladium (II) nitrate solution ($Pd(NO_3)_2$, 99.95 %, Alfa Aesar). Appropriate amount of $Pd(NO_3)_2$ solution was added to CeO_2-Al_2O_3 powder and this solution was impregnated over the support. The oxide dried at 120 °C for 3 days.

3.2. Characterization

3.2.1. BET Analysis

Surface area characterization was performed by using Micromeritics TriStar II Surface Area and Porosity equipment under nitrogen flow at a 10 °C/min heating rate. Prepared oxide was degassed for 3 h at 150 °C for the removal of moisture and other adsorbed gases on the surface by using Micromeritics VacPrep 061 Sample Degas System.

3.2.2. XRD Analysis

XRD analysis was performed for 1 % Pd/CeO_2-Al_2O_3 oxides by using Rigaku Ultima-IV X-Ray Diffractometer (Rigaku XRD, -30kV, 15mA- with Cu Kα radiation, λ=1.54Å) equipment for scattering angle 10 to 70 ° with 1 °/min rate. Crystal were compared with Rigaku ICDD database.

3.2.3. TPx Analyses

TPx analyses were performed using Micromeritics Chemisorp 2720. Detailed information about the equipment is given in Appendix A.

Temperature programmed reduction (TPR), temperature programmed oxidation (TPO) and temperature programmed thermal decomposition (TPtD) experiments were performed to measure oxygen release/uptake capacity of prepared oxides.

TPx experiments were performed in Micromeritics ChemiSorb 2720 flow chemisorption system given in Figure 3.1 below.

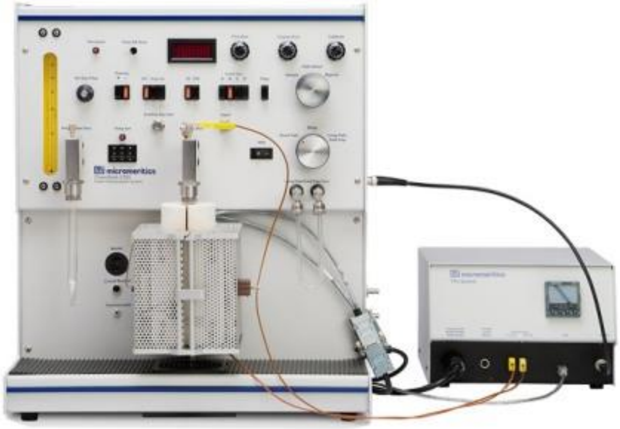

Figure 3.1 Micromeritics ChemiSorb 2720 TPx equipment

A sample was placed in a u-shaped quartz reactor on a quartz wool bed and positioned vertically in a programmable furnace in Micromeritics ChemiSorb 2720. A furnace was locked and isolation wool was placed on the top of the furnace. For TPR measurements, cold trap was installed to capture the water formed during reaction. After placing the sample, by-pass and short path lines were purged with helium. Then, sample and long path lines were also purged with helium. Purging was completed when the TCD signal was almost stable. After purging the system with helium, gas port was adjusted to a suitable reaction gas for experiment. Temperature programmed reduction (TPR) was performed under hydrogen flow (10 % H_2-Ar) to analyze the reducibility of prepared oxide. Temperature programmed thermal reduction (TPtD) was performed under helium flow (He) to decompose the prepared oxide. Temperature programmed oxidation (TPO) was performed under oxygen flow (2 % O_2-He) to oxidize the reduced or decomposed oxide. After stabilizing the TCD signal under reaction gas flow, maximum temperature, ramp and dwell time were set and sample was started to be heated. TCD signal and temperature data were recorded by software. After completion of heating, sample was cooled by using fan.

A stepwise experimental procedure for TPx experiments is given in Appendix B.1.

For prepared oxides, firstly, temperature programmed reduction (TPR) was performed under hydrogen flow (10 % H_2-Ar) to analyze the reducibility of prepared oxide. After first oxidation, two-step cycle was simulated with beginning of temperature programmed thermal decomposition (TPtD) under an inert atmosphere (He) and it was followed by temperature programmed oxidation (TPO) under oxygen flow (2 % O_2-He).

3.2.4. Chemisorption

Adsorption measurements were performed in home built pyrex manifold equipped with vacuum tight Ace glass stopcocks given in Figure 3.2 below.

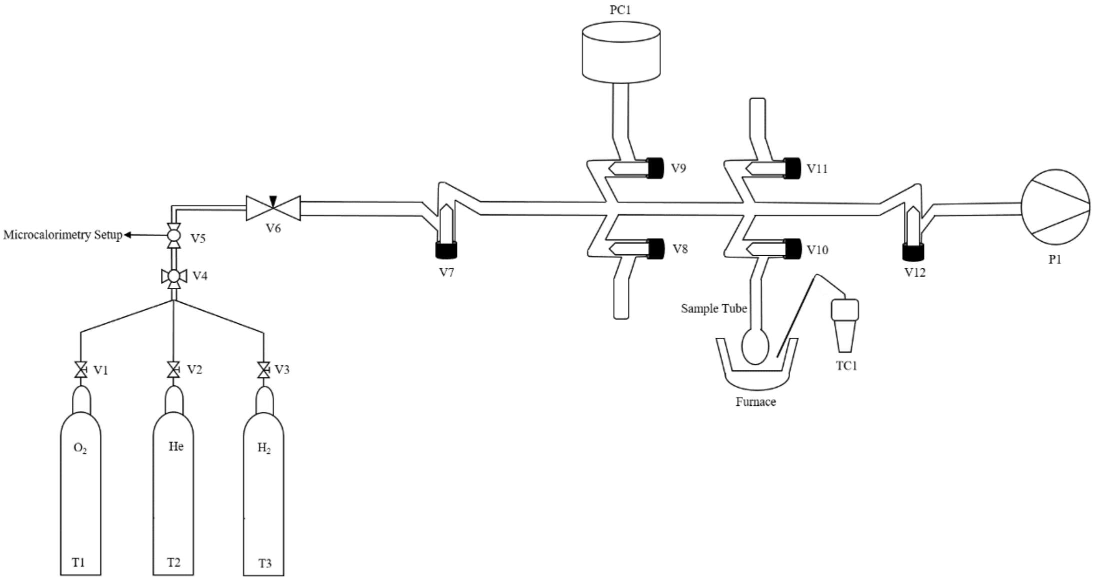

Figure 3.2 Drawing of chemisorption manifold

This pyrex equipment built in the lab contains a multiport high vacuum pyrex glass manifold, a turbo molecular pump (Varian 9699171) to vacuum the system, a pressure gauge (MKS Baratron Capacitance Manometer), a digital power supply (MKS PR4000B) to monitor the pressure data, vacuum tight Ace glass stopcocks, a thermometer and a heater. This pyrex manifold is suitable for vacuum operation better than 10^{-6} Torr. Samples were held in pyrex sample cell and it was heated by using heater and thermometer to adjust the temperature in the cell.

System was evacuated before attaching the sample cell to the system. While sample was heated up to 150 °C, system was purged with helium. Temperature of the sample increased up to 350 °C and system was evacuated for 10 minutes. After the system was flushed with hydrogen, sample was reduced for 4 time with hydrogen at 350 °C. System was evacuated for 1 hour at 350 °C and overnight at room temperature after reduction. By dosing hydrogen at different pressures to the sample (~ 1-20 torr), total adsorption amount was measured. Again dosing hydrogen at different pressures (~ 1-20 torr), weak adsorption amount was measured.

A stepwise experimental procedure for chemisorption experiments is given in Appendix B.2.

3.2.5. Microcalorimetry

Heat of adsorption measurements were performed in home built pyrex manifold equipped with vacuum tight Ace glass stopcocks given in Figure 3.3 below.

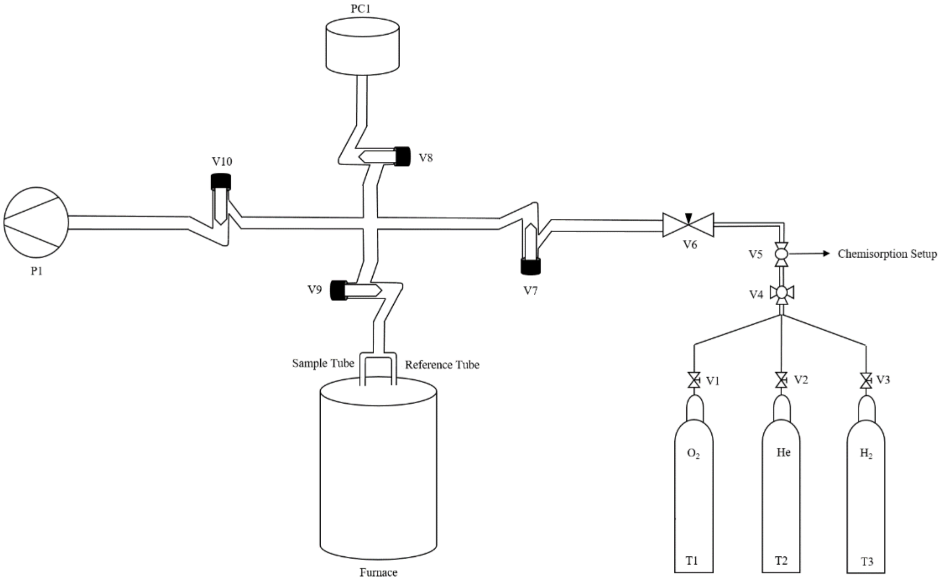

Figure 3.3 Drawing of microcalorimetry manifold

In this equipment, a calorimeter (Setaram C-80 TianCalvet) is connected to the multiport high vacuum pyrex glass manifold. There are also a turbo molecular pump station (Pfeiffer TCP 015, Pfeiffer TMH 065) to vacuum the system, a pressure gauge (MKS Baratron Capacitance Manometer), a digital power supply (MKS PR4000B) to monitor the pressure data and vacuum tight Ace glass stopcocks in this equipment. Sample and reference cells are placed into the calorimeter and surrounded by more than 400 thermocouples.

After evacuating the microcalorimetry manifold, both sample cell and reference cell were placed into calorimetry. Sample was heated up to 250 °C and hydrogen was dosed to the sample to reduce the surface. After reduction, sample was cool down to 150 °C and depending on the oxygen or hydrogen adsorption experiments, oxygen or hydrogen at different pressures (~ 0-200 torr) was dosed to the sample. Heat of adsorption data can be calculated by using enthalpy data given by the software.

A stepwise experimental procedure for microcalorimetry experiments is given in Appendix B.3.

3.3. Kinetic Analysis

3.3.1. Redhead Method

Activation energies for desorption analysis can be calculated by the Redhead method. In this method, for an n^th order process, material balance around the reactor can be written as [74];

$$rate = -\frac{dC}{dt} = k_0 . e^{-E_a/_{RT}} . C^n \qquad \text{Equation 3.1}$$

It is known that temperature is increasing linearly with time (Equation 3.2) and maximum rate can be calculated as (Equation 3.3);

$$T = T_0 + \alpha t \qquad \text{Equation 3.2}$$

$$\frac{d(rate)}{dT} = 0 \qquad \text{Equation 3.3}$$

Substituting Equation 3.1 and Equation 3.2 to Equation 3.3;

$$\frac{d(rate)}{dT} = k_0 . \frac{E_a}{R.T^2} . e^{-E_a/_{RT}} . C^n - \alpha^{-1} . \left[k_0 . e^{-E_a/_{RT}}\right]^2 . n . C^n \qquad \text{Equation 3.4}$$

For a 1st order process at the maximum temperature (T_p), activation energy can be calculated by using equation given below.

$$k_0 . e^{-E_a/_{R.T_p}} = \frac{\alpha . E_a}{R.{T_p}^2} \qquad \text{Equation 3.5}$$

For a given pre-exponential factor, heating rate and peak temperature, activation energy can be calculated for desorption data taken from such as TGA or TPtD. However, pre-exponential factor should be appropriately determined for this method.

3.3.2. Differential Method

Activation energies and pre-exponential factors for desorption analysis can also be calculated by differential method without any information about reaction order. For differential method, it is known that TCD signal can be used to determine the mol/min data, In(TCD signal) vs. 1/T is plotted. The slope and the intercept of this plot gives $-E_a/R$ and In(k_0), respectively.

3.3.3. Kissinger Method

Activation energies and pre-exponential factors for thermal analysis can also be determined by Kissinger method, an experimental method in which exothermic peak is recorded while the small amount of reacting material is heated at different heating rates with the assumption that at the peak temperature, conversion is constant. In this method, reaction order is assumed as first order [75].

The rate equation of first order reaction is given in Equation 3.6 below.

$$\frac{dx}{dt} = k(T).f(x) \qquad \text{Equation 3.6}$$

Rate constant can be calculated by using Arrhenius Equation.

$$k(T) = k_0.e^{(\frac{-E_a}{R.T})} \qquad \text{Equation 3.7}$$

The combination of Equation 3.6 and Equation 3.7 is given in Equation 3.8 below.

$$\frac{dx}{dt} = k_0.e^{(\frac{-E_a}{R.T})}.f(x) \qquad \text{Equation 3.8}$$

After differentiating Equation 3.8 with respect to time by using chain rule gives Equation 3.9;

$$\frac{d[\frac{dx}{dt}]}{dt} = k_0.e^{(\frac{-E_a}{R.T})}.\frac{d[f(x)]}{dt} + k_0.f(x).\frac{d\left[e^{(\frac{-E_a}{R.T})}\right]}{dt} \qquad \text{Equation 3.9}$$

Constant heating rate, dT/dt, can be identified as α and the term with constant heating rate can be rearranged.

$$\frac{d\left[e^{(\frac{-E_a}{R.T})}\right]}{dt} = \frac{E_a.\alpha}{R.T^2}.e^{(\frac{-E_a}{R.T})} \qquad \text{Equation 3.10}$$

It is assumed that at the peak temperature (T_p), conversion is constant.

$$0 = k_0.e^{(\frac{-E_a}{R.T_p})}.\frac{d[f(x)]}{dt} + k_0.f(x).\frac{E_a.\alpha}{R.{T_p}^2}.e^{(\frac{-E_a}{R.T_p})} \qquad \text{Equation 3.11}$$

$$0 = \frac{d[f(x)]}{dt} + f(x).\frac{E_a.\alpha}{R.{T_p}^2} \qquad \text{Equation 3.12}$$

Defining $f'(x) = \frac{d[f(x)]}{dx}$ and $\frac{d[f(x)]}{dt} = f' \frac{d\,x}{dt}$;

$$0 = k_0 . e^{(\frac{-E_a}{R.T_p})} . f'(x) + \frac{E_a.\alpha}{R.{T_p}^2} \qquad \text{Equation 3.13}$$

After rearranging and taking natural logarithm of Equation 3.13 gives Equation 3.14.

$$In\left[\frac{\alpha}{{T_p}^2}\right] = In\left[\frac{k_0.R}{E_a}\right] + In[-f'(x)] - \frac{E_a}{R.T_p} \qquad \text{Equation 3.14}$$

Since reaction is assumed to be first order reaction; $f'(x) = (1 - x)$ and $In[-f'(x)] = 0$, Equation 3.14 is arranged to Equation 3.15.

$$In\left[\frac{\alpha}{{T_p}^2}\right] = In\left[\frac{k_0.R}{E_a}\right] - \frac{E_a}{R.T_p} \qquad \text{Equation 3.15}$$

Equation 3.15 is the final form of Kissinger Equation. Plotting In[$\alpha/{T_p}^2$] vs. $1/T_p$, the slope of this plot gives $-E_a/R$ value and the intercept of this plot gives In[$k_0.R/E_a$]. Therefore, kinetic parameters can be calculated.

CHAPTER 4

RESULTS AND DISCUSSIONS

4.1. BET Results

BET surface areas for prepared oxides and used chemicals are given in Table 4.1.

Table 4.1 BET surface areas for used and synthesized materials

Oxide	**BET surface area (m^2/g)**
CeO_2 (Alfa Aesar)	2.9
1 % Pd/CeO_2	3.8
1 % Pd/20 % CeO_2-Al_2O_3	56.1
1 % Pd/15 % CeO_2-Al_2O_3	55.6
1 % Pd/10 % CeO_2-Al_2O_3	60.4
10 % CeO_2-Al_2O_3	69.1
1 % Pd/Al_2O_3	74.9
γ-Al_2O_3 (Alfa Aesar)	69.0

It is seen that adding high surface γ-Al_2O_3 to Pd/CeO_2 oxide increases the surface area. Low ceria loading results in slightly higher surface area mainly because of the fact that ceria stabilized Al_2O_3 and prevent its formation to α-Al_2O_3 [76].

4.2. XRD Results

Prepared 1 % Pd/CeO_2-Al_2O_3 oxides were examined with X-ray diffractometer. Diffraction lines were compared with the Rigaku ICDD database (CeO_2 card no: 75-0076, γ-Al_2O_3 card no: 26-0031, $CeAlO_3$ card no: 48-0051, SiO_2 card no: 11-0252). Moreover, for CeO_2-Al_2O_3 oxide, Haneda et al. reported XRD spectra given in Figure 4.1 below.

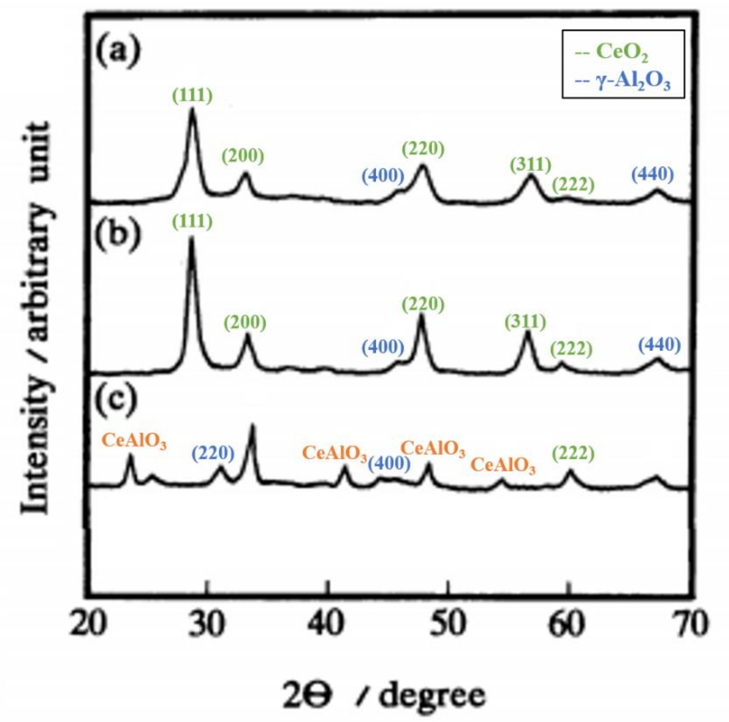

Figure 4.1 XRD spectra for (a) fresh (b) oxidized (c) reduced catalyst (adapted from [32])

XRD results for prepared 1 % Pd/CeO_2-Al_2O_3 oxides are given in Figure 4.2 for 1 % Pd/10 % CeO_2-Al_2O_3 after TPR-TPO, 1 % Pd/15 % CeO_2-Al_2O_3 after TPR and for 1 % Pd/20 % CeO_2-Al_2O_3 after TPR-TPO.

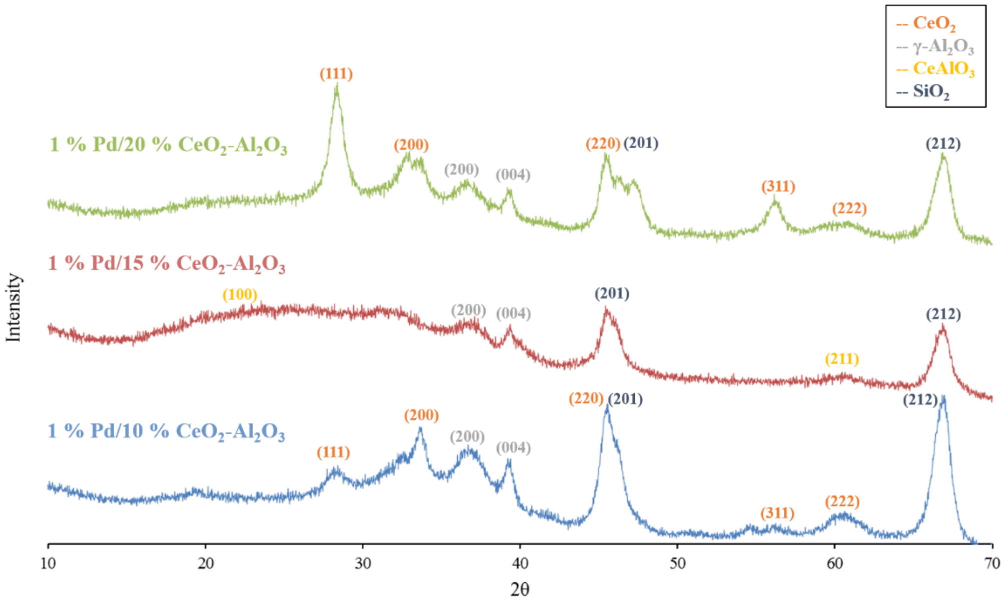

Figure 4.2 XRD spectra for 1 % Pd/20 % CeO$_2$-Al$_2$O$_3$ (oxidized), 1 % Pd/15 % CeO$_2$-Al$_2$O$_3$ (reduced), 1 % Pd/10 % CeO$_2$-Al$_2$O$_3$ (oxidized)

XRD results showed that characteristic peaks of CeO$_2$ and γ-Al$_2$O$_3$ were detected for oxidized oxides. However, for 1 % Pd/15 % CeO$_2$-Al$_2$O$_3$, no CeO$_2$ peaks can be observed. The reason is that all CeO$_2$ is reduced during TPR. In addition, CeAlO$_3$ peaks were observed for reduced sample. SiO$_2$ peaks were detected for all prepared oxides due to the presence of quartz wool in the samples.

4.3. TPx Results

4.3.1. TPR Results

The reducibility of prepared oxides was investigated by TPR.

In Figure 4.3 and Figure 4.4, TPR patterns for CeO_2 and 1 % Pd/CeO_2 at different heating rates are given.

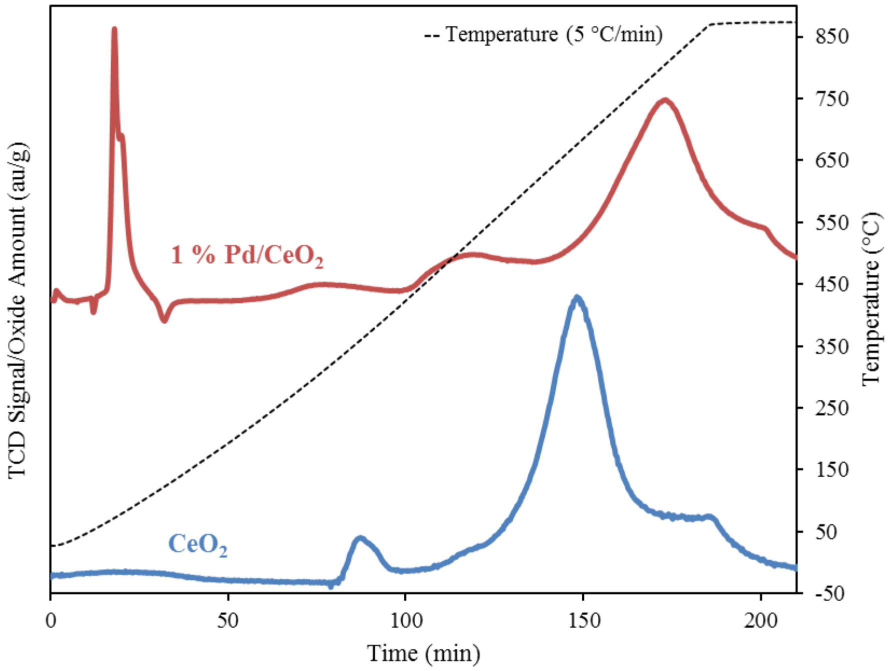

(a)

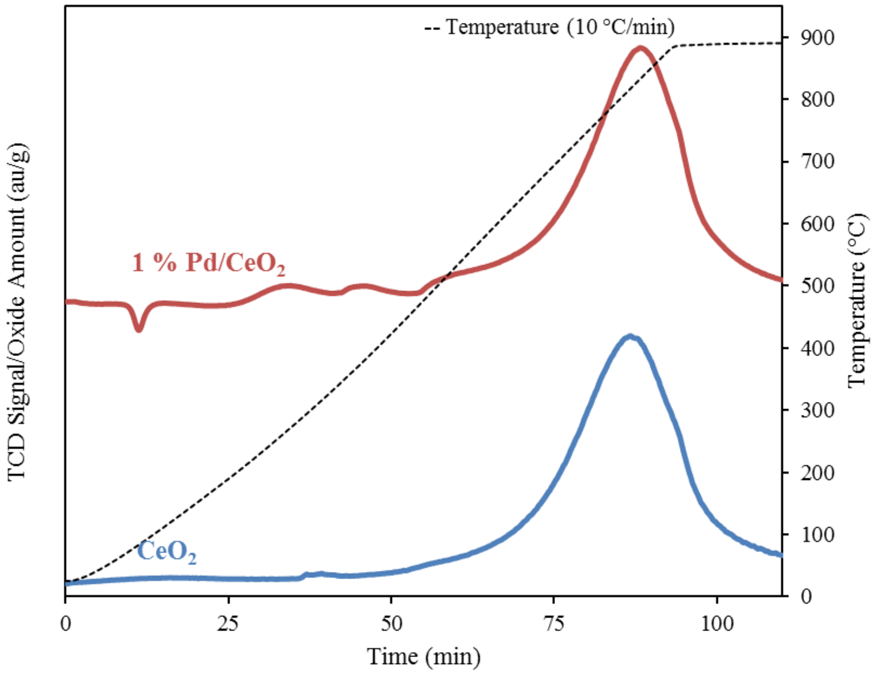

(b)

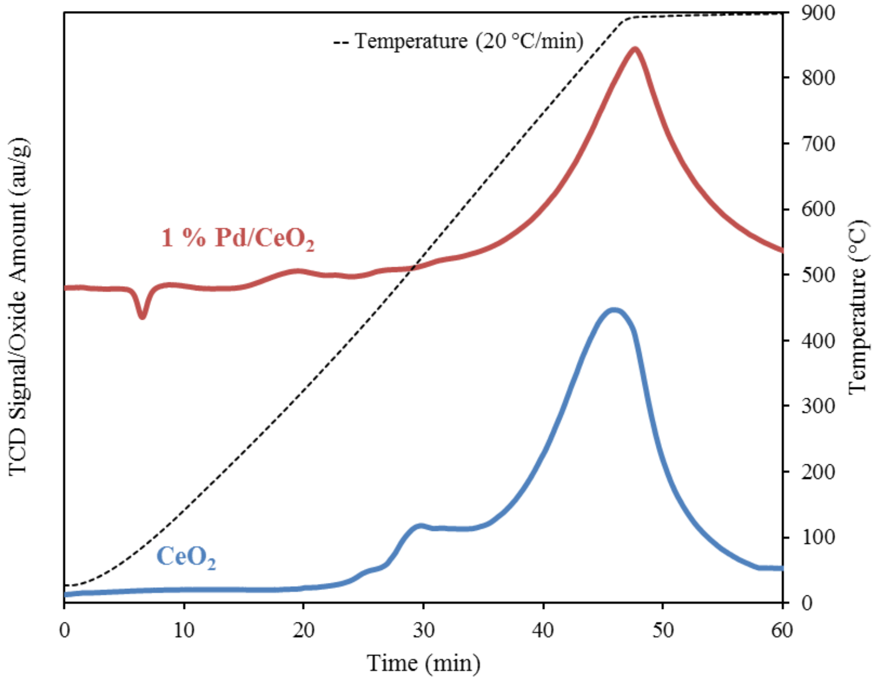

(c)

Figure 4.3 TPR pattern of CeO_2 and 1 % Pd/CeO_2 at (a) 5 °C/min (b) 10 °C/min and (c) 20 °C/min heating rates under 25 sccm 10 % H_2-Ar flow

For CeO_2, two main reduction peaks were observed in the temperature range of 350-600 °C and 600-800 °C which correspond to the surface reduction of ceria and bulk reduction of ceria, respectively [26].

For 1 % Pd/CeO_2, a positive peak with a shoulder was observed at nearly 35 °C which attributes to the reduction of precious metal (PdO to Pd) [35]. This shoulder peak corresponds to the presence of more than one different species or interactions. Moreover, the negative peak was observed at around 70 °C attributing to the decomposition of β-hydride palladium phase [77]. Surface and bulk reduction peaks of ceria were also detected in the temperature range of 300-500 °C and 600-900 °C, respectively.

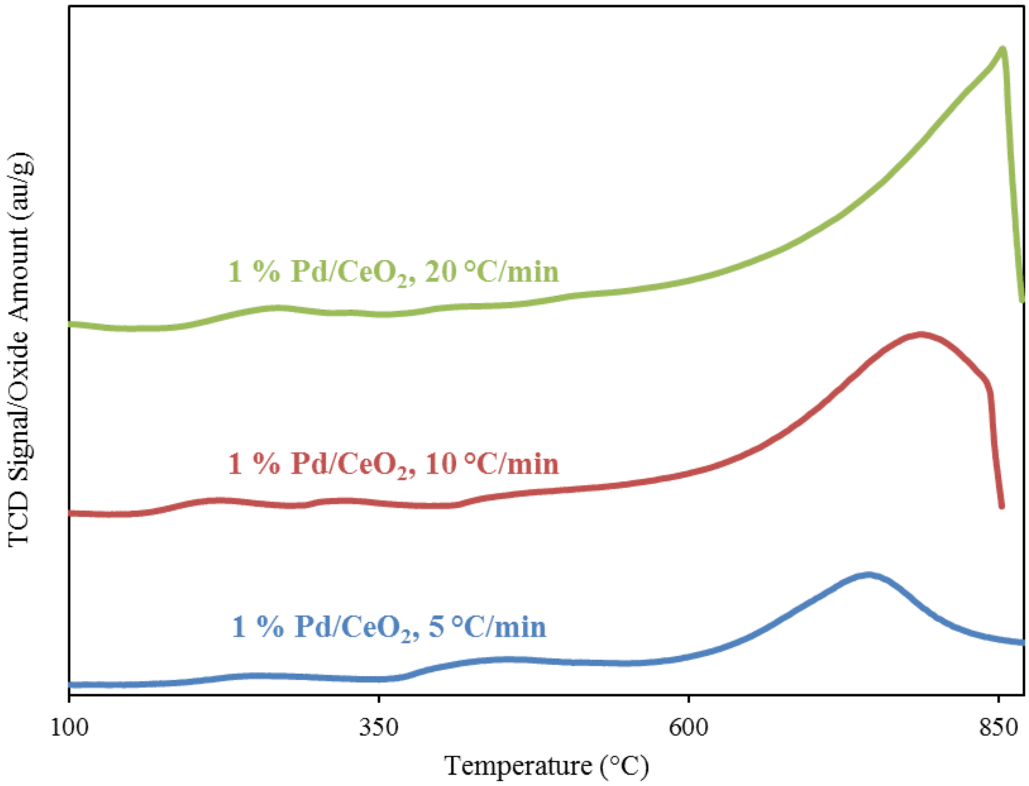

Figure 4.4 TPR pattern of 1 % Pd/CeO_2 at 5, 10 and 20 °C/min heating rates under 25 sccm 10 % H_2-Ar flow

In Figure 4.4, TPR pattern for 1 % Pd/CeO_2 at different heating rates is given. It is clearly seen that lower heating rates provide enough time to complete the reduction process. Moreover, it is observed that decreasing heating rate results in a shift in reduction temperature and a decrease in reduction area. Additional research is required to understand the reason for this phenomenon.

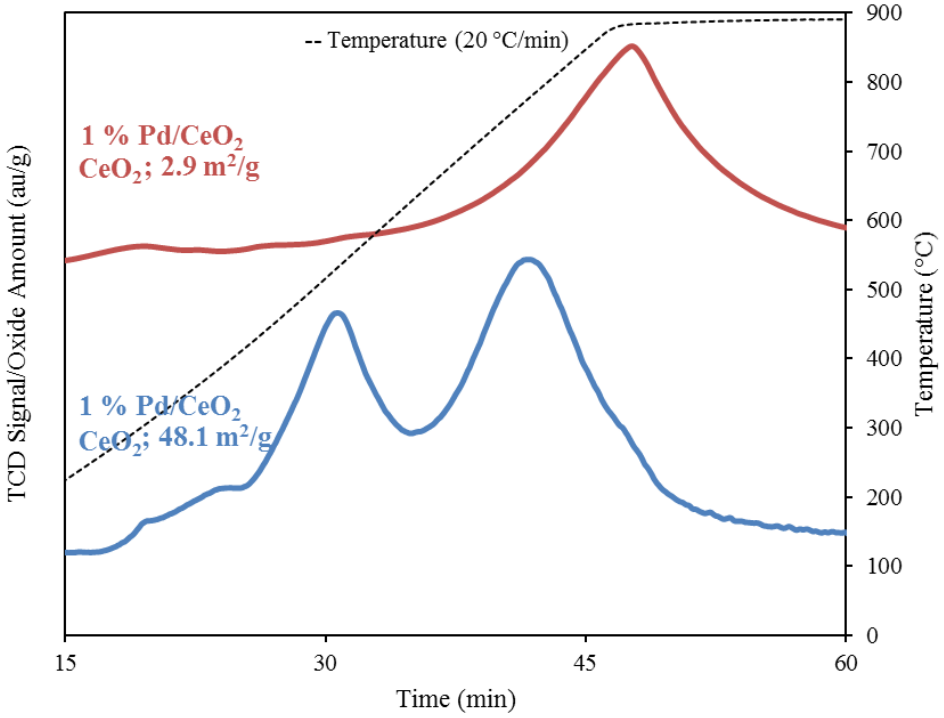

Figure 4.5 TPR pattern of 1 % Pd/CeO$_2$ with CeO$_2$ surface areas 2.9 m^2/g and 48.1 m^2/g at 20 °C/min heating rate under 25 sccm 10 % H$_2$-Ar flow

1 % Pd/CeO$_2$ synthesized with average particle size of 25 nm ceria was also provided from Ozkar Group [78]. TPR was performed for Pd-nanoceria oxide and results are given in Figure 4.5. Surface area of ceria strongly affects the hydrogen uptake capacity and surface reduction peak of ceria was observed more explicitly for 1 % Pd/CeO$_2$ oxides when the surface area of ceria is higher [27].

TPR pattern for CeO_2, 1 % Pd/CeO_2, 1 % Pd/CeO_2-Al_2O_3 oxides, CeO_2-Al_2O_3, 1 % Pd/Al_2O_3 and γ-Al_2O_3 is given in Figure 4.6 below.

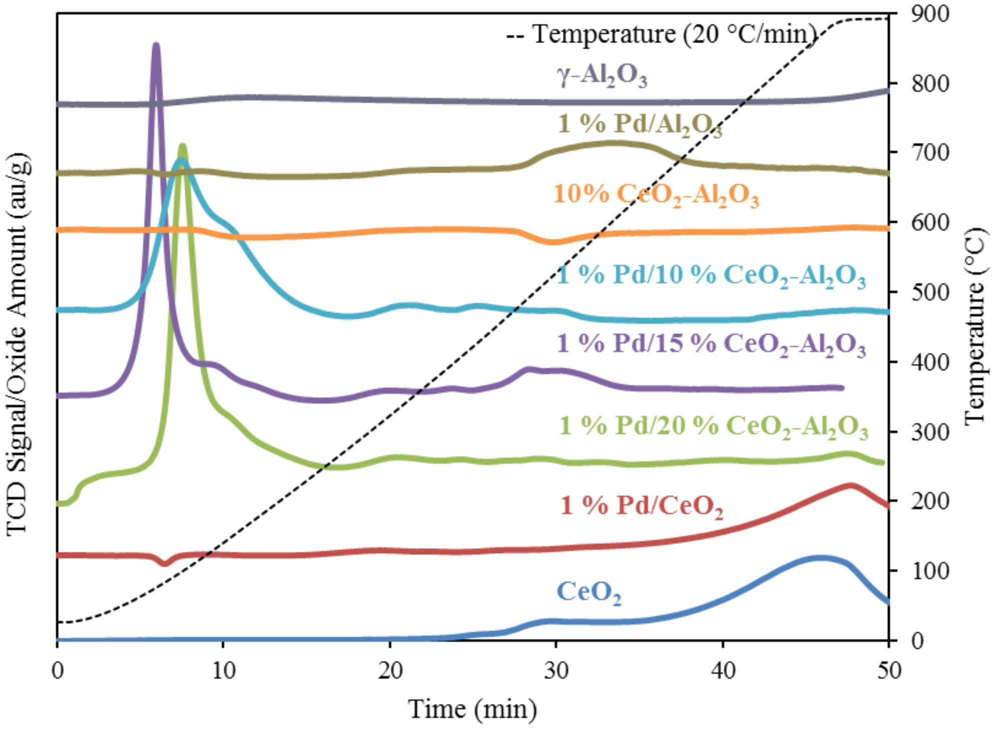

Figure 4.6 TPR pattern of CeO_2, 1 % Pd/CeO_2, 1 % Pd/CeO_2-Al_2O_3 oxides, CeO_2-Al_2O_3, 1 % Pd/Al_2O_3 and γ-Al_2O_3 at 20 °C/min heating rate under 25 sccm 10 % H_2-Ar flow

For γ-Al_2O_3, no obvious reduction peak was observed which is expected that alumina has no oxygen exchange mechanism.

For 1 % Pd/Al_2O_3, two very small peaks were observed. A negative peak at around 80 °C attributes to the decomposition of β-hydride palladium phase [77]. Up to 450 °C, no reduction peak was detected which means that no oxidized Pd particles are reduced in this temperature range. A small, positive peak in the temperature range of 450-650 °C was observed and it corresponds to the reduction of adsorbed oxygen on alumina.

For 10 % CeO_2-Al_2O_3, no obvious reduction peak was detected mainly due to the low percentage of ceria.

For, 1 % Pd/CeO_2-Al_2O_3 oxides, in the low temperature region between 25 °C and 200 °C, a high intensity peak with a shoulder was observed. Trovarelli et al. reported that this peak attributes to the reduction of PdO to Pd and high intensity indicates that hydrogen consumption is higher than the reduction of metal precursor. Hence, surface Ce^{+4} reduction occurs simultaneously at this temperature range [35]. Two maxima in this peak also confirm that the reduction of PdO to Pd and the reduction of CeO_2 to Ce_2O_3 happen in the temperature range of 25-200 °C. Additional reduction peaks were observed for all 1 % Pd/CeO_2-Al_2O_3 oxides in the temperature range 300-500 °C mainly because of reduction of oxygen adsorbed on alumina or reduction of $CeAlO_3$ species.

4.3.1.1. Hydrogen Uptake Amounts

In order to quantify hydrogen uptake amounts from TPR data, Ag_2O was used as a reference material. Ag_2O was reduced under the same conditions and it is calculated that 1 unit area corresponds to $7.30*10^{-5}$ mol or $1.46*10^{-4}$ g H_2 amount. Calculations related to the TPR of Ag_2O are given in Appendix C.1.1.

The reactions for reduction of ceria and palladium oxide are given in Equation 4.1 and Equation 4.2 below. It is seen that for 2 moles of CeO_2 and 1 mol of Pd, 1 mol of H_2 is consumed during TPR.

$$2CeO_2 + H_2 \rightarrow Ce_2O_3 + H_2O \qquad \text{Equation 4.1}$$

$$PdO + H_2 \rightarrow Pd + H_2O \qquad \text{Equation 4.2}$$

For CeO_2, hydrogen consumption was calculated for each peak present in TPR data and it is given in Table 4.2 below. Stoichiometric hydrogen consumption was calculated for CeO_2 and results are given in Table C.2 in Appendix C.1.2.

Table 4.2 Hydrogen consumption for CeO_2 during TPR

	Temperature range	**Temperature (°C)**	**Calculated area**	**Hydrogen consumption (mol)**
1st Peak	300-400 °C	364.2	0.019	$1.43*10^{-6}$
2nd Peak	450-800 °C	675.4	0.344	$2.51*10^{-5}$
		838.9	0.082	$5.98*10^{-6}$

For CeO_2, hydrogen consumption amount during TPR was compared with the theoretically calculated amount and it is seen that 44.8 % of CeO_2 was reduced during TPR analysis.

For 1 % Pd/CeO_2, hydrogen consumption was calculated for each peak present in TPR data and it is given in Table 4.3 below. Additionally, theoretical hydrogen consumption was calculated for both PdO and CeO_2 in 1 % Pd/CeO_2 and results are given in Table C.3 in Appendix C.1.3.

Table 4.3 Hydrogen consumption for 1 % Pd/CeO_2 during TPR

	Temperature range	**Temperature (°C)**	**Calculated area**	**Hydrogen consumption (mol)**
1st Peak	25-60 °C	28.1	0.092	$6.70*10^{-6}$
		35.4	0.048	$3.48*10^{-6}$
2nd Peak	60-85 °C	73.9	-0.011	$-7.79*10^{-7}$
3rd Peak	200-300 °C	254.7	0.036	$2.61*10^{-6}$
4th Peak	300-500 °C	442.1	0.072	$5.25*10^{-6}$
5th Peak	600-900 °C	741.1	0.696	$7.13*10^{-5}$
		879.9	0.097	$7.11*10^{-6}$

For 1 % Pd/CeO_2, to validate TPR peaks, hydrogen consumption amount during TPR was compared with the theoretically calculated amount. It is reported in the literature that the first peak in the temperature range of 25-60 °C attributes to the reduction of PdO [35]. Since there is a shoulder peak in this temperature range, it is assumed that more than one species were reduced. Consumed hydrogen peak calculation confirms that at 28.1 °C, $6.70*10^{-6}$ mol hydrogen was consumed which is almost equal to the hydrogen consumption by PdO calculated using stoichiometry. Moreover, the molar ratio of consumed H_2 at 28.1 °C to Pd in oxide was calculated as 1.17 and it also approves that the main state of palladium on ceria surface is PdO. Therefore, it can be concluded that all PdO was reduced to Pd at nearly 28.1 °C.

Ferrer et al. reported that the negative peak was observed around 70 °C which attributes to the decomposition of β-hydride palladium phase [77]. Since this hydride peak observed, the temperatures between 25-60 °C, some of the reduced Pd formed β-PdH_x phase. Calculating the second peak area, it can be concluded that $7.79*10^{-7}$ mol hydrogen was consumed in first peak to form PdH_x at nearly 28.1 °C.

Experimental results revealed that there is more hydrogen consumed during first peak which can be attributed to the reduction of CeO_2 species. Stoichiometric calculations confirm that 2.1 % of CeO_2 was reduced at nearly 35.4 °C. The reason of low temperature reduction of ceria can be explained via the spillover of hydrogen in the presence of Pd atoms. Moreover, percentage CeO_2 surface atoms were calculated using surface area data and the results are given in Table C.6 in Appendix C.3. It is calculated that approximately 0.83 % CeO_2 atoms are on the surface of 1 % Pd/CeO_2 oxide. Therefore, at nearly 35.4 °C, all surface CeO_2 atoms were reduced in the presence of Pd.

For the reduction of remained CeO_2, consumed hydrogen for other peaks was calculated. Hence, in the temperatures between 200-300 °C, 300-500 °C and 600-900 °C, 1.5 %, 2.9 % and 44.8 % of bulk CeO_2 was reduced, respectively. Totally, 51.3 % of CeO_2 was reduced during TPR analysis.

For 1 % Pd/CeO_2-Al_2O_3 oxides, hydrogen consumption was calculated for first peak present in TPR data and it is given in Table 4.4 below. Additionally, theoretical hydrogen consumption was calculated for both PdO and CeO_2 in 1 % Pd/CeO_2 and results are given in Table C.4 in Appendix C.1.4.

Table 4.4 Hydrogen consumption for 1 % Pd/CeO_2-Al_2O_3 oxides during TPR in the temperature range of 25-200 °C

	Temperature (°C)	**Calculated area**	**Hydrogen consumption (mol)**
1 % Pd/20 % CeO_2-Al_2O_3	73.3	0.376	$2.75*10^{-5}$
	101.0	0.092	$6.69*10^{-6}$
1 % Pd/15 % CeO_2-Al_2O_3	73.7	0.259	$1.89*10^{-5}$
	110.5	0.042	$8.04*10^{-6}$
1 % Pd/10 % CeO_2-Al_2O_3	75.2	0.157	$1.15*10^{-5}$
	113.1	0.090	$6.58*10^{-6}$

For 1 % Pd/CeO_2-Al_2O_3 oxides, hydrogen consumption amount during TPR at temperatures between 25-200 °C was compared with the theoretically calculated amount. It is clearly seen that hydrogen consumption calculated from TPR data is higher than hydrogen consumption of PdO calculated theoretically for all oxides. Therefore, it can be concluded that in addition to the reduction of PdO, more hydrogen was consumed by CeO_2 at nearly 80 °C for all oxides. This phenomenon can be explained by the reduction of CeO_2 via spillover in the presence of Pd atoms. Moreover, hydrogen consumption calculations show that CeO_2 was reduced totally to Ce_2O_3 for all oxides. In addition to the hydrogen consumed by PdO and CeO_2, more hydrogen was consumed by 1 % Pd/CeO_2-Al_2O_3 oxides at nearly 100 °C and this excess hydrogen consumption increases with the increase in alumina percentage. This situation can be explained by the reduction of adsorbed oxygen species of alumina or the formation of $CeAlO_3$ perovskite structure.

4.3.2. TPO Results

The oxygen uptake temperature and capacity of prepared oxides were investigated by TPO.

In Figure 4.7, TPO patterns after TPtD for 1 % Pd/CeO_2 at different heating rates are given.

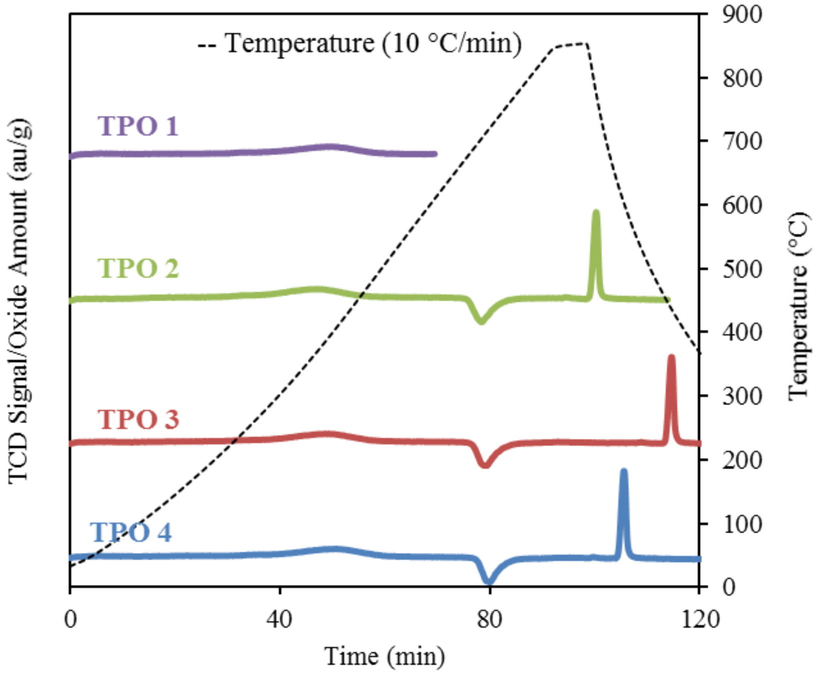

(a)

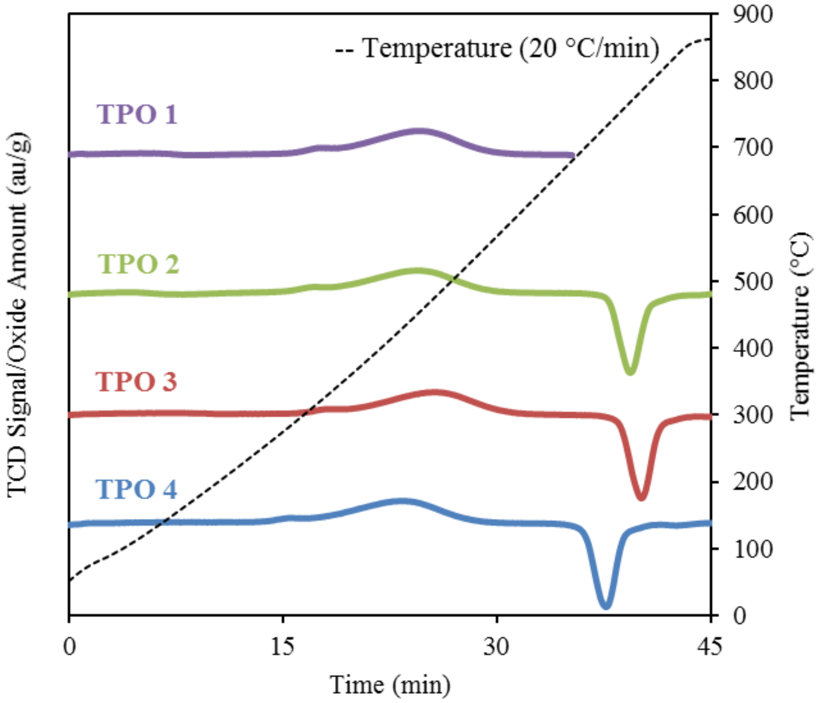

(b)

Figure 4.7 TPO pattern after TPtD of 1 % Pd/CeO_2 at (a) 10 °C/min and (b) 20 °C/min heating rates under 25 sccm 2 % O_2-He flow

For 1 % Pd/CeO_2, 4 cycles were performed to observe oxygen release and uptake behavior. TPO experiments were conducted up to 750 °C after first decomposition (TPO 1) and up to 950 °C after other decomposition steps (TPO 2, TPO 3, TPO 4). It is clearly seen that, 1 % Pd/CeO_2 can uptake oxygen after decomposition for 4 cycles in the temperature range 200-600 °C and peak temperature of nearly 400 °C. At higher temperatures; between 700-800 °C, a negative peak was observed which attributes to the decomposition of an oxide species. In other words, oxide released oxygen at that temperature in an O_2 atmosphere. Gil et al. reported that at nearly 750 °C, PdO decomposition was observed under an oxygen atmosphere [79]. Wang et al. reported that under CO atmosphere, both positive and negative peaks can be observed and the negative peak corresponds to the reduction of CeO_2 in the bulk facilitated by Pd [80].

Cooling stage was also recorded at 20 °C/min heating rate and it is seen that oxide uptakes oxygen during cooling at nearly 600 °C. These two step oxidation indicates that there are two different species decomposed.

In Figure 4.8, TPO pattern after TPtD for 1 % Pd/CeO_2 and 1 % Pd/CeO_2-Al_2O_3 oxides is given. It is seen that under oxygen atmosphere, oxygen uptake temperature decreased whereas oxygen release temperature increased by adding Al_2O_3 to the structure.

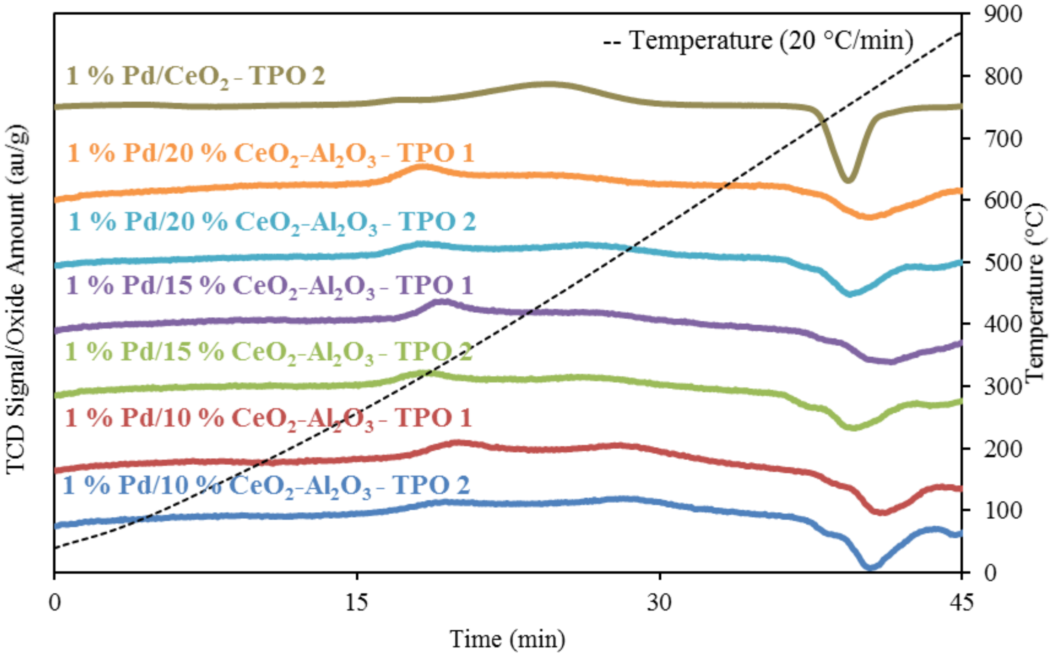

Figure 4.8 TPO pattern after TPtD of 1 % Pd/CeO_2 and 1 % Pd/CeO_2-Al_2O_3 oxides at 20 °C/min heating rate under 25 sccm 2 % O_2-He flow

4.3.3. TPtD Results

The oxygen release temperature and capacity of prepared oxides was investigated by TPtD.

Since it is known that pure CeO_2 decomposes at nearly 1600 °C under an inert atmosphere [8], TPO experiments after TPtD were not performed for CeO_2. Also, Al_2O_3 cannot decompose at recorded temperatures therefore, no TPO experiments after TPtD were conducted for Al_2O_3.

In Figure 4.9, TPtD patterns after TPO for 1 % Pd/CeO_2 at different heating rates are given.

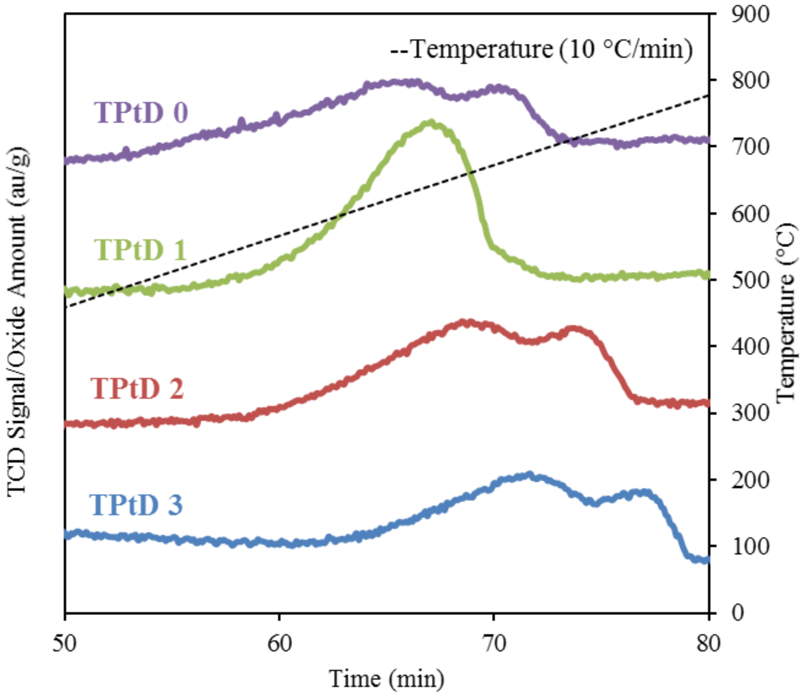

(a)

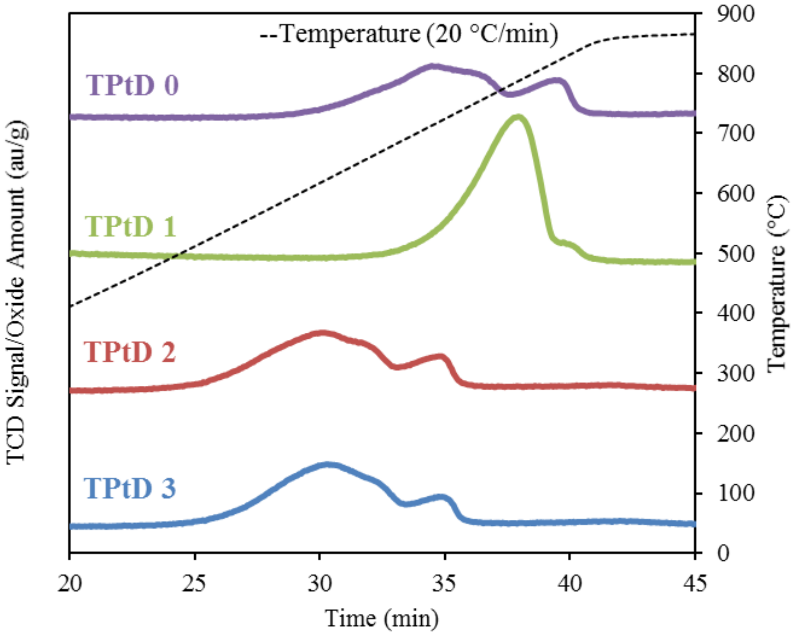

(b)

Figure 4.9 TPtD pattern after TPO of 1 % Pd/CeO_2 at (a) 10 °C/min and (b) 20 °C/min heating rates under 25 sccm He flow

For 1 % Pd/CeO_2, it is seen that by adding Pd, decomposition temperature of CeO_2 was lowered by nearly 940 °C which is also a proof for Pd-Ceria interaction. Lower temperature decomposition can be explained by the reverse spillover of oxygen species in ceria in the presence of Pd. Moreover, during oxidation step, if temperature increases up to 950 °C, the decomposition amount is lower (TPtD 0, TPtD 2, TPtD 3) because of the fact that decomposition of oxide already starts during TPO.

In Figure 4.10, TPtD pattern after TPO for 1 % Pd/CeO_2 and 1 % Pd/CeO_2-Al_2O_3 oxides is given.

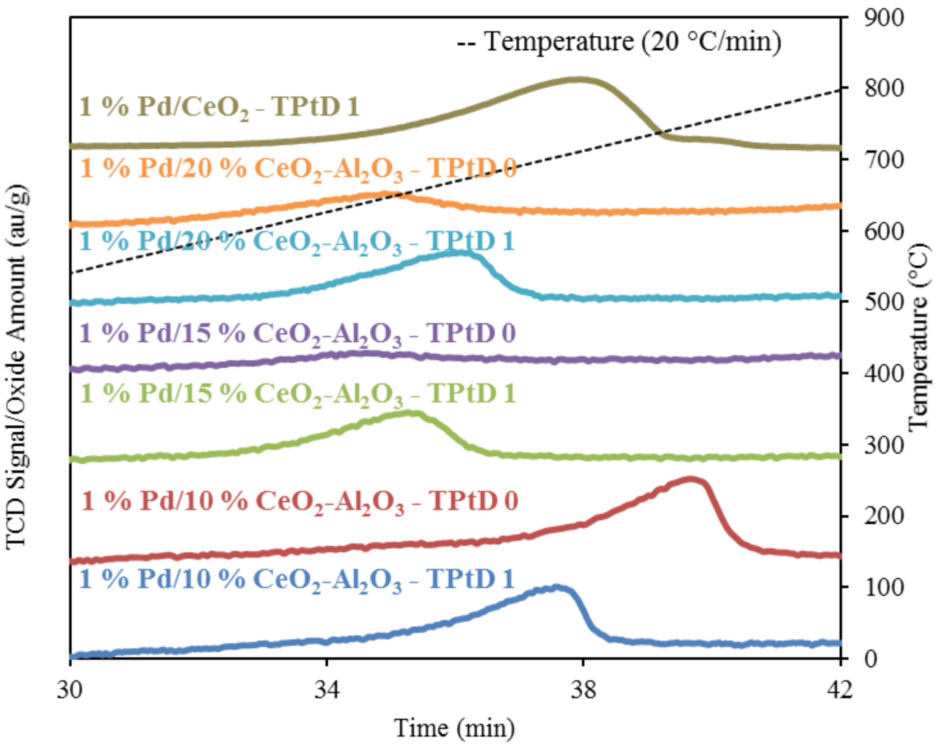

Figure 4.10 TPtD pattern after TPO of 1 % Pd/CeO_2 and 1 % Pd/CeO_2-Al_2O_3 oxides at 20 °C/min heating rate under 25 sccm He flow

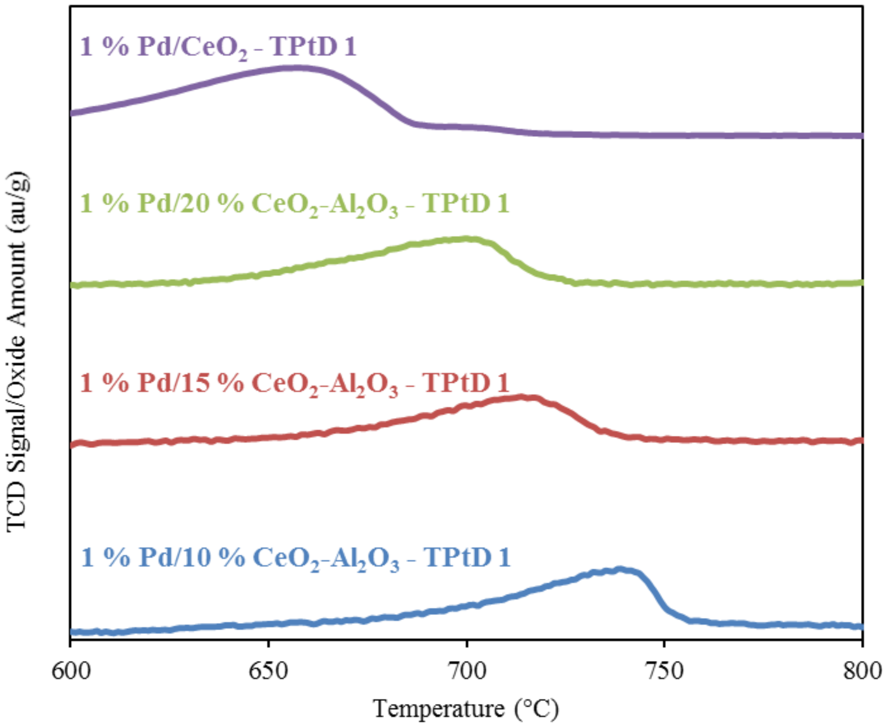

Figure 4.11 TPtD 1 pattern after TPO 1 of 1 % Pd/CeO_2 and 1 % Pd/CeO_2-Al_2O_3 oxides at 20 °C/min heating rate under 25 sccm He flow

From Figure 4.10, it is seen that adding Al_2O_3 causes thermal decomposition temperature increase by nearly 40 °C. Also, only 1st order decomposition kinetics observed for Al_2O_3 added oxides whereas for 1 % Pd/CeO_2, if temperature is increased up to 750 °C during TPO, 1st order decomposition kinetics observed. Otherwise, a shoulder peak observed during decomposition. Moreover, from Figure 4.11, it is seen that increasing ceria amount lowers the decomposition temperature.

4.3.3.1. Oxygen Uptake and Release Amounts

The area under TPO and TPtD curves were calculated for prepared oxides by using Matlab Interactive Peak Fitter tool. In order to quantify oxygen uptake and release amounts in terms of mol or gram O_2 per oxide, air injection calibration was performed and the related data is given in Appendix C.2.

In Table 4.5, oxygen uptake and release amount for 1 % Pd/CeO_2 are given.

Table 4.5 Oxygen uptake and release amounts for 1 % Pd/CeO_2 during two-step thermochemical cycles at 10 °C/min heating rate

Cycle	**Total oxygen release (mol O_2)**	**Total oxygen uptake (mol O_2)**	**Cumulative total oxygen release (mol O_2)**	**Cumulative total oxygen uptake (mol O_2)**
1st cycle	$5.20*10^{-7}$	$7.85*10^{-7}$	$5.20*10^{-7}$	$7.85*10^{-7}$
2nd cycle	$9.78*10^{-7}$	$1.52*10^{-6}$	$1.50*10^{-6}$	$2.30*10^{-6}$
3rd cycle	$1.09*10^{-6}$	$1.40*10^{-6}$	$2.58*10^{-6}$	$3.70*10^{-6}$
4th cycle	$1.05*10^{-6}$	$1.40*10^{-6}$	$3.64*10^{-6}$	$5.10*10^{-6}$

It is seen that oxygen release and uptake amounts increase during first 3 cycles and become nearly constant after 3rd cycle. Moreover, oxidation amount is higher than decomposition amount for all cycles. In other words, oxygen content of oxide tends to remain high and quasi-equilibrium oxidation state is observed for 1 % Pd/CeO_2 oxide [14].

In Table 4.6, oxygen uptake and release amount for 1 % Pd/CeO_2-Al_2O_3 oxides are given.

Table 4.6 Oxygen uptake and release amounts for 1 % Pd/CeO_2-Al_2O_3 oxides during two-step thermochemical cycles at 20 °C/min heating rate

Oxide	**Total oxygen release/ CeO_2 amount (g/g)**		**Total oxygen uptake / CeO_2 amount (g/g)**	
	1st Cycle	**2nd Cycle**	**1st Cycle**	**2nd Cycle**
1 % Pd/20 % CeO_2-Al_2O_3	$1.19*10^{-3}$	$1.42*10^{-3}$	$3.01*10^{-4}$	$1.14*10^{-3}$
1 % Pd/15 % CeO_2-Al_2O_3	$2.31*10^{-3}$	$2.45*10^{-3}$	$3.38*10^{-4}$	$8.57*10^{-4}$
1 % Pd/10 % CeO_2-Al_2O_3	$5.21*10^{-3}$	$4.85*10^{-3}$	$6.99*10^{-4}$	$4.71*10^{-4}$

It is clearly seen that increasing alumina amount in prepared oxides results in increasing oxygen release amount per ceria basis. The reason is that when there is enough alumina surface for ceria coverage, the amount of use of ceria surface atoms will be higher.

4.3.4. Activation Energy Calculations for TPx Experiments

4.3.4.1. Redhead Method

For this method, TPtD reaction is assumed to be first-order and Equation 3.5 was used to calculate activation energy for a given pre-exponential factor, heating rate and peak temperature. Detailed sample calculation for activation energies is given in Appendix C.4.1.

In Table 4.7, calculated activation energies for TPtD experiments by Redhead method are tabulated.

Table 4.7 Calculated activation energies for TPtD experiments by Redhead method

Oxide	Experiment	Maximum rate temperature (°C)	Ea* (kJ/mol)
1 % Pd/CeO_2	TPtD 1	661.8	167.1
1 % Pd/20 % CeO_2-Al_2O_3	TPtD 0	682.1	170.9
	TPtD 1	704.4	175.1
1 % Pd/15 % CeO_2-Al_2O_3	TPtD 0	693.2	173.0
	TPtD 1	716.9	177.4
1 % Pd/10 % CeO_2-Al_2O_3	TPtD 0	745.0	182.7
	TPtD 1	736.3	181.0

*The pre-exponential factor was assumed as 10^9 min^{-1} [74].

It is seen that adding Al_2O_3 to the structure causes higher activation energies and different ceria loadings has a very small effects on activation energy for decomposition reaction.

4.3.4.2. Differential Method

For differential method, In(TCD signal) vs. 1/T was plotted. The slope and the intercept of this plot gives $-E_a/R$ and $In(k_0)$, respectively.

In Table 4.8, calculated activation energies and pre-exponential factors for TPtD experiments by differential method are tabulated.

Table 4.8 Calculated activation energies and pre-exponential factors for prepared oxides during TPtD experiments by using differential method

Oxide	**Experiment**	**Ea (kJ/mol)**	**Pre-exponential factor**
1 % Pd/CeO_2	TPtD 0	106.1	$8.98*10^3$
	TPtD 1	381.3	$5.31*10^{20}$
	TPtD 2	161.4	$2.81*10^7$
	TPtD 3	166.4	$6.16*10^7$
1 % Pd/20 % CeO_2-Al_2O_3	TPtD 0	226.3	$1.30*10^9$
	TPtD 1	198.2	$8.10*10^9$
1 % Pd/15 % CeO_2-Al_2O_3	TPtD 0	120.1	$2.29*10^3$
	TPtD 1	196.2	$4.10*10^7$
1 % Pd/10 % CeO_2-Al_2O_3	TPtD 0	83.1	$5.47*10^1$
	TPtD 1	174.1	$2.14*10^6$

Differential analysis provides reliable results for activation energy calculation at low conversion levels. From Table 4.8, it is seen that generally, calculated activation energies are similar with the ones calculated from Redhead method. However, for 1 % Pd/CeO_2, if decomposition starts during TPO (TPtD 0, TPtD 2, TPtD 3), activation energy is about 2 times lower. Additionally, as calculated in Redhead method, addition of alumina makes activation energies of decomposition reaction higher.

Uner et al. reported that pre-exponential factor gives additional information about sticking coefficient, changes due to reaction and the number and geometry of the surface sites [36]. In the light of this information, it can be concluded that 1 %

Pd/20 % CeO_2-Al_2O_3 had the highest active sites among the other prepared oxides. Moreover, for 1 % Pd/CeO_2, TPtD 1 gives the highest pre-exponential factor. It is also expected due to the fact that for other TPtD experiments (TPtD 0, TPtD 2, TPtD 3), some active sites for oxygen release are observed during TPO.

4.3.4.3. Kissinger Method

For Kissinger method, activation energies and pre-exponential factors were calculated using different heating rates for 1st order reaction kinetics.

In Table 4.9, calculated activation energies and pre-exponential factors for TPR experiments by Kissinger method are tabulated.

Table 4.9 Calculated activation energies and pre-exponential factors for CeO_2 and 1 % Pd/CeO_2 during TPR experiments by using Kissinger method

Oxide	**Ea (kJ/mol)**	**Pre-exponential factor**
CeO_2	66.5	$1.10*10^{-1}$
1 % Pd/CeO_2	106.5	$1.89*10^{1}$

Activation energies of TPR experiments for CeO_2 and 1 % Pd/CeO_2 were calculated for the highest temperature peak which corresponds to the bulk reduction peak of ceria. While stoichiometric calculations reveal that more CeO_2 was reduced in the presence of Pd, activation energy for the reduction of oxygen species in bulk CeO_2 in the presence of Pd is higher. It can be concluded that Pd facilitates the reduction of surface species rather than bulk species. Moreover, it is reported that activation energy is lowered by half for the reactions with no heat effect [81]. It can be concluded that for 1 % Pd/CeO_2, the reduction process is in the kinetic regime, however, for CeO_2, the reduction process is in the pore diffusion regime and mass transfer limited.

4.4. Chemisorption Results

In order to investigate H_2 adsorption capacity, volumetric adsorption measurement was performed for 1 % Pd/CeO_2 by using chemisorption manifold.

In Figure 4.12, hydrogen adsorption amount is given for 1 % Pd/CeO_2.

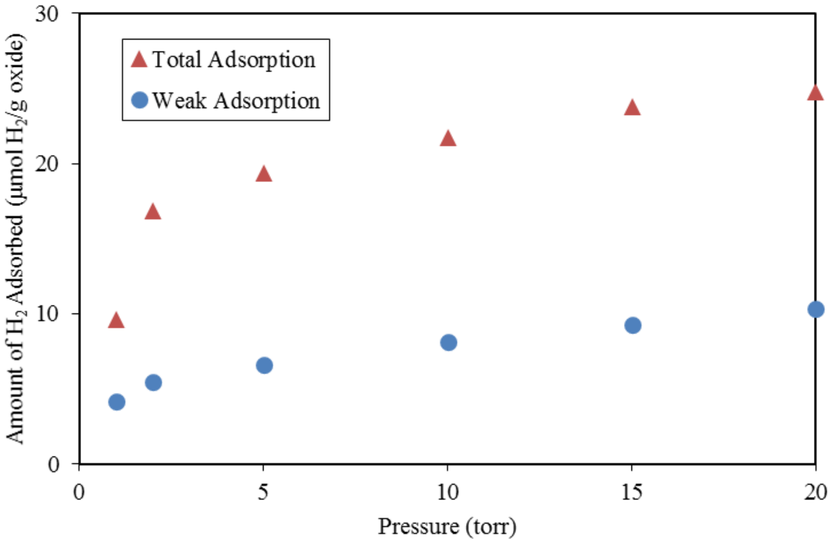

Figure 4.12 Percentage dispersion measurements for 1 % Pd/CeO_2 at 30 °C

From Figure 4.12, total, weak and strong adsorption amounts were calculated as 13.6, 4.6 and 9.0 μmol H_2/g oxide, respectively. Therefore, dispersion was calculated from strong adsorption data as 19.2 %. Mean particle diameter can be calculated from dispersion data. For 19.2 % dispersion, mean particle diameter are found as 5.21 nm. Sample calculation for dispersion and mean particle diameter is given in Appendix C.5.

4.5. Microcalorimetry Results

In order to investigate H_2, O_2 and H_2O adsorption capacity and heat of adsorption, adsorption measurements were performed on of 1 % Pd/CeO_2 and 1 % Pd/CeO_2-Al_2O_3 oxides by using microcalorimetry.

4.5.1. H_2 Adsorption

In Figure 4.13 and Figure 4.14, heat of H_2 adsorptions and H_2 adsorption amounts are given for 1 % Pd/CeO_2 and 1 % Pd/CeO_2-Al_2O_3 oxides.

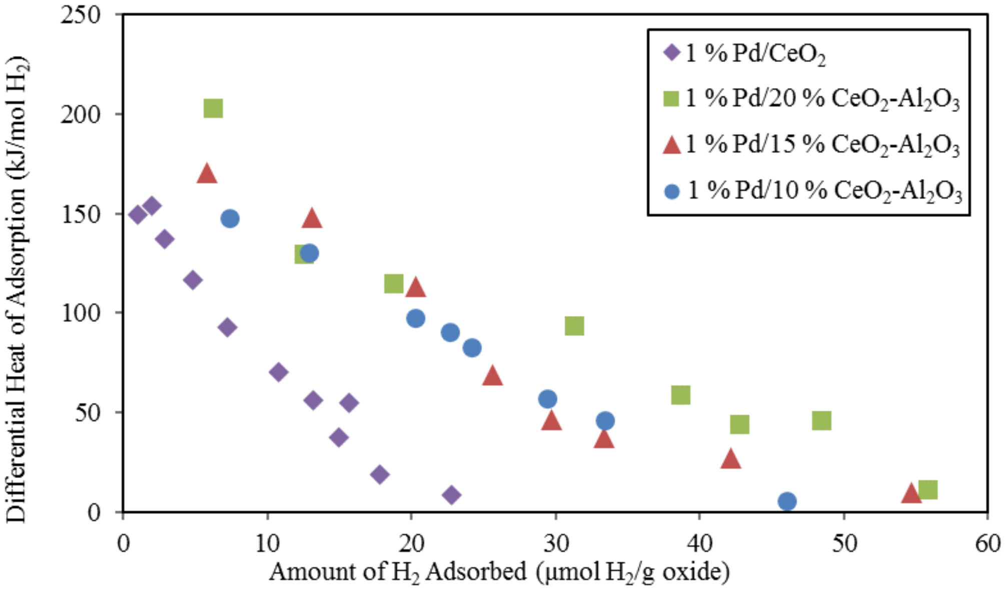

(a)

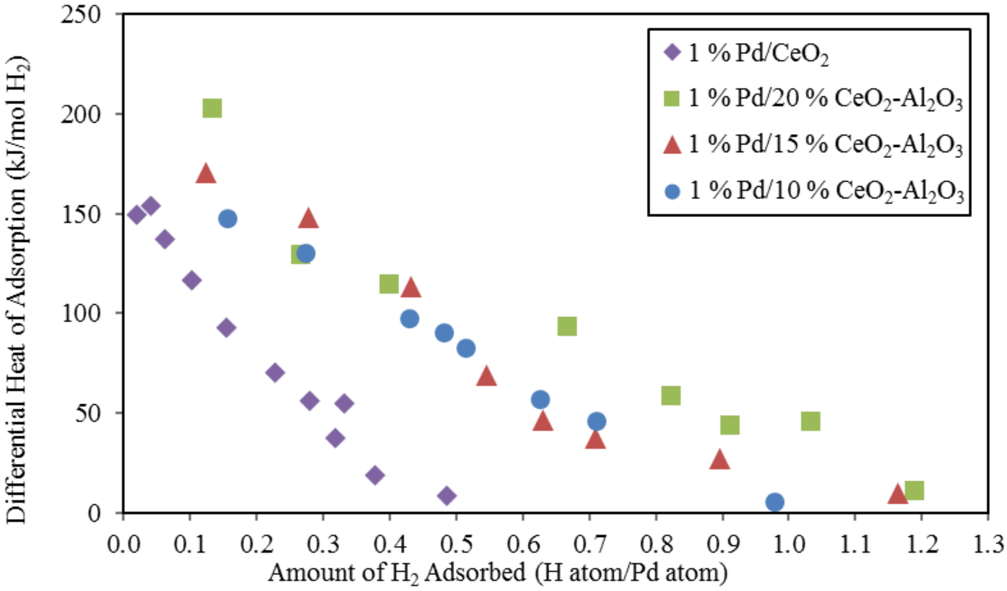

(b)

Figure 4.13 Differential heats of H_2 adsorption on 1 % Pd/CeO_2 (at 100 °C) and 1 % Pd/CeO_2-Al_2O_3 oxides (at 50 °C) (a) μmol H_2/g oxide vs differential heat of adsorption (b) H atom/Pd atom vs differential heat of adsorption

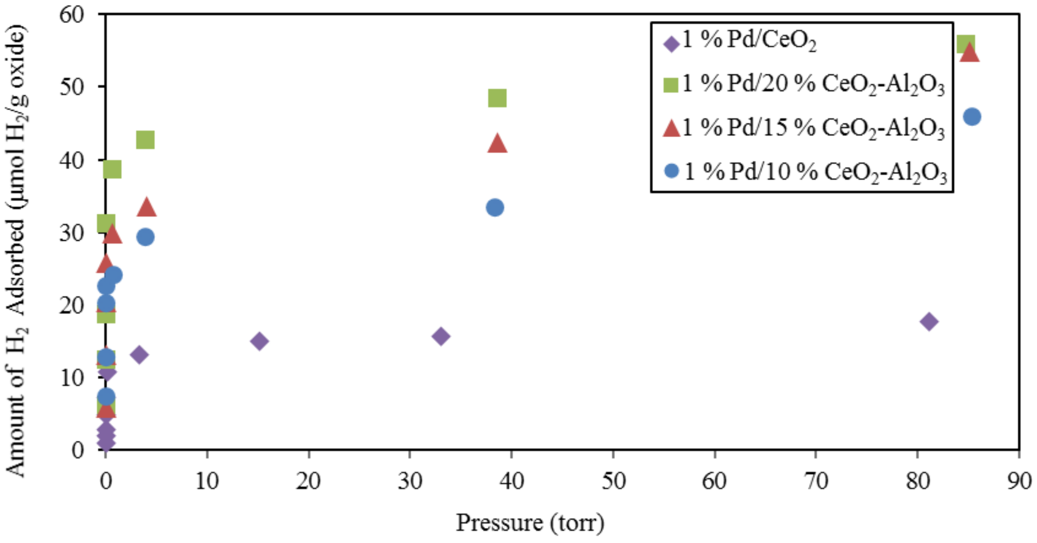

Figure 4.14 H_2 adsorption isotherms for 1 % Pd/CeO_2 (at 100 °C) and 1 % Pd/CeO_2-Al_2O_3 oxides (at 50 °C)

There is no observable change in heat of H_2 adsorption data at initial coverage for all synthesized oxides. However, it is seen that H_2 adsorption capacity increases with the addition of Al_2O_3 to the structure. Moreover, increase in CeO_2 amount in 1 % Pd/CeO_2-Al_2O_3 oxides results in slightly increase in H_2 adsorption capacity.

For all prepared oxides, H_2 adsorption decreases with coverage. Therefore, the sites that H_2 adsorbed to 1 % Pd/CeO_2 and 1 % Pd/CeO_2-Al_2O_3 oxides are consumed. It is seen that for 1 % Pd/CeO_2, the loss of H_2 adsorption sites were observed more quickly than 1 % Pd/CeO_2-Al_2O_3 oxides. Therefore, adding alumina to the structure increases the H_2 adsorption sites. Moreover, the ratio of H atom in the adsorbed gas to Pd atom in the oxide is higher than 1 for 1 % Pd/CeO_2-Al_2O_3 oxides. This also proves that more H is adsorbed onto oxide than Pd particles. Since there is no PdH_x peaks observed in TPR for 1 % Pd/CeO_2-Al_2O_3 oxides, this situation can be explained by spillover.

In Table 4.10, Pd dispersion for 1 % Pd/CeO_2 and 1 % Pd/CeO_2-Al_2O_3 oxides are tabulated. It is seen that addition of Al_2O_3 resulted in higher Pd dispersions.

Among 1 % Pd/CeO_2-Al_2O_3 oxides, highest ceria containing oxide has the highest Pd dispersion. This can be considered as a proof that ceria can stabilize Pd particles in the presence of alumina.

Table 4.10 Percentage Pd dispersions for synthesized oxides

Oxide	**BET surface area (m^2/g)**	**Amount of oxide for TPx experiments (g)**	**Pd dispersion (%)**	**Mean particle diameter (nm)**
1 % Pd/CeO_2	3.8	0.200	22.9	4.37
1 % Pd/20 % CeO_2-Al_2O_3	56.1	0.042	66.8	1.50
1 % Pd/15 % CeO_2-Al_2O_3	55.6	0.036	54.7	1.83
1 % Pd/10 % CeO_2-Al_2O_3	60.4	0.037	48.4	2.06

4.5.2. O_2 Adsorption

In Figure 4.15 and Figure 4.16, heat of O_2 adsorptions and O_2 adsorption amounts are given for 1 % Pd/CeO_2 and 1 % Pd/CeO_2-Al_2O_3 oxides.

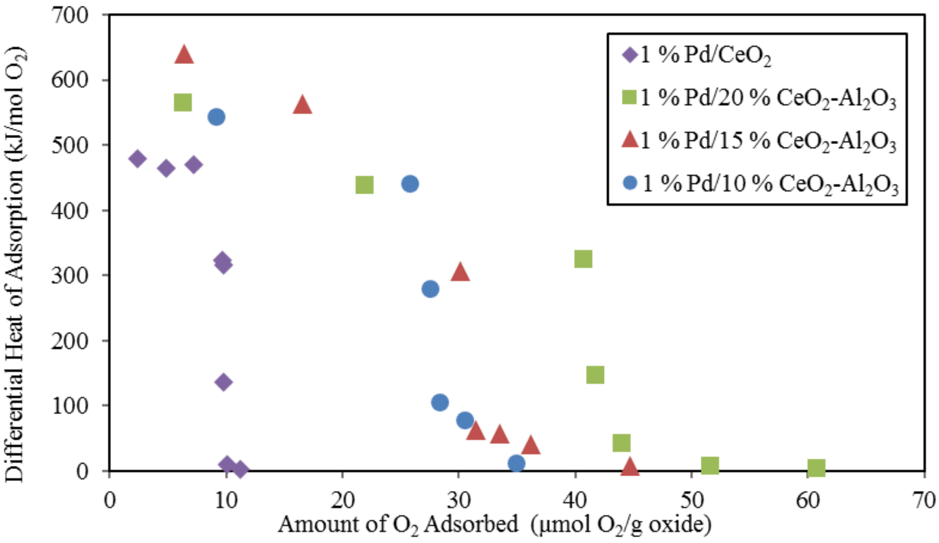

Figure 4.15 Differential heats of O_2 adsorption on 1 % Pd/CeO_2 (at 100 °C) and 1 % Pd/CeO_2-Al_2O_3 oxides (at 50 °C)

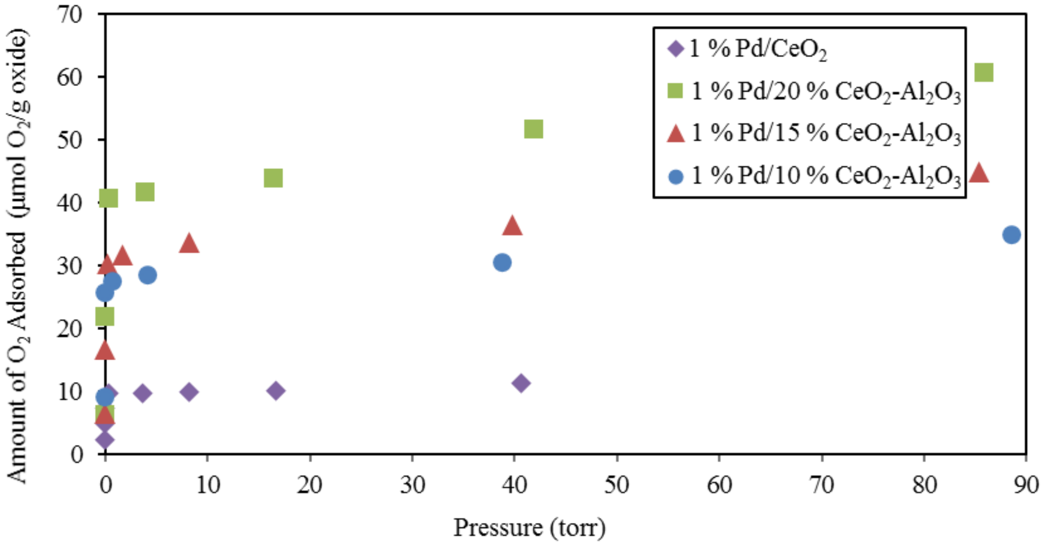

Figure 4.16 O_2 adsorption isotherms for 1 % Pd/CeO_2 (at 100 °C) and 1 % Pd/CeO_2-Al_2O_3 oxides (at 50 °C)

There is no observable change in heat of O_2 adsorption data at initial coverage for all synthesized oxides, very similar to the H_2 adsorption. Additionally, a similar trend with H_2 adsorption is seen in O_2 adsorption for all synthesized oxides.

The situation is similar with the H_2 adsorption that oxygen adsorption decreases with coverage and adding alumina to the structure increases the O_2 adsorption sites.

4.5.3. H_2O Adsorption

In Figure 4.17 and Figure 4.18, heat of H_2O adsorptions and H_2O adsorption amounts are given for 1 % Pd/CeO_2 and 1 % Pd/CeO_2-Al_2O_3 oxides.

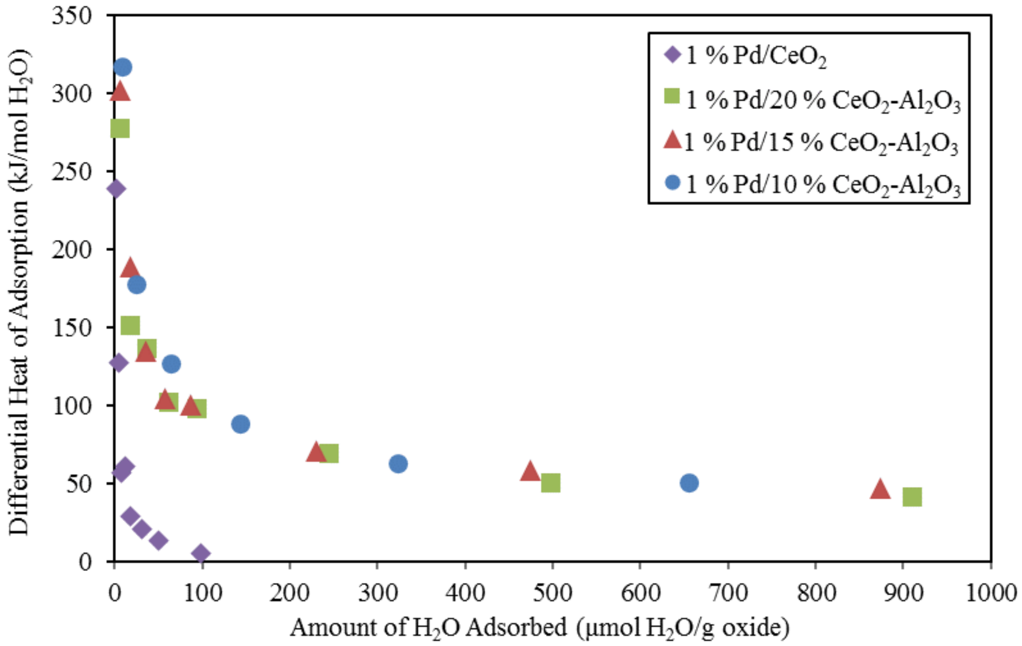

Figure 4.17 Differential heats of H_2O adsorption on 1 % Pd/CeO_2 (at 100 °C) and 1 % Pd/CeO_2-Al_2O_3 oxides (at 50 °C)

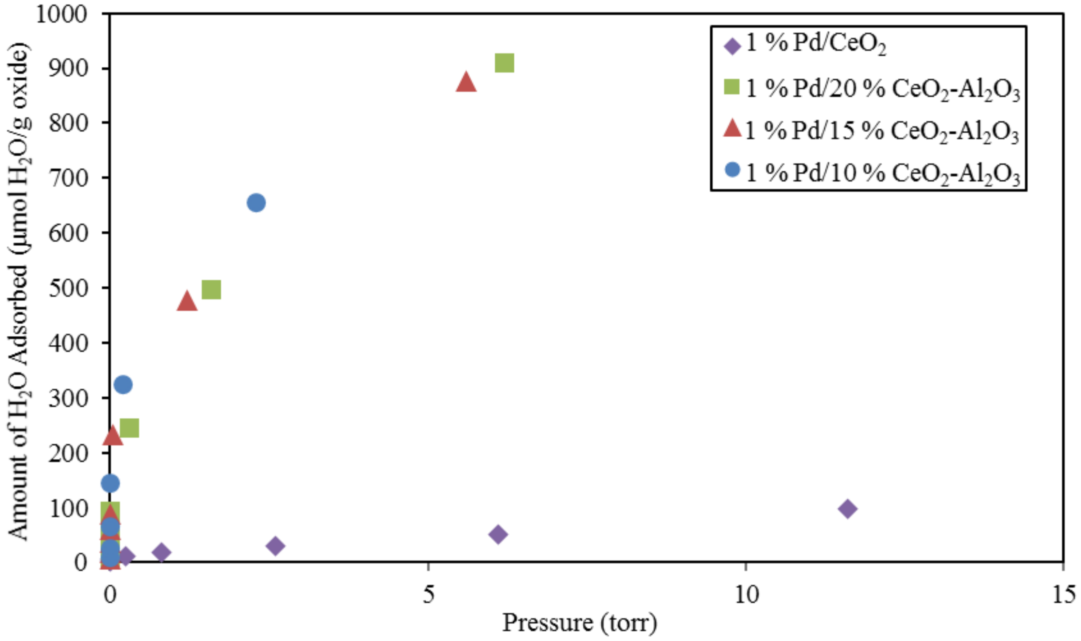

Figure 4.18 H_2O adsorption isotherms for 1 % Pd/CeO_2 (at 100 °C) and 1 % Pd/CeO_2-Al_2O_3 oxides (at 50 °C)

There is no observable change in heat of H_2O adsorption data at initial coverage for all synthesized oxides, very similar to the H_2 and O_2 adsorption. In Figure 4.18, it is seen that there is a huge increase in H_2O adsorption capacity with the addition of Al_2O_3 to the structure. However, unlike H_2 and O_2 adsorption, change in CeO_2 percentage in 1 % Pd/CeO_2-Al_2O_3 oxides has no effect on H_2O adsorption capacity. Moreover, adsorbed H_2O amount is about 10 times higher than H_2 and O_2 adsorption amount for all prepared oxides.

Similar to H_2 and O_2 adsorption, H_2O adsorption decreases with coverage and adding alumina to the structure increases the H_2O adsorption sites. However, there is difference for H_2O adsorption for all prepared oxides that there are intermediate and low adsorption sites are available for H_2O adsorption. Measurements show that there is a water adsorption site which energy state is nearly 240 kJ/mol after a surface coverage of 10 μmol H_2O/g oxide for 1 % Pd/CeO_2. For 1 % Pd/CeO_2-Al_2O_3 oxides, higher energy state adsorption site is observed nearly as 280-300 kJ/mol after a surface coverage of 50-60 μmol H_2O/g oxide.

4.5.4. Heat of Adsorption and Adsorption Amount Comparison

In Table 4.11, heat of adsorption data at initial coverage for 1 % Pd/CeO_2 and 1 % Pd/CeO_2-Al_2O_3 oxides are tabulated.

Table 4.11 Heat of adsorption data at initial coverage for 1 % Pd/CeO_2 and 1 % Pd/CeO_2-Al_2O_3 oxides

Oxide	**Heat of H_2 adsorption (kJ/mol)**	**Heat of O_2 adsorption (kJ/mol)**	**Heat of H_2O adsorption (kJ/mol)**
1 % Pd/CeO_2	149.7	478.5	239.3
1 % Pd/20 % CeO_2-Al_2O_3	202.9	564.8	277.7
1 % Pd/15 % CeO_2-Al_2O_3	167.0	639.1	301.6
1 % Pd/10 % CeO_2-Al_2O_3	147.8	543.2	316.6

It is known that O_2 and H_2 are stable molecules and dissociative adsorption of these gases are hard on most oxides. It is also known that precious metals have an ability to dissociate H_2 and O_2 atoms via spillover mechanism. Dissociative and molecular adsorption indicate different heat of adsorption data and for dissociative adsorption, heat of adsorption is generally 10 times higher than the one for molecular adsorption [82].

High heat of adsorption data indicate that dissociative adsorption occurs on all prepared oxides. Addition of Al_2O_3 to the structure results in higher H_2, O_2 and H_2O coverage. It is seen that heat of O_2 adsorption is almost two times higher than heat of H_2O adsorption for all prepared oxides mainly because of mole number of oxygen in gases. Therefore, it can be concluded that prepared oxides can be oxidized with water in addition to oxygen.

For H_2O, latent heat for condensation of water reported as 40 kJ/mol at nearly 330 K. Heat of adsorption results indicate that after monolayer adsorption complete, condensation occurs and water is adsorbed onto another molecule.

CHAPTER 5

CONCLUSIONS

Oxygen release/uptake kinetics of precious metal added ceria-containing oxides were studied by temperature programmed analyses and microcalorimetry. Incipient wetness method was used to synthesize 1 wt. % Pd/CeO_2 and 1 wt. % Pd/Al_2O_3 oxides and sequential impregnation method was used to synthesize 1 wt. % Pd/CeO_2-Al_2O_3 oxides with 20 wt. %, 15 wt. % and 10 wt. % loadings of ceria. Surface area of prepared oxides were measured with BET analysis and it is seen that surface area of 1 wt. % Pd/CeO_2 increases with the addition of Al_2O_3 to the structure. XRD analysis was performed for 1 wt. % Pd/CeO_2-Al_2O_3 oxides to investigate the crystal phases. For oxidized oxides, characteristic peaks of CeO_2 were observed while for reduced oxides, $CeAlO_3$ peaks were detected.

Temperature programmed analyses were performed to investigate the reducibility and oxygen release/uptake kinetics of prepared oxides. Temperature programmed reduction (TPR) analysis indicated that for 1 wt. % Pd/CeO_2, the peak at nearly 35 °C was observed which attributes to the reduction of precious metal. Stoichiometric calculations also confirmed that all PdO and all surface CeO_2 atoms (2.1 % of CeO_2) was reduced below 60 °C and 49.2 % of CeO_2 was reduced in the temperatures between 200-900 °C via the spillover of hydrogen in the presence of Pd. For 1 wt. % Pd/CeO_2-Al_2O_3 oxides, a high intensity peak in the temperature range of 25 °C-200 °C was observed and this peak attributes to the reduction of PdO to Pd in addition to the Ce^{+4} reduction. Stoichiometric calculations also confirmed that all PdO and all CeO_2 were reduced in this temperature range. Activation energy calculations by Kissinger method revealed that Pd facilitates the reduction of surface species rather than bulk species. Moreover, it can be concluded that for 1 % Pd/CeO_2, the reduction process is in the kinetic regime, however, for CeO_2, the reduction process is in the pore diffusion regime and mass transfer limited.

Temperature programmed oxidation (TPO) analysis showed that under oxidizing conditions, all prepared oxides both uptake and release oxygen under oxygen atmosphere. Temperature programmed thermal decomposition (TPtD) analysis showed that addition of Pd to CeO_2 decreases the thermal decomposition temperature by nearly 940 °C via the reverse spillover of oxygen atoms on ceria in the presence of Pd. TPtD experiments also confirm that oxides release oxygen during TPO. Area analysis showed that during 4th oxidation/decomposition cycle, 1 wt. % Pd/CeO_2 oxide releases $1.05*10^{-6}$ mol O_2 and uptakes $1.40*10^{-6}$ mol O_2, therefore it uptakes more oxygen than the amount it released. For 1 wt. % Pd/CeO_2-Al_2O_3 oxides, oxygen release amount per ceria basis increases with the increasing alumina amount in prepared oxides. TPtD activation energies were calculated for all prepared oxides by using Redhead and differential analysis. Activation energies calculated by Redhead analysis were very similar for all cycles and oxides as nearly 175 kJ/mol. Differential analysis results changed for different oxides and cycles.

Volumetric chemisorption measurements were performed for 1 wt. % Pd/$CeO_{2.}$ Strong hydrogen adsorption amount and dispersion were calculated as 9.0 μmol H_2/g oxide and 19.2 %, respectively.

Microcalorimetry measurements were performed to measure H_2, O_2 and H_2O vapor adsorption amount and heat of adsorption data for all prepared oxides. Measurements indicated that H_2, O_2 and H_2O adsorption capacity increases with the addition of alumina and heat of O_2 adsorption is almost two times higher than heat of H_2O adsorption for all prepared oxides which is a proof that all prepared oxides can be oxidized with both H_2O and O_2.

REFERENCES

[1] "EIA projects 48% increase in world energy consumption by 2040 - Today in Energy - U.S. Energy Information Administration (EIA)." [Online]. Available: http://www.eia.gov/todayinenergy/detail.cfm?id=26212. [Accessed: 17-Jul-2016].

[2] C. Acar and I. Dincer, "Impact assessment and efficiency evaluation of hydrogen production methods: Impact assessment and evaluation of hydrogen production methods," *Int. J. Energy Res.*, vol. 39, no. 13, pp. 1757–1768, Oct. 2015.

[3] J. R. Rostrup-Nielsen, J. Sehested, and J. K. Nørskov, "Hydrogen and synthesis gas by steam- and C02 reforming," vol. 47, B.-A. in Catalysis, Ed. Academic Press, 2002, pp. 65–139.

[4] C. Acar and I. Dincer, "Comparative assessment of hydrogen production methods from renewable and non-renewable sources," *Int. J. Hydrog. Energy*, vol. 39, no. 1, pp. 1–12, Jan. 2014.

[5] N. S. Lewis and D. G. Nocera, "Powering the planet: Chemical challenges in solar energy utilization," *Proc. Natl. Acad. Sci.*, vol. 103, no. 43, pp. 15729–15735, Oct. 2006.

[6] A. S. Joshi, I. Dincer, and B. V. Reddy, "Solar hydrogen production: A comparative performance assessment," *Int. J. Hydrog. Energy*, vol. 36, no. 17, pp. 11246–11257, Aug. 2011.

[7] O. J. Murphy and J. O. Bockris, "Photovoltaic electrolysis: Hydrogen and electricity from water and light," *Int. J. Hydrog. Energy*, vol. 9, no. 7, pp. 557–561, Jan. 1984.

[8] W. C. Chueh and S. M. Haile, "A thermochemical study of ceria: exploiting an old material for new modes of energy conversion and CO2 mitigation," *Philos. Trans. R. Soc. Lond. Math. Phys. Eng. Sci.*, vol. 368, no. 1923, pp. 3269–3294, Jul. 2010.

[9] S. Abanades and G. Flamant, “Thermochemical hydrogen production from a two-step solar-driven water-splitting cycle based on cerium oxides,” *Sol. Energy,* vol. 80, no. 12, pp. 1611–1623, 2006.

[10] N. W. Hurst, S. J. Gentry, A. Jones, and B. D. McNicol, “Temperature Programmed Reduction,” *Catal. Rev.*, vol. 24, no. 2, pp. 233–309, Jan. 1982.

[11] M. A. Reiche (CH-1), M. Maciejewski (CH-1), and A. Baiker (CH-1), “Characterization by temperature programmed reduction,” *Catal. Today*, vol. 56, no. 4, pp. 347–355, Mar. 2000.

[12] R. J. Gorte, “Temperature-programmed desorption for the characterization of oxide catalysts,” *Catal. Today,* vol. 28, no. 4, pp. 405–414, Sep. 1996.

[13] S. Hayun, T. Y. Shvareva, and A. Navrotsky, “Nanoceria – Energetics of Surfaces, Interfaces and Water Adsorption,” *J. Am. Ceram. Soc.*, vol. 94, no. 11, pp. 3992–3999, Nov. 2011.

[14] A. Trovarelli, “Catalytic Properties of Ceria and CeO2-Containing Materials,” *Catal. Rev.*, vol. 38, no. 4, pp. 439–520, Nov. 1996.

[15] A. Trovarelli, *Catalysis by Ceria and Related Materials*. World Scientific, 2002.

[67] T. Montini, M. Melchionna, M. Monai, and P. Fornasiero, “Fundamentals and Catalytic Applications of CeO2-Based Materials,” Chem. Rev., vol. 116, no. 10, pp. 5987–6041, May 2016.

[17] R. W. McCabe and A. Trovarelli, “Forty years of catalysis by ceria: A success story,” *Appl. Catal. B Environ.*, vol. 197, p. 1, Nov. 2016.

[18] R. J. Gorte, “Ceria in catalysis: From automotive applications to the water–gas shift reaction,” *AIChE J.*, vol. 56, no. 5, pp. 1126–1135, May 2010.

[19] A. Bueno-López, “Diesel soot combustion ceria catalysts,” *Appl. Catal. B Environ.*, vol. 146, pp. 1–11, Mar. 2014.

[20] X. Wang and R. J. Gorte, “Steam reforming of n-butane on Pd/ceria,” *Catal. Lett.*, vol. 73, no. 1, pp. 15–19, Apr. 2001.

[21] N. L. Wieder, M. Cargnello, K. Bakhmutsky, T. Montini, P. Fornasiero, and R. J. Gorte, “Study of the Water-Gas-Shift Reaction on Pd@CeO2/Al2O3 Core−Shell Catalysts,” *J. Phys. Chem. C,* vol. 115, no. 4, pp. 915–919, Feb. 2011.

[22] T. Shido and Y. Iwasawa, “Regulation of reaction intermediate by reactant in the water-gas shift reaction on CeO2, in relation to reactant-promoted mechanism,” *J. Catal.*, vol. 136, no. 2, pp. 493–503, Aug. 1992.

[23] G. S. Zafiris and R. J. Gorte, “Evidence for Low-Temperature Oxygen Migration from Ceria to Rh,” *J. Catal.*, vol. 139, no. 2, pp. 561–567, Feb. 1993.

[24] S. Scirè, S. Minicò, C. Crisafulli, C. Satriano, and A. Pistone, “Catalytic combustion of volatile organic compounds on gold/cerium oxide catalysts,” *Appl. Catal. B Environ.*, vol. 40, no. 1, pp. 43–49, Jan. 2003.

[25] D. Martin, R. Taha, and D. Duprez, “Effects of sintering and of additives on the oxygen storage capacity of PtRh catalysts,” in *Studies in Surface Science and Catalysis*, vol. 96, A. F. and J.-M. Bastin, Ed. Elsevier, 1995, pp. 801–811.

[26] G. R. Rao, “Influence of metal particles on the reduction properties of ceria-based materials studied by TPR,” *Bull. Mater. Sci.*, vol. 22, no. 2, pp. 89–94, Apr. 1999.

[27] M. F. L. Johnson and J. Mooi, “Cerium dioxide crystallite sizes by temperature-programmed reduction,” *J. Catal.*, vol. 103, no. 2, pp. 502–505, Feb. 1987.

[28] A. Trovarelli, F. Zamar, J. Llorca, C. de Leitenburg, G. Dolcetti, and J. T. Kiss, “Nanophase Fluorite-Structured CeO2–ZrO2Catalysts Prepared by High-Energy Mechanical Milling,” *J. Catal.*, vol. 169, no. 2, pp. 490–502, Jul. 1997.

[29] A. d. Logan and M. Shelef, “Oxygen availability in mixed cerium/praseodymium oxides and the effect of noble metals,” *J. Mater. Res.*, vol. 9, no. 2, pp. 468–475, Feb. 1994.

[30] B. Caglar and D. Uner, “NO oxidation and NOx storage over Ce–Zr mixed oxide supported catalysts,” *Catal. Commun.*, vol. 12, no. 6, pp. 450–453, Feb. 2011.

[31] B. Çağlar, “NOx Storage and Reduction Over Ce-Zr Mixed Oxide Supported Catalysts,” M.Sc. Thesis, Middle East Technical University, 2009.

[32] M. Haneda, T. Mizushima, N. Kakuta, A. Ueno, Y. Sato, S. Matsuura, K. Kasahara, and M. Sato, “Structural Characterization and Catalytic Behavior of

Al_2O_3-Supported Cerium Oxides," *Bull. Chem. Soc. Jpn.*, vol. 66, no. 4, pp. 1279–1288, 1993.

[33] J. Z. Shyu, W. H. Weber, and H. S. Gandhi, "Surface characterization of alumina-supported ceria," *J. Phys. Chem.*, vol. 92, no. 17, pp. 4964–4970, Aug. 1988.

[34] H. C. Yao and Y. F. Y. Yao, "Ceria in automotive exhaust catalysts," *J. Catal.*, vol. 86, no. 2, pp. 254–265, Apr. 1984.

[35] A. Trovarelli, G. Dolcetti, C. de Leitenburg, and J. Kaspar, "CO2 Hydrogenation Over Platinum Group Metals Supported on CeO2: Evidence for a Transient Metal-Support Interaction," in *Studies in Surface Science and Catalysis*, vol. 75, F. S. and P. T. L. GUCZI, Ed. Elsevier, 1993, pp. 2781–2784.

[36] U. Oran and D. Uner, "Mechanisms of CO oxidation reaction and effect of chlorine ions on the CO oxidation reaction over Pt/CeO2 and Pt/CeO2/γ-Al2O3 catalysts," *Appl. Catal. B Environ.*, vol. 54, no. 3, pp. 183–191, Dec. 2004.

[37] M. S. Brogan, T. J. Dines, and J. A. Cairns, "Raman spectroscopic study of the Pt–CeO2 interaction in the Pt/Al2O3–CeO2 catalyst," *J. Chem. Soc. Faraday Trans.*, vol. 90, no. 10, pp. 1461–1466, Jan. 1994.

[38] J. Z. Shyu and K. Otto, "Characterization of Pt/γ-alumina catalysts containing ceria," *J. Catal.*, vol. 115, no. 1, pp. 16–23, Jan. 1989.

[39] J. Z. Shyu, K. Otto, W. L. H. Watkins, G. W. Graham, R. K. Belitz, and H. S. Gandhi, "Characterization of Pd/γ-alumina catalysts containing ceria," *J. Catal.*, vol. 114, no. 1, pp. 23–33, Nov. 1988.

[40] L. Kepinski and M. Wolcyrz, "Microstructure of Pd/CeO2 catalyst: Effect of high temperature reduction in hydrogen," *Appl. Catal. -Gen.*, vol. 150, no. 2, pp. 197–220, Mar. 1997.

[41] R. de S. Monteiro, F. B. Noronha, L. C. Dieguez, and M. Schmal, "Characterization of PdCeO2 interaction on alumina support and hydrogenation of 1,3-butadiene," *Appl. Catal. Gen.*, vol. 131, no. 1, pp. 89–106, Oct. 1995.

[42] J. A. Farmer, J. H. Baricuatro, and C. T. Campbell, “Ag Adsorption on Reduced CeO $_2$ (111) Thin Films †,” *J. Phys. Chem. C*, vol. 114, no. 40, pp. 17166–17172, Oct. 2010.

[43] J. A. Farmer and C. T. Campbell, “Ceria Maintains Smaller Metal Catalyst Particles by Strong Metal-Support Bonding,” *Science*, vol. 329, no. 5994, pp. 933–936, Aug. 2010.

[44] T. Bunluesin, R. J. Gorte, and G. W. Graham, “Studies of the water-gas-shift reaction on ceria-supported Pt, Pd, and Rh: Implications for oxygen-storage properties,” *Appl. Catal. B Environ.*, vol. 15, no. 1, pp. 107–114, Jan. 1998.

[45] C. Wen, Y. Zhu, Y. Ye, S. Zhang, F. Cheng, Y. Liu, P. Wang, and F. Tao, “Water-Gas Shift Reaction on Metal Nanoclusters Encapsulated in Mesoporous Ceria Studied with Ambient-Pressure X-ray Photoelectron Spectroscopy,” *Acs Nano*, vol. 6, no. 10, pp. 9305–9313, Oct. 2012.

[46] S. Y. Christou and A. M. Efstathiou, “Effects of Pd particle size on the rates of oxygen back-spillover and CO oxidation under dynamic oxygen storage and release measurements over Pd/CeO2 catalysts,” *Top. Catal.*, vol. 42–43, no. 1–4, pp. 351–355, May 2007.

[47] R. Craciun, W. Daniell, and H. Knözinger, “The effect of CeO2 structure on the activity of supported Pd catalysts used for methane steam reforming,” *Appl. Catal. Gen.*, vol. 230, no. 1–2, pp. 153–168, Apr. 2002.

[48] A. Yee, S. J. Morrison, and H. Idriss, “A study of the reactions of ethanol on CeO2 and Pd/CeO2 by steady state reactions, temperature programmed desorption, and in situ FT-IR,” *J. Catal.*, vol. 186, no. 2, pp. 279–295, Sep. 1999.

[49] B. Wang, D. Weng, X. Wu, and J. Fan, “Influence of H-2/O-2 redox treatments at different temperatures on Pd-CeO2 catalyst: Structure and oxygen storage capacity,” *Catal. Today*, vol. 153, no. 3–4, pp. 111–117, Aug. 2010.

[50] A. Steinfeld, “Solar hydrogen production via a two-step water-splitting thermochemical cycle based on Zn/ZnO redox reactions,” *Int. J. Hydrog. Energy*, vol. 27, no. 6, pp. 611–619, Jun. 2002.

[51] M. Kromer, K. Roth, R. Takata, and P. Chin, “Support for cost analyses on solar-driven high temperature thermochemical water-splitting cycles,” *TIAX, LLC, Report*, 2011.

[52] P. Charvin, S. Abanades, F. Lemont, and G. Flamant, “Experimental study of SnO2/SnO/Sn thermochemical systems for solar production of hydrogen,” *AIChE J.*, vol. 54, no. 10, pp. 2759–2767, Oct. 2008.

[53] T. Nakamura, “Hydrogen production from water utilizing solar heat at high temperatures,” *Sol. Energy*, vol. 19, no. 5, pp. 467–475, 1977.

[54] C. Agrafiotis, A. Zygogianni, C. Pagkoura, M. Kostoglou, and A. G. Konstandopoulos, “Hydrogen production via solar-aided water splitting thermochemical cycles with nickel ferrite: Experiments and modeling,” *AIChE J.*, vol. 59, no. 4, pp. 1213–1225, Apr. 2013.

[55] J. R. Scheffe, D. Weibel, and A. Steinfeld, “Lanthanum–Strontium–Manganese Perovskites as Redox Materials for Solar Thermochemical Splitting of H2O and CO2,” *Energy Fuels*, vol. 27, no. 8, pp. 4250–4257, Aug. 2013.

[56] A. H. McDaniel, E. C. Miller, D. Arifin, A. Ambrosini, E. N. Coker, R. O’Hayre, W. C. Chueh, and J. Tong, “Sr- and Mn-doped LaAlO3−δ for solar thermochemical H2 and CO production,” *Energy Environ. Sci.*, vol. 6, no. 8, p. 2424, 2013.

[57] W. C. Chueh and S. M. Haile, “Ceria as a Thermochemical Reaction Medium for Selectively Generating Syngas or Methane from H2O and CO2,” *ChemSusChem*, vol. 2, no. 8, pp. 735–739, Aug. 2009.

[58] A. Le Gal, S. Abanades, and G. Flamant, “CO2 and H2O Splitting for Thermochemical Production of Solar Fuels Using Nonstoichiometric Ceria and Ceria/Zirconia Solid Solutions,” *Energy Fuels*, vol. 25, no. 10, pp. 4836–4845, Oct. 2011.

[59] H. Kaneko, H. Ishihara, S. Taku, Y. Naganuma, N. Hasegawa, and Y. Tamaura, “Cerium ion redox system in CeO2–xFe2O3 solid solution at high temperatures (1,273–1,673 K) in the two-step water-splitting reaction for solar H2 generation,” *J. Mater. Sci.*, vol. 43, no. 9, pp. 3153–3161, Feb. 2008.

[60] H. Kaneko, T. Miura, H. Ishihara, S. Taku, T. Yokoyama, H. Nakajima, and Y. Tamaura, “Reactive ceramics of CeO2–MOx (M=Mn, Fe, Ni, Cu) for H2 generation by two-step water splitting using concentrated solar thermal energy,” *Energy*, vol. 32, no. 5, pp. 656–663, May 2007.

[61] T. Rager and J. Golczewski, “Solar-Thermal Zinc Oxide Reduction Assisted by a Second Redox Pair,” *Z. Für Phys. ChemieInternational J. Res. Phys. Chem. Chem. Phys.*, vol. 219, no. 2/2005, pp. 235–246, 2008.

[62] M. Roeb, M. Neises, N. Monnerie, F. Call, H. Simon, C. Sattler, M. Schmücker, and R. Pitz-Paal, “Materials-Related Aspects of Thermochemical Water and Carbon Dioxide Splitting: A Review,” *Materials*, vol. 5, no. 11, pp. 2015–2054, Oct. 2012.

[63] “It’s Elemental - The Element Cadmium.” [Online]. Available: http://education.jlab.org/itselemental/ele048.html. [Accessed: 29-Jun-2016].

[64] D. Souria, “Souriau D. Process and set-up for thermal energy use at high temperature, in particular nuclear energy,” Patent no. 2135421, 1971.

[65] N. Gokon, S. Takahashi, H. Yamamoto, and T. Kodama, “Thermochemical two-step water-splitting reactor with internally circulating fluidized bed for thermal reduction of ferrite particles,” *Int. J. Hydrog. Energy*, vol. 33, no. 9, pp. 2189–2199, May 2008.

[66] F. Fresno, R. Fernández-Saavedra, M. Belén Gómez-Mancebo, A. Vidal, M. Sánchez, M. Isabel Rucandio, A. J. Quejido, and M. Romero, “Solar hydrogen production by two-step thermochemical cycles: Evaluation of the activity of commercial ferrites,” *Int. J. Hydrog. Energy*, vol. 34, no. 7, pp. 2918–2924, Apr. 2009.

[67] J. E. Miller, M. D. Allendorf, R. B. Diver, L. R. Evans, N. P. Siegel, and J. N. Stuecker, “Metal oxide composites and structures for ultra-high temperature solar thermochemical cycles,” *J. Mater. Sci.*, vol. 43, no. 14, pp. 4714–4728, Apr. 2008.

[68] T. Kodama, T. Shimizu, T. Satoh, M. Nakata, and K.-I. Shimizu, “Stepwise production of CO-rich syngas and hydrogen via solar methane reforming by using a Ni(II)–ferrite redox system,” *Sol. Energy*, vol. 73, no. 5, pp. 363–374, Nov. 2002.

[69] S. M. Haile, “Fuel cell materials and components☆☆,” *Acta Mater.*, vol. 51, no. 19, pp. 5981–6000, Nov. 2003.

[70] R. Craciun, B. Shereck, and R. J. Gorte, “Kinetic studies of methane steam reforming on ceria-supported Pd,” *Catal. Lett.*, vol. 51, no. 3–4, pp. 149–153, May 1998.

[71] K. Otsuka, M. Hatano, and A. Morikawa, “Hydrogen from water by reduced cerium oxide,” *J. Catal.*, vol. 79, no. 2, pp. 493–496, Feb. 1983.

[72] W. C. Chueh, C. Falter, M. Abbott, D. Scipio, P. Furler, S. M. Haile, and A. Steinfeld, “High-Flux Solar-Driven Thermochemical Dissociation of CO2 and H2O Using Nonstoichiometric Ceria,” *Science*, vol. 330, no. 6012, pp. 1797–1801, Dec. 2010.

[73] N. D. Petkovich, S. G. Rudisill, L. J. Venstrom, D. B. Boman, J. H. Davidson, and A. Stein, “Control of Heterogeneity in Nanostructured Ce1-xZrxO2 Binary Oxides for Enhanced Thermal Stability and Water Splitting Activity,” *J. Phys. Chem. C*, vol. 115, no. 43, pp. 21022–21033, Nov. 2011.

[74] B. Dernaika and D. Uner, “A simplified approach to determine the activation energies of uncatalyzed and catalyzed combustion of soot,” *Appl. Catal. B Environ.*, vol. 40, no. 3, pp. 219–229, Feb. 2003.

[75] H. E. Kissinger, “Variation of peak temperature with heating rate in differential thermal analysis,” *J. Res. Natl. Bur. Stand.*, vol. 57, no. 4, pp. 217–221, 1956.

[76] M. Ozawa and M. Kimura, “Effect of cerium addition on the thermal stability of gamma alumina support,” *J. Mater. Sci. Lett.*, vol. 9, no. 3, pp. 291–293.

[77] V. Ferrer, A. Moronta, J. Sánchez, R. Solano, S. Bernal, and D. Finol, “Effect of the reduction temperature on the catalytic activity of Pd-supported catalysts,” *Catal. Today*, vol. 107–108, pp. 487–492, Oct. 2005.

[78] Y. Tonbul, S. Akbayrak, and S. Özkar, “Palladium(0) nanoparticles supported on ceria: Highly active and reusable catalyst in hydrogen generation from the hydrolysis of ammonia borane,” *Int. J. Hydrog. Energy*, vol. 41, no. 26, pp. 11154–11162, Jul. 2016.

[79] S. Gil, J. M. Garcia-Vargas, L. F. Liotta, G. Pantaleo, M. Ousmane, L. Retailleau, and A. Giroir-Fendler, “Catalytic Oxidation of Propene over Pd Catalysts Supported on CeO2, TiO2, Al2O3 and M/Al2O3 Oxides (M = Ce, Ti, Fe, Mn),” *Catalysts*, vol. 5, no. 2, pp. 671–689, Apr. 2015.

[80] X. Wang, R. J. Gorte, and J. P. Wagner, “Deactivation Mechanisms for Pd/Ceria during the Water–Gas-Shift Reaction,” *J. Catal.*, vol. 212, no. 2, pp. 225–230, Dec. 2002.

[81] D. Uner and L. K. Doraiswamy, “Chemical Reaction Engineering: Beyond the Fundamentals,” *CRC Press*, 15-Jul-2013. [Online]. Available: https://www.crcpress.com/Chemical-Reaction-Engineering-Beyond-the-Fundamentals/Doraiswamy-Uner/p/book/9781439831229. [Accessed: 26-Sep-2016].

[82] D. Uner, N. A. Tapan, İ. Özen, and M. Üner, “Oxygen adsorption on Pt/TiO2 catalysts,” *Appl. Catal. Gen.*, vol. 251, no. 2, pp. 225–234, Sep. 2003.

[83] C. Agrafiotis, M. Roeb, and C. Sattler, “A review on solar thermal syngas production via redox pair-based water/carbon dioxide splitting thermochemical cycles,” *Renew. Sustain. Energy Rev.*, vol. 42, pp. 254–285, Feb. 2015.

APPENDIX A

MICROMERITICS CHEMISORB 2720

In Micromeritics ChemiSorb 2720 TPx equipment, flowing gas technique is used for analysis. Different analysis can be performed in this system such as; temperature programmed reduction (TPR), temperature programmed oxidation (TPO), temperature programmed thermal decomposition (TPtD), pulse chemisorption and physisorption. Different reactive gases such as; carbon dioxide (CO_2), oxygen (O_2), air (O_2+N_2), hydrogen sulfide (H_2S), ammonia (NH_3) and different carrier gases such as; helium (He), argon (Ar), nitrogen (N_2) can be used for analysis. There is a programmable furnace which heats the sample tube while the gas flows through the sample. Temperature of the furnace can be increased up to 1100 °C at a maximum rate of 50 °C /min and the furnace controller can be programmed to provide different ramps and dwell times. A downstream thermal conductivity detector (TCD) monitors the adsorbed amount of gas by the sample while heating and a thermocouple monitors the temperature of the sample by using ChemiSorb TPx V1.03 software. Temperature programmed chemisorption experiments provide the calculation of the amount of physical or chemical adsorption by using the TCD signal and temperature data if the sample is active at elevated temperatures.

APPENDIX B

EXPERIMENTAL PROCEDURES

B.1. TPx Experimental Procedures

1. Place the sample on a quartz wool bed in a u-shaped quartz reactor and position vertically in a programmable tube furnace in Micromeritics ChemiSorb 2720. Lock the furnace and place isolation wool on the top of the furnace.
2. For TPR measurements, install cold trap with ice-water mixture and place isolation wool on the top of cold trap bed.
3. Switch ‘By-pass’ and ‘Short Path’ for ‘Path Select’ and ‘Delay’ valves, respectively.
4. Switch helium (Port A) on Micromeritics ChemiSorb 2720.
5. Open helium gas cylinder.
6. Turn Micromeritics ChemiSorb 2720 on.
7. Set the flow rate of gas to 25-30 sccm by using rotameter on Micromeritics ChemiSorb 2720.
8. Turn TPx on.
9. Turn the computer on. After that, open ChemiSorb TPx V1.03 software.
10. In ChemiSorb TPx V1.03 software, select ‘File/Open/Sample’.
11. In ‘Sample Information’ tab, write sample type, experiment name and the amount of sample.
12. In ‘Analysis Condition’ tab, select the experiment as TPR, TPO or TPtD.
13. In ‘Report Options’ tab, select the data which are wanted to be reported.
14. In ChemiSorb TPx V1.03 software, select ‘Unit 1/Start Analysis’.

Follow the steps for TPR, TPO or TPtD given below.

B.1.1. TPR Experiments

1. Purge the by-pass and short path lines with helium (Port A) while ‘By-pass’ and ‘Short Path’ valves are open. Wait until the signal is stabilized.
2. Switch ‘Sample’ and ‘Long Path’ for ‘Path Select’ and ‘Delay’ valves, respectively.
3. Purge the sample and long path lines with helium (Port A) while ‘Sample’ and ‘Long Path’ valves are open. Wait until the signal is stabilized.
4. Switch (-) ‘Polarity’ on Micromeritics ChemiSorb 2720.
5. Open 10 % H_2-Ar gas cylinder.
6. Switch hydrogen (Port B) on Micromeritics ChemiSorb 2720.
7. Wait until the baseline is stable.
8. Set the maximum temperature, ramp and dwell time on TPx. Start heating on TPx.
9. Start recording TCD signal, temperature and time data.
10. Close data recording when the maximum temperature is reached.
11. Stop heating on TPx.
12. Wait for the temperature of sample is 400 °C.
13. Open the furnace lock and cooling fan on Micromeritics ChemiSorp 2720.
14. Wait for the temperature of sample is at room temperature.
15. Switch helium (Port A) on Micromeritics ChemiSorb 2720.
16. Purge the sample and long path lines with helium (Port A) while ‘Sample’ and ‘Long Path’ valves are open. Wait until the signal is stabilized.
17. Switch ‘By-pass’ and ‘Short Path’ for ‘Path Select’ and ‘Delay’ valves, respectively.
18. Purge the by-pass and short path lines with helium (Port A) while ‘By-pass’ and ‘Short Path’ valves are open. Wait until the signal is stabilized.
19. Close ChemiSorb TPx V1.03 software. Turn the computer, TPx and Micromeritics ChemiSorb 2720 off.
20. Close He and 10 % H_2-Ar gas cylinders.

B.1.2. TPO Experiments

1. Purge the by-pass and short path lines with helium (Port A) while ‘By-pass’ and ‘Short Path’ valves are open. Wait until the signal is stabilized.
2. Switch ‘Sample’ and ‘Long Path’ for ‘Path Select’ and ‘Delay’ valves, respectively.
3. Purge the sample and long path lines with helium (Port A) while ‘Sample’ and ‘Long Path’ valves are open. Wait until the signal is stabilized.
4. Switch (+) ‘Polarity’ on Micromeritics ChemiSorb 2720.
5. Open 2 % O_2-He gas cylinder.
6. Switch oxygen (Port D) on Micromeritics ChemiSorb 2720.
7. Wait until the baseline is stable.
8. Set the maximum temperature, ramp and dwell time on TPx. Start heating on TPx.
9. Start recording TCD signal, temperature and time data.
10. Close data recording when the maximum temperature is reached.
11. Stop heating on TPx.
12. Wait for the temperature of sample is 400 °C.
13. Open the furnace lock and cooling fan on Micromeritics ChemiSorb 2720.
14. Wait for the temperature of sample is at room temperature.
15. Switch helium (Port A) on Micromeritics ChemiSorb 2720.
16. Purge the sample and long path lines with helium (Port A) while ‘Sample’ and ‘Long Path’ valves are open. Wait until the signal is stabilized.
17. Switch ‘By-pass’ and ‘Short Path’ for ‘Path Select’ and ‘Delay’ valves, respectively.
18. Purge the by-pass and short path lines with helium (Port A) while ‘By-pass’ and ‘Short Path’ valves are open. Wait until the signal is stabilized.
19. Close ChemiSorb TPx V1.03 software. Turn the computer, TPx and Micromeritics ChemiSorb 2720 off.
20. Close He and 2 % O_2-He gas cylinders.

B.1.3. TPtD Experiments

1. Purge the by-pass and short path lines with helium (Port A) while ‘By-pass’ and ‘Short Path’ valves are open. Wait until the signal is stabilized.
2. Switch ‘Sample’ and ‘Long Path’ for ‘Path Select’ and ‘Delay’ valves, respectively.
3. Purge the sample and long path lines with helium (Port A) while ‘Sample’ and ‘Long Path’ valves are open. Wait until the signal is stabilized.
4. Switch (-) ‘Polarity’ on Micromeritics ChemiSorb 2720.
5. Wait until the baseline is stable.
6. Set the maximum temperature, ramp and dwell time on TPx. Start heating on TPx.
7. Start recording TCD signal, temperature and time data.
8. Close data recording when the maximum temperature is reached.
9. Stop heating on TPx.
10. Wait for the temperature of sample is 400 °C.
11. Open the furnace lock and cooling fan on Micromeritics ChemiSorb 2720.
12. Wait for the temperature of sample is at room temperature.
13. Switch ‘By-pass’ and ‘Short Path’ for ‘Path Select’ and ‘Delay’ valves, respectively.
14. Purge the by-pass and short path lines with helium (Port A) while ‘By-pass’ and ‘Short Path’ valves are open. Wait until the signal is stabilized.
15. Close ChemiSorb TPx V1.03 software. Turn the computer, TPx and Micromeritics ChemiSorb 2720 off.
16. Close He gas cylinder.

B.2. Chemisorption Experimental Procedures

1. Evacuate the chemisorption manifold.
2. Attach the sample tube to the system.
3. Purge the system with helium while sample tube is heated up to 150 °C.
4. Increase the temperature up to 350 °C.
5. Open V10 and V12 and evacuate the system for 10 minutes.
6. Flush the system with hydrogen.
7. Reduce the sample with hydrogen at 350 °C for 4 times. (30 minutes reduction and 10 minutes evacuation at 350 °C). Record the temperature and system pressure data.
8. Evacuate the system for 1 hour at 350 °C.
9. Evacuate the system overnight at room temperature. (~30 °C)
10. Dose hydrogen (~ 1-20 torr) to the system (open V3, V4, V5, V6, V7) at room temperature (~30 °C) for total adsorption measurement.
11. Record system pressure as P_1.
12. Close V7 and open V10 and wait for 5 minutes to approach the system at steady state. Record P_2 as reduced pressure.
13. Close V10 and record the system pressure as P_3.
14. Open V12 and evacuate the system for 10 minutes.
15. Repeat the same procedure after dosing hydrogen at different amounts (~ 1-20 torr) for weak adsorption measurement.

Or

16. Set P_1 to 0.1 torr, until no more adsorption takes place. Then, set P_1 as 0.2, 0.4, 1, 2, 5, 10, 20, 40, 60, 80 and 100 torr pressures. After 5 minutes, record P_2 and P_3.
17. Evacuated the system for 10 minutes.
18. Close V10 and flush the system with helium. Record P_1, P_2 and P_3 for dead volume measurement.

B.3. Microcalorimetry Experimental Procedures

1. Evacuate the microcalorimetry manifold.
2. Load the sample into the sample cell and place it into calorimetry.
3. Heat the sample up to 250 °C at a rate of 2 °C/min.
4. Dose hydrogen to the sample (open V3, V4, V5, V6, V7, V9) to reduce the surface.
5. Cool the sample to 150 °C at a rate of 2 °C/min.
6. Dose hydrogen or oxygen (~ 0-200 torr) to the system (for hydrogen; open V3, V4, V5, V6, V7; for oxygen; open V2, V4, V5, V6, V7) at 150 °C.
7. Record system pressure as P_1.
8. Close V7 and open V9 and wait for 5 minutes to approach the system at steady state. Record P_2 as reduced pressure.
9. Close V9 and record the system pressure as P_3.
10. Open V10 and evacuate the system for 10 minutes.
11. Repeat the same procedure after dosing hydrogen at different amounts (~ 0-200 torr).

APPENDIX C

CALCULATIONS

C.1. Hydrogen Consumption Calculations

C.1.1. Calibration with Reference Material: Ag_2O

As a reference material, Ag_2O was used to determine the hydrogen consumption amount by peak area analysis. In Figure C.1, TPR pattern for Ag_2O is given. It is seen that reduction peak temperature is 122.1 °C which is in the range 119∓15 °C reported by Micromeritics.

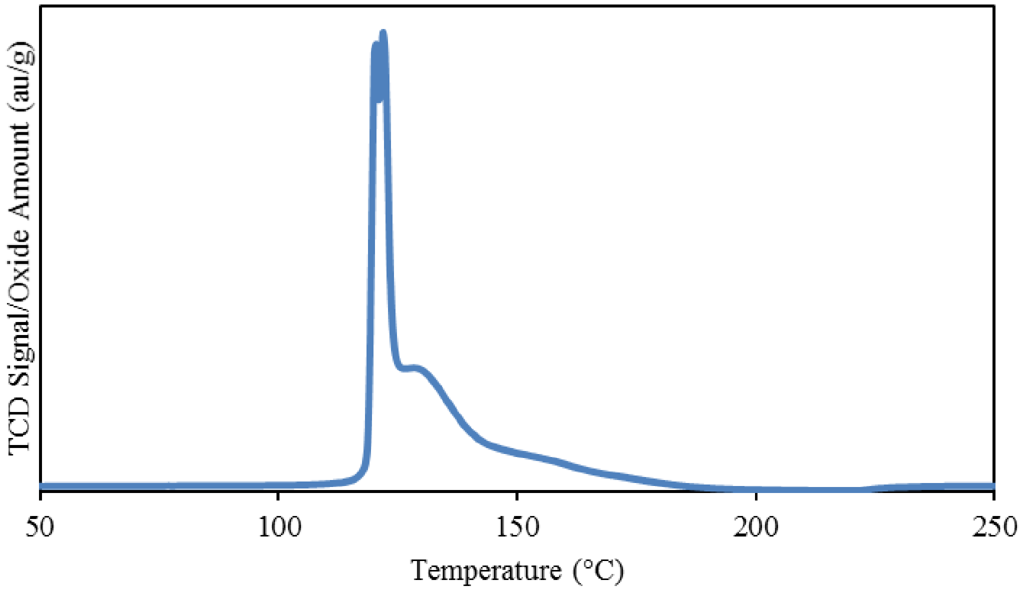

Figure C.1 TPR pattern of Ag_2O at 10 °C/min heating rate under 25 sccm 10 % H_2-Ar flow

In Table C.1, initial, final and consumed amounts of Ag_2O are given.

Table C.1 Ag_2O amounts in TPR analysis

	Mass (g)	**Mol**
Initial amount (Ag_2O)	0.024	$1.03*10^{-4}$
Final amount (2Ag)	0.019	$1.82*10^{-4}$
Amount used in reaction (O)	$4.30*10^{-3}$	$2.69*10^{-4}$

$$Ag_2O + H_2 \rightarrow 2\ Ag + H_2O \qquad \text{Equation C.1}$$

For 1 mol of Ag_2O, 1 mol of H_2 is consumed in TPR according to Equation C.1. Therefore, for $1.031*10^{-4}$ mol O, $1.031*10^{-4}$ mol or $2.062*10^{-4}$ g H_2 was consumed. Area under the peak was calculated as 1.4116 by using Matlab Interactive Peak Fitter tool. Therefore, 1 unit area corresponds to $7.30*10^{-5}$ mol or $1.46*10^{-4}$ g H_2 amount.

$$0.0239\ g\ Ag_2O.\frac{1\ mol\ Ag_2O}{231.74\ g\ Ag_2O}.\frac{2\ moles\ Ag}{1\ mol\ Ag_2O}.\frac{107.8682\ g\ Ag}{1\ mol\ Ag} = 0.0222\ g\ Ag\ initially\ and\ 0.0196\ g\ Ag\ finally$$

Volume of H_2 consumed was calculated by ideal gas law at standard conditions (1 bar, 0 °C).

$$1\ bar.V\ m^3 = 1.031 * 10^{-4} mol\ H_2 . 8.314 * 10^{-5}\frac{m^3.bar}{mol.K}.273\ K$$

$$V = 2.34 * 10^{-6} m^3.\frac{10^6 cm^3}{1\ m^3} = 2.34\ cm^3\ H_2$$

Hydrogen consumption was calculated as 97.9 $\frac{cm^3 H_2}{g\ Ag_2O}$ which is reported as 93.9 ∓ 3 $\frac{cm^3 H_2}{g\ Ag_2O}$ by Micromeritics.

C.1.2. CeO_2

Table C.2 Calculated hydrogen consumption for CeO_2 using stoichiometry

	CeO_2
Initial CeO_2 amount (g)	0.0250
Initial CeO_2 amount (mol)	$1.45*10^{-4}$
CeO_2 hydrogen consumption (mol)	$7.27*10^{-5}$

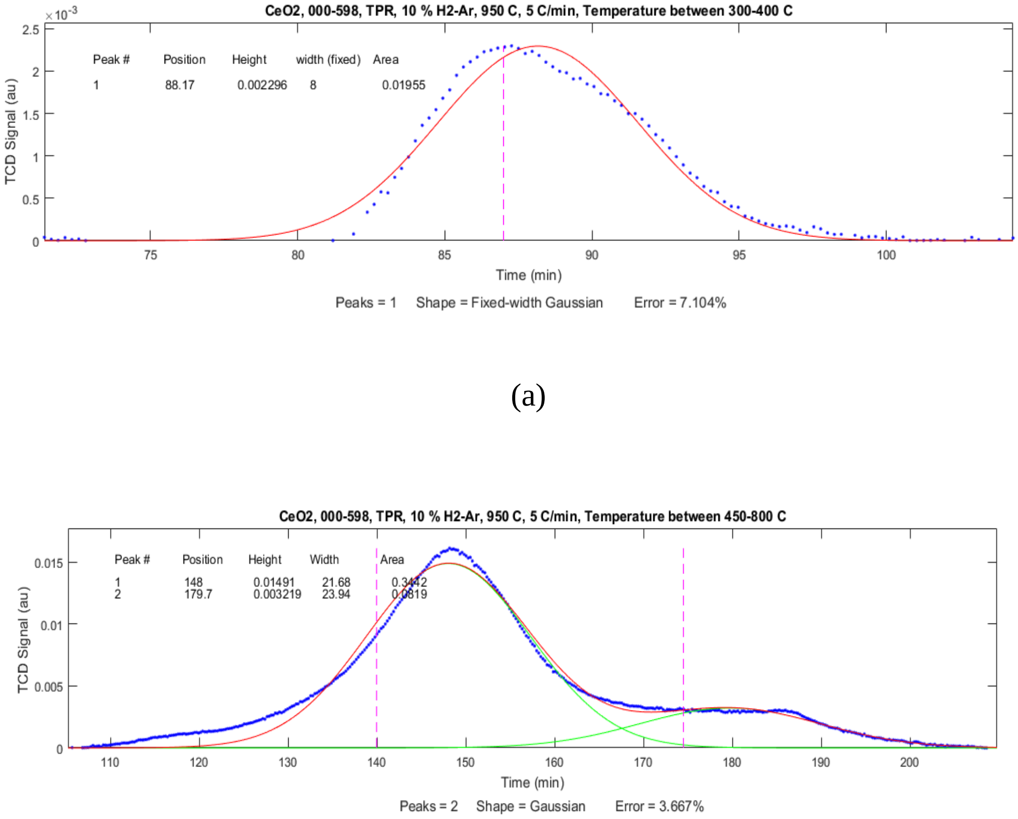

(a)

(b)

Figure C.2 Hydrogen consumption area calculations for CeO_2 during TPR using Matlab Interactive Peak Fitter tool

C.1.3. 1 % Pd/CeO_2

Table C.3 Calculated hydrogen consumption for 1 % Pd/CeO_2 using stoichiometry

	1 % Pd/CeO_2
Initial oxide amount (g)	0.0608
Initial Pd amount (g)	$6.08*10^{-4}$
Initial Pd amount (mol)	$5.71*10^{-6}$
PdO hydrogen consumption (mol)	$5.71*10^{-6}$
Initial CeO_2 amount (g)	0.0602
Initial CeO_2 amount (mol)	$3.49*10^{-4}$
CeO_2 hydrogen consumption (mol)	$1.75*10^{-4}$

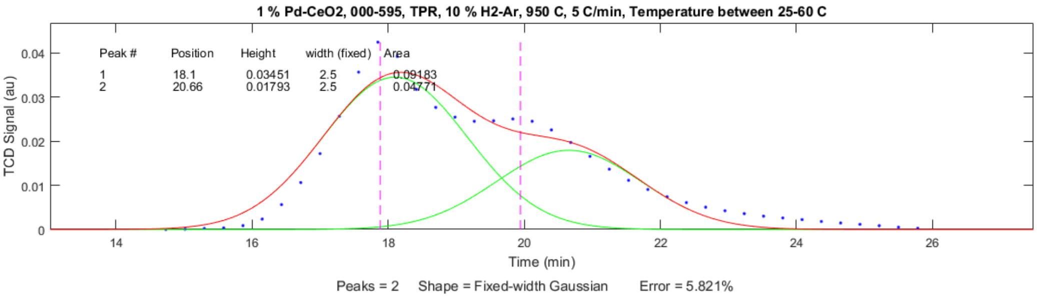

(a)

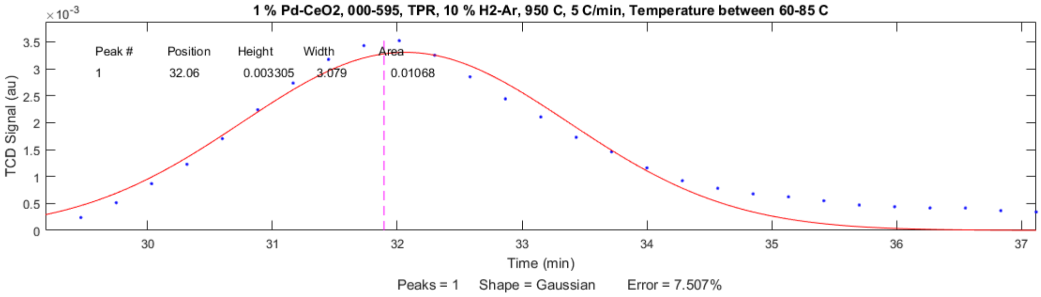

(b)

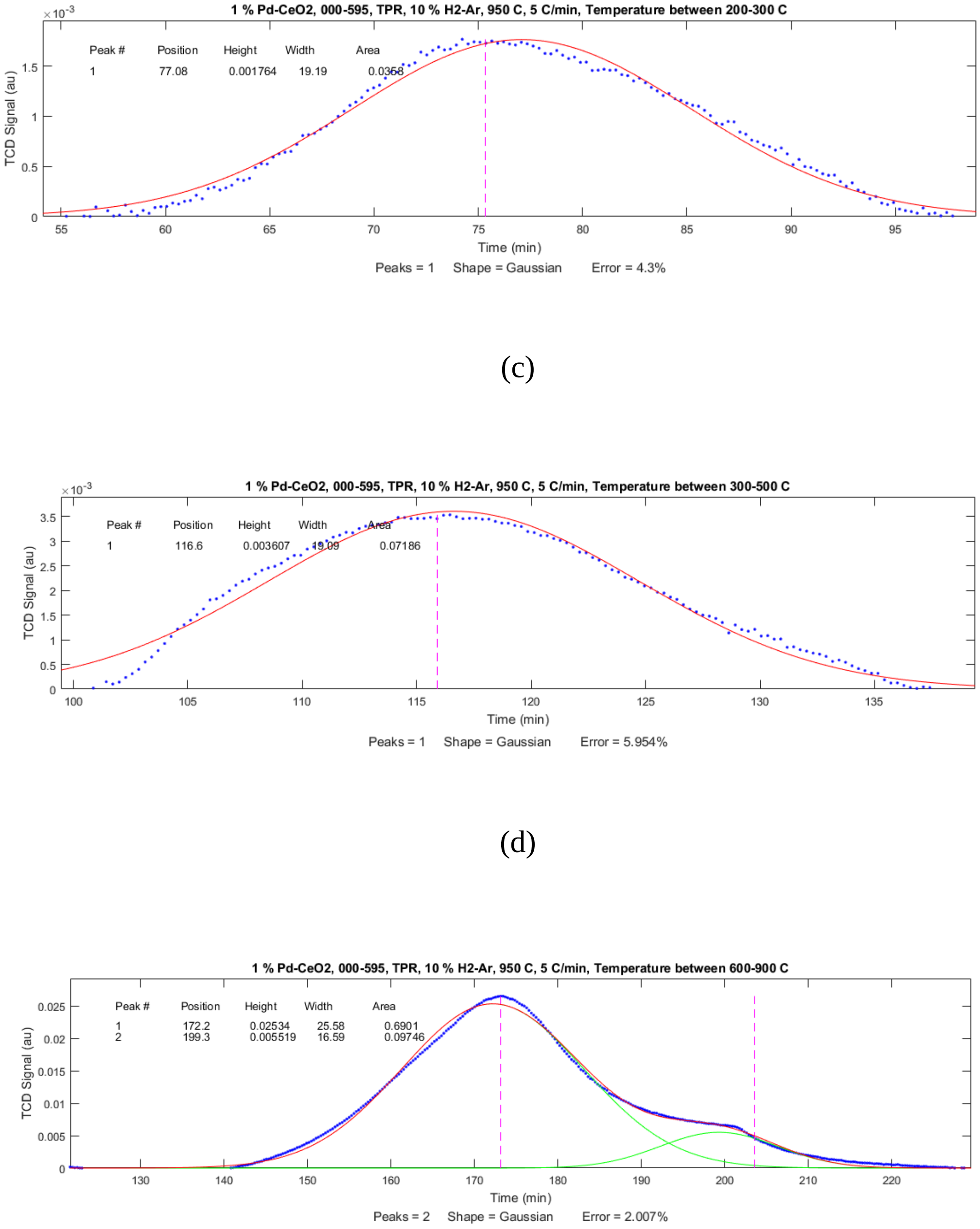

(c)

(d)

(e)

Figure C.3 Hydrogen consumption area calculations for 1 % Pd/CeO_2 during TPR using Matlab Interactive Peak Fitter tool

C.1.4. 1 % Pd/CeO_2-Al_2O_3

Table C.4 Calculated hydrogen consumption for 1 % Pd/CeO_2-Al_2O oxides using stoichiometry

	1 % Pd/20 % CeO_2-Al_2O_3	**1 % Pd/15 % CeO_2-Al_2O_3**	**1 % Pd/10 % CeO_2-Al_2O_3**
Initial oxide amount (g)	0.042	0.036	0.021
Initial Pd amount (g)	$4.22*10^{-4}$	$3.58*10^{-4}$	$2.10*10^{-4}$
Initial Pd amount (mol)	$3.97*10^{-6}$	$3.36*10^{-6}$	$1.97*10^{-6}$
PdO hydrogen consumption calculated by stoichiometry (mol)	$3.97*10^{-6}$	$3.36*10^{-6}$	$1.97*10^{-6}$
Initial CeO_2 amount (g)	$8.36*10^{-3}$	$5.32*10^{-3}$	$2.08*10^{-3}$
Initial CeO_2 amount (mol)	$4.86*10^{-5}$	$3.09*10^{-5}$	$1.21*10^{-5}$
CeO_2 hydrogen consumption calculated by stoichiometry (mol)	$2.43*10^{-5}$	$1.55*10^{-5}$	$6.04*10^{-6}$

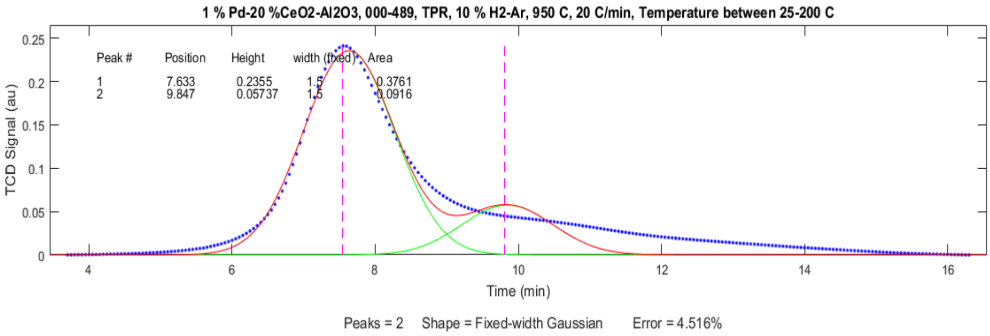

(a)

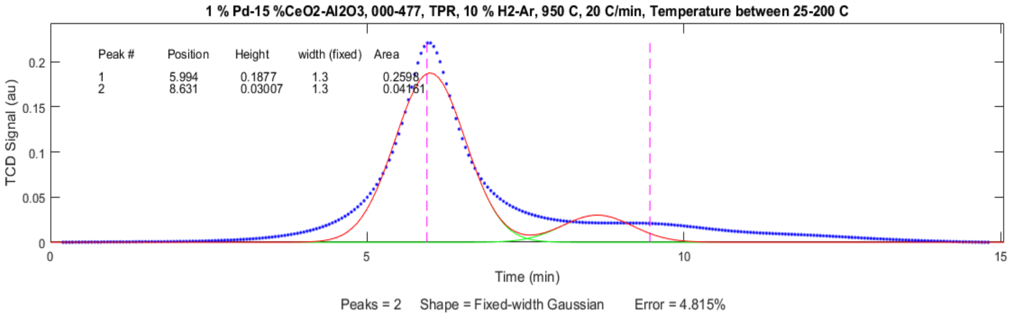

(b)

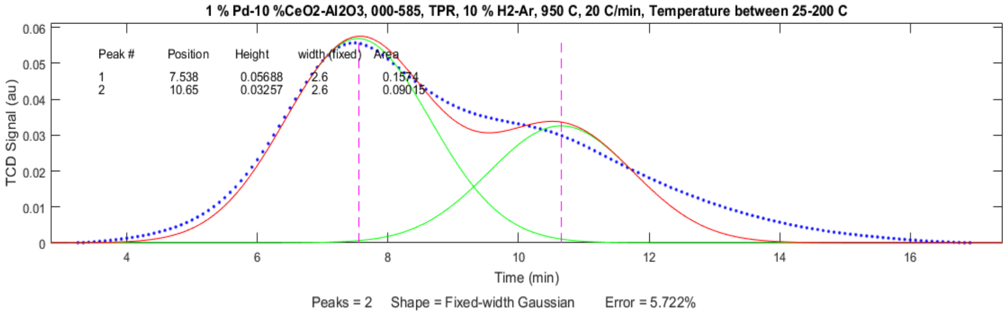

(c)

Figure C.4 Hydrogen consumption area calculations for 1 % Pd/CeO$_2$-Al$_2$O$_3$ oxides during TPR using Matlab Interactive Peak Fitter tool

C.2. Oxygen Calibration with Air Injection

In order to calibrate oxygen uptake/release amount, air injection experiments were performed in Micromeritics Chemisorb 2720. In Figure C.5, air injection peaks are given.

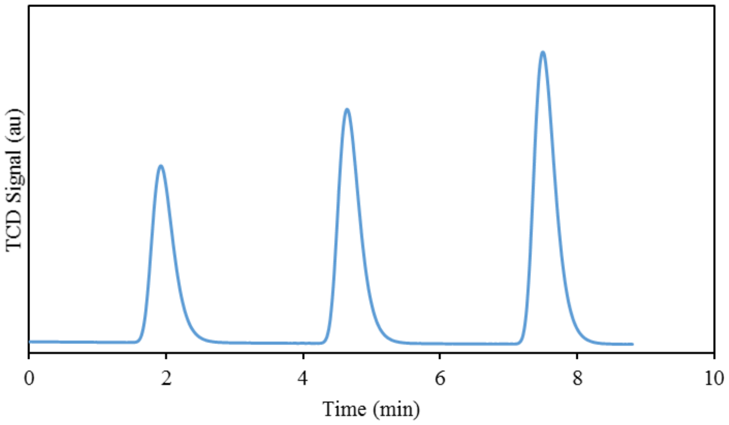

Figure C.5 Air injection experiments for oxygen calibration

Oxygen amounts in injected air were calculated and sample calculation for first injection is given below assuming that air has 20.95 % O_2 by volume and air is an ideal gas with 24.5 dm^3/mol molar volume.

$$0.3\ mL\ air.\frac{20.95\ \%\ O_2}{100}.\frac{1\ L}{10^3\ mL}.\frac{1\ m^3}{10^3\ L}.\frac{10^3\ dm^3}{1\ m^3}.\frac{1\ mol}{24.5\ dm^3}_{at\ 25°C,1\ atm} = 2.569 * 10^{-6}\ mol\ O_2$$

Peak areas were calculated by using Matlab Interactive Peak Fitter tool. In Table C.5, injection amounts are tabulated for each injection.

Table C.5 Air injection and corresponding oxygen amounts

	Air Volume (mL)	**Oxygen Amount (mol)**	**Peak Area**
1st Injection	0.3	$2.569*10^{-6}$	0.056
2nd Injection	0.4	$3.425*10^{-6}$	0.074
3rd Injection	0.5	$4.281*10^{-6}$	0.091

Calibration plot is given in Figure C.6 below. Linear trendline with zero intercept was plotted to understand the relation between area and oxygen amount. Oxygen release/uptake amounts can be quantitatively calculated by using equation in Figure C.6.

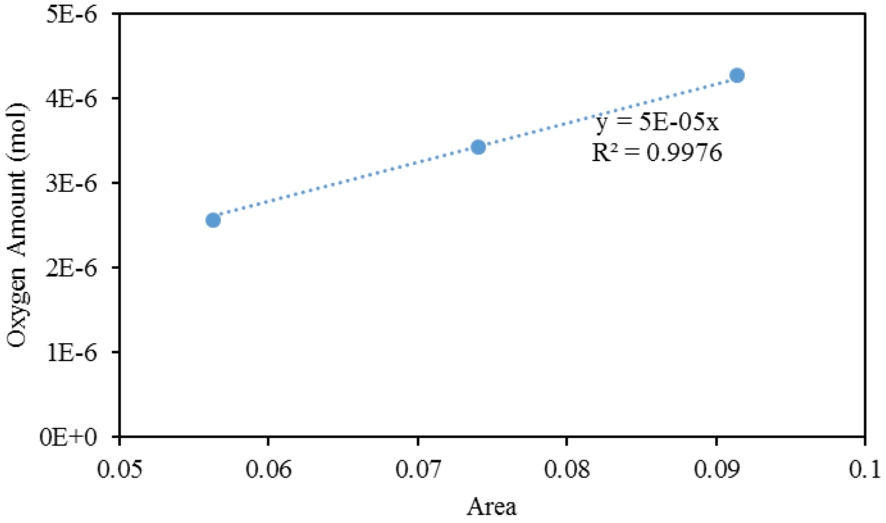

Figure C.6 Oxygen calibration plot for Micromeritics Chemisorb 2720

C.3. Surface Atom Percentage Calculation

Surface atom percentage for CeO_2 was calculated for all synthesized oxides using surface area data. Sample calculation for 1 % Pd/CeO_2 is given below and in Table C.6, surface atom percentage data for all prepared oxides are given.

$$\%\,\boldsymbol{Surface\ Atoms} = 3.8\ \frac{m^2}{g}.10^4\frac{cm^2}{m^2}.10^{15}\frac{sites}{cm^2}.\frac{1\,mol}{6.02*10^{23}sites}.\frac{172.115\,g}{1\,mol}.100 = 1.09\ \%$$

Table C.6 Percentage CeO_2 surface atoms for synthesized oxides

Oxide	**BET surface area (m^2/g)**	**CeO_2 surface atoms (%)**
CeO_2	2.9	0.83
1 % Pd/CeO_2	3.8	1.09
1 % Pd/20 % CeO_2-Al_2O_3	56.1	16.03
1 % Pd/15 % CeO_2-Al_2O_3	55.6	15.89
1 % Pd/10 % CeO_2-Al_2O_3	60.4	17.26

C.4. Activation Energy Calculations

C.4.1. Redhead Method

Activation energies for TPtD experiments were calculated by Redhead method and Equation 3.5 using MathCad. Sample calculation is given in Figure C.7 below.

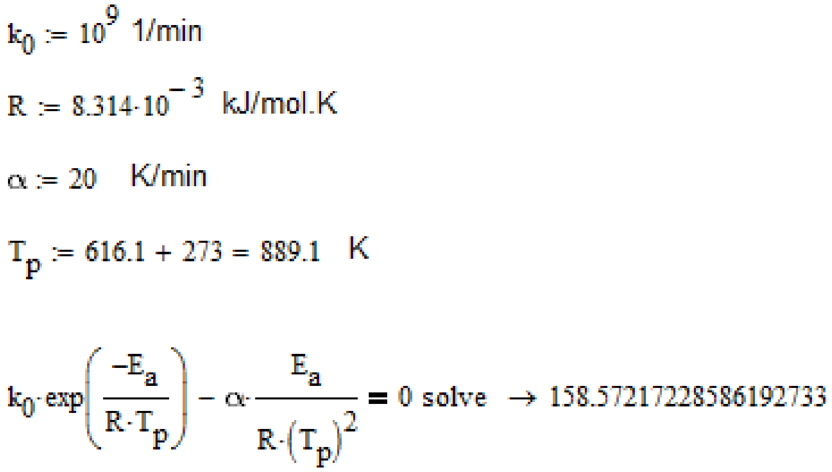

$k_0 := 10^9$ 1/min

$R := 8.314 \cdot 10^{-3}$ kJ/mol.K

$\alpha := 20$ K/min

$T_p := 616.1 + 273 = 889.1$ K

$$k_0 \cdot \exp\left(\frac{-E_a}{R \cdot T_p}\right) - \alpha \cdot \frac{E_a}{R \cdot \left(T_p\right)^2} = 0 \text{ solve } \rightarrow 158.57217228586192733$$

Figure C.7 Activation energy calculation by Redhead Method using MathCad

C.5. Dispersion Calculations

Dispersion of Pd and mean particle diameter were calculated using strong adsorption amount for all prepared oxides. Sample calculation for chemisorption experiments is given below.

$$\% \boldsymbol{Dispersion} = 9.0\ \frac{\mu mol\ H2}{gcat} \times \frac{1\ gcat}{0.01\ g\ Pd} \times \frac{106.42\ g\ Pd}{1\ mol\ Pd} \times \frac{1\ mol\ Pd}{10^6\ \mu mol\ Pd} \times \frac{2\ \mu mol\ H}{1\ \mu mol\ H2} \times 100 = 19.2\ \%$$

$$\boldsymbol{Mean\ Particle\ Diameter} = \frac{100}{\%\ Dispersion} = \frac{100}{19.2} = 5.21\ nm$$